Universidade de Aveiro
2016

Departamento de Engenharia de Materiais e Cerâmica

Alexandra Bînțu

Análise e controlo da velocidade de deformação das ligas de Al-Mg e aço TWIP para melhorar o comportamento mecânico

Analysis and control of SRS of Al-Mg alloys and TWIP steel for improved mechanical performance

Universidade de Aveiro
2016

Departamento de Engenharia de Materiais e Cerâmica

Alexandra Bînțu

Análise e controlo da velocidade de deformação das ligas de Al-Mg e aços TWIP para melhorar o comportamento mecânico

Analysis and control of SRS of Al-Mg alloys and TWIP steel for improved mechanical performance

Tese apresentada à Universidade de Aveiro para cumprimento dos requisitos necessários à obtenção do grau de Doutor em Ciência e Engenharia de Materiais, realizada sob a orientação científica do Prof. Doutora Gabriela Tamara Vincze, Professora Auxiliar Convidada do Departamento de Engenharia Mecânica da Universidade de Aveiro e do Prof. Doutor Cătălin Radu Picu, Professor Catedrático do Department of Mechanical, Aerospace & Nuclear Engineering, Rensselaer Polytechnic Institute, Troy, EUA.

I dedicate this work to all who believed in me

o júri
presidente

Doutor Luís Filipe Pinheiro de Castro
Professor Catedrático da Universidade de Aveiro

Doutor Joaquim Manuel Vieira
Professor Catedrático da Universidade de Aveiro

Doutor Manuel Fernando Gonçalves Vieira
Professor Associado da Faculdade de Engenharia da Universidade do Porto

Doutor Fábio Jorge Pereira Simões
Professor Adjunto, Instituto Politécnico de Leiria

Doutora Marta Cristina Cardoso de Oliveira
Professora Auxiliar da Faculdade de Ciência e Tecnologia da Universidade de Coimbra

Doutora Gabriela Tamara Vincze
Professora Auxiliar Convidada da Universidade de Aveiro

Acknowledgements

My years here in Aveiro have been a period of one of the greatest personal growth in my life. These accomplishments, however, would not have been possible without the help of several people and I am grateful for the tremendous roles they have played in my life.

First, I'd like to thank my scientific supervisor, Prof. Dr. Gabriela Tamara Vincze, for the support, guidance, encouragement and most importantly for her friendship throughout this thesis from the initial to the final stage. Her persistent help alongside high professionalism have offered me the opportunity to easily integrate into the workings of academic research. I'd also like to express my sincere gratitude to my co-supervisor, Prof. Dr. Cătălin Picu from the Rensselaer Polytechnic Institute, New York, for his continuous kindness, support, scientific advice and fruitful discussions during the development of the work. His insights have guided me to a level of understanding higher than I thought possible.

I would like to express my deepest appreciation to Prof. Dr. Jose Joaquin Grácio. Even though he is no longer with us, I can never forget his valuable advice, encouragement and numerous stimulating discussions.

My sincere thanks to Prof. Dr. Augusto Lopes for his constant availability, kindness and technical support for all the microstructural investigations that were carried out. His willingness to always help at any time with a smile was greatly appreciated. I also, gratefully acknowledge the contribution of Prof. Dr. Frederic Barlat, especially in the Chapter 5 of this present thesis. Many thanks goes to Prof. Dr. Mihaela Banu for always believing in me and encouraging me.

I would like to express my gratitude to all the staff members at the Centre for Mechanical Technology and Automation (TEMA) and the Department of Materials Engineering and Ceramics, for their assistance in my research work. The projects BD/UI/5624/2011 and PTDC/EBEPME/116683/2010 for financial support, are greatly appreciated.

From the bottom of my heart a special vote of gratitude goes to my parents, Liliana and George, my sister Oana and my grandmother Gina. Without their continuous support, sacrifice and belief in me from the first day of my work to the end, I would not have gotten to this point. This dissertation stands as a testament to their success. I offer my deepest thanks also to all my Romanian, Portuguese, French, Indian and Pakistani friends who absolutely encouraged and cared about me throughout these years. Last but not the least, this thesis is also dedicated to you, João. Thank you for your true love and support!

palavras chave

ligas de alumínio magnésio, aço TWIP, comportamento mecânico, sensibilidade à velocidade de deformação, refinamento de grãos, deformação por maclagem

resumo

Nesta tese são apresentados estudos experimentais e microestruturais para a análise e controlo da sensibilidade à velocidade de deformação (SRS) da liga AA5182 e do aço TWIP com o objetivo de melhorar o comportamento mecânico destes materiais. Os aços TWIP são materiais com elevada resistência mecânica e excecional capacidade de encruamento, parâmetros que conduzem à absorção de uma quantidade significativa de energia antes de rotura. As ligas de AlMg são materiais leves, com boa resistência à corrosão e boas propriedades mecânicas. A larga variedade de aplicações, como por exemplo na indústria automóvel, permitirá melhorar a performance dos produtos e economizar energia.

O maior problema destes materiais prende-se com a baixa ou negativa sensibilidade à velocidade de deformação que conduz a uma deformação heterogénea e limita a deformação após estricção. Neste trabalho são estudados métodos para melhorar a SRS das ligas de AlMg através de combinação de deformação plástica severa e tratamentos térmicos, e é investigada a origem física da baixa ou até negativa SRS do aço TWIP através de ensaios à escala macro, micro e nano. Estes estudos são complementados e sustentados por um amplo programa de observações microestructurais através de técnicas de microscopia TEM, SEM e EBSD.

A deformação plástica severa na liga de AlMg foi aplicada através de laminagem. Foi demonstrado que o tipo de laminagem (simétrica versus assimétrica), o grau de redução de laminagem e o tratamento térmico realizado após a laminagem são os principais fatores que afetam a evolução da SRS. Especificamente, o aumento do grau de laminagem (de 50% para 90%) resulta num aumento da SRS. A técnica de laminagem assimétrica inversa (ASRR) revelou ser a mais eficiente no aumento do SRS, sendo que esta produz a maior deformação equivalente no material. Adicionalmente, para este tipo de laminagem e uma redução da espessura de 90%, verificou-se que a tensão de cedência aumenta para um tratamento térmico mais longo (de 30min a 120min). Conjetura-se que o processo físico associado ao comportamento observado está relacionado com a movimentação de ida e volta de solutos de Mg da solução sólida para precipitados/cachos durante o processo de laminagem e posterior tratamento térmico.

A investigação à sensibilidade da velocidade de deformação de aço TWIP com base em testes mecânicos e caracterização microestrutural foi outro objetivo desta tese. Demonstrou-se que as amostras testadas com uma velocidade de deformação reduzida apresentam uma densidade de maclas maior do que as amostras testadas a uma velocidade de deformação maior. À escala macroscópica este traduz-se numa taxa de encruamento maior para velocidades reduzidas, conduzindo a um coeficiente de sensibilidade à velocidade de deformação em termos de taxa de encruamento negativo. Foi observada uma diminuição da SRS com o aumento da deformação, passando de valores positivos a negativos. O presente estudo demonstrou a importância da medida de escala utilizada na investigação do SRS através de uma combinação de testes de micro- e nano-indentações. Nomeadamente, quando o material é testado a uma escala nanométrica, através de nano-indentação, as amostras pré-deformadas em tração com taxas de deformação menores apresentam sistematicamente uma dureza menor do que as amostras pré-deformadas com taxas mais elevadas. À medida que o volume de material testado aumenta, a dureza relativa das duas amostras passa gradualmente da tendência observada à escala nano para aquela observada à escala macroscópica. O efeito está ligado ao mecanismo de interação entre as estruturas de deslocações e maclas.

keywords

aluminium magnesium alloys, TWIP steel, mechanical behavior, strain rate sensitivity, grain refinement, deformation twinning

abstract

In this thesis are presented experimental and microstructural studies for strain rate sensitivity (SRS) control and analysis of AA5182 and Twinning Induced Plasticity steel for improved mechanical performance.

TWIP steels are materials with very high strength and exceptional strain hardening capability, parameters leading to large energy absorption before failure. Al-Mg alloys are lightweight materials with good corrosion resistance and adequate material properties. The broader use of these materials, for example in the automotive industry, would allow improved product performance and energy savings.

The formability of these materials is strongly affected by their negative strain rate sensitivity (SRS) which leads to early failure and limits the post necking deformation. In this work we study ways to improve the strain rate sensitivity of Al-Mg alloys through a combination of severe plastic deformation and annealing, and we investigate the physical origins of the low and potentially negative strain rate sensitivity of TWIP steel through macro, micro and nanoscale testing. These studies are supported by extensive microstructural observations.

The severe plastic deformation applied to Al-Mg alloys is applied by rolling. It is shown that the type of rolling (symmetric versus asymmetric), the rolling reduction degree and the applied heat treatment performed after rolling are the main factors affecting the evolution of SRS. Specifically, SRS increases with increasing the degree of rolling for given post-rolling heat treatment. The reversed asymmetric rolling technique appears to be the most efficient in increasing SRS since it produces the largest equivalent plastic strain in the sample. Furthermore, the evolution of tensile flow stresses depends on the chosen thermal treatment; it was observed that the yield stress increases with increasing the annealing time for rolling reduction of 85%. It is conjectured that the physical process responsible for the observed behavior is related to the movement of Mg from solid solution to precipitates/clusters and back during rolling and subsequent annealing.

The investigation of the strain rate sensitivity of TWIP steel based on mechanical tests and microstructural characterization is another objective of this thesis. It was demonstrated that slower-deformed samples have a higher twin density, which leads to larger flow stress measured in a macroscopic uniaxial test and results in negative strain hardening rate sensitivity. The SRS is observed to decrease with strain, becoming negative for larger strains. The correlation between SRS and the probing scale was revealed by a combination of micro- and nano-indentation experiments. When probed at the nanoscale by nano-indentation, samples pre-deformed in tension at smaller strain rates exhibit systematically smaller hardness than samples pre-deformed at higher rates. As the volume of material probed increases, the relative hardness of the two types of samples gradually shifts from the trend observed at the nanoscale to that observed macroscopically. The effect is linked to the dislocation-twin interaction mechanism.

Contents

Symbols and abbreviations

bcc	Body centered cubic crystals
fcc	Face centered cubic crystals
b	Magnitude of the Burger vector
τ	Shear stress
σ_y	Yield stress
SRS	Strain rate sensitivity
m	Stran rate sensitivity parameter
m^i	Instantaneous rate sensitivity
m_θ	Strain hardening rate sensitivity
EBSD	Electron backscatter diffraction
IPF	Inverse pole figure map
PF	Pole figure map
MO	Misorientation average
γ	Shear strain
F	Applied force
A	Cross-section area
m^s	Schmid factor
c_τ	Critical resolved shear stress for slip
θ	Strain hardening rate
RT	Room temperature
α	Average intensity of the dislocation interaction
μ	Shear modulus
τ_o	Friction stress
ρ	Dislocation density
Λ	Mean free path of mobile dislocations
$f(g)$	Orientation distribution function (ODF)
$\phi1$, φ, ϕ	Euler's angles
σ	True stress
ε	True strain
M	Taylor factor
ν	Poisson coefficient
$\dot{\boldsymbol{\gamma}}$	Shear strain rate
n	Strain hardening coefficient
$\dot{\boldsymbol{\varepsilon}}$	Strain rate
ufg	Ultrafine grain
PLC	Portevin-LeChatelier effect
DSA	Dynamic Strain Aging
HV	Vickers Hardness
HRC	Rockwell hardness

BIW	Body in White
AHSS	Advanced High Strength Steel
UHSS	Ultra-High Strength Steel

List of figures

Chapter 2

Chapter 3

Chapter 4

Chapter 5

Chapter 6

CHAPTER 1

Introduction

CHAPTER 1 - Introduction

Processing by sheet metal forming has a relevant impact on the manufacture. Production of plastic deformed sheets remark significant growth year after year. With diversification of deformation methods, low price, modernization and industrialization machinery, processing by plastic deformation has recently more extensive applications such as aerospace, automotive or packaging. Metal plasticity has to be controlled to enhance design, quality and enforcement of vehicle components. Car weight is directly related to fuel consumption and hence to pollution and environmental degradation. However, the weight is also determined by consumer expectations with respect to safety, performance, passenger comfort and overall vehicle quality. This led to a continuous decrease of the net weight over the past years. Reducing the weight without compromising vehicle performance has to involve the use of higher strength materials. This is where Aluminum-Magnesium alloys and Advanced High Strength Steels (AHSS) find their place into automotive industry. Interestingly, besides their exceptional mechanical properties, both of these metals exhibit negative strain rate sensitivity (SRS), at least in some ranges of temperature and strain rate, which renders their mechanical behavior sensitive to notches and small geometric and microstructural defects. Fundamental questions regarding the mechanism of SRS are persistent in the literature. The dominant concept related to this is based on the classical mechanism for Dynamic Strain Ageing (DSA) which requires a certain degree of coupling between the intermittent motion of dislocations and the evolution of mobile solute atoms.

The use of AA5182 (Al-Mg alloy) and TWIP steel (AHSS) for manufacture of light weighing car components may therefore require detailed investigation to achieve a better understanding of the small-scale processes and multiscale mechanisms underlying their deformation behavior.

1.1Motivation and objectives of the thesis

Many metallic materials can be produced with low cost by forming operations, where the requested shape is obtained from a sheet by plastic deformation. Among this products, Advanced High Strength Steels (Ex. TWIP steels) and Aluminum-Magnesium alloys (AA5182) are interesting choices because of their high strength to weight ratio, high crash resistance or high corrosion resistance. Their inherent high strength allows structural components to be thinner, making the vehicle lighter and more fuel efficient.

Nowadays complete vehicles are being made from aluminum alloys and also TWIP steels are beginning to find its way into the car industry. Steels with higher strengths allowing a thickness reduction and thus lower weight are also more commonly used. Compared to pure aluminum or ordinary mild steel, the materials mentioned above are all more difficult to form. Therefore, for process optimization it is important to have a deep understanding on the material behavior. Additionally, major technological changes are on the horizon that require significant advances to be made in the science and technology of metal forming.

The main objective of this thesis is to explore ways and find possible solutions to increase the SRS of AA5182 and TWIP steels. This will be accomplished by a combination of experimentation on the macroscopic/microscopic scale. Specifically, using a coupling of rolling and heat treatments in AA5182 we committed to determine whether the SRS at room temperature may be rendered positive through such processing. The relationship between basic deformation behavior and the microstructural response of the materials will be sought.

The other purpose of the present work is to investigate the relationship between twinning rate and the applied deformation strain rate in an 18% Mn TWIP steel and to observe the effect of this dependence on the macroscopic rate sensitivity of the material. The correlation between SRS and scale dimension in TWIP steel is also presented.

The expected significance of the proposed research is that it will lead to an improved understanding of the fundamental mechanisms controlling plasticity in Al-Mg alloys sheet and TWIP steels. This research will allow a broad use of this class of high strength materials with exceptional energy absorption properties in automotive manufacturing.

1.2 Evolution and structure of the thesis

This thesis is divided into *seven* chapters and partial conclusions are presented in the last part of each chapter. The results interpretation is closely correlated with the presented studies. The list of bibliography indices is presented at the end of the thesis. Finally, the results of this present work can serve for constitutive modeling of processes occurring during forming of Al-Mg alloys and TWIP steels.

The manuscript starts with an *Introduction*, which represents *Chapter 1*. This introductory section presents the basis of the work with the main issues that needs to be solved.

The *Literature Review* which introduces a rigorous analysis of the deformation mechanisms in metal and alloys, together with the characterization of the factors that influence sheet metal forming processes, compose the *Chapter 2.*

Chapter 3, describes the main issues related with the formability of Al-Mg alloys (AA5182) and TWIP steel as well as a comparison between them. Afterwards, the experimental procedures used to achieve the thesis objectives are presented. The mechanical tests were carried out at *Departamento de Engenharia Mecânica*, in addition to microstructural characterization of the materials at *Departamento de Engenharia do Materiais e Ceramica, Universidade de Aveiro*.

The results obtained after testing AA5182 by mechanical and microstructural means compose *Chapter 4*. Two main tests have been carried out: asymmetric/symmetric rolling and uni-axial tensile tests that together with thermomechanical processing and metallographic characterization give a full picture of deformation mechanism of the alloy sheet.

With *Chapter* 5 one can gain a detailed understanding of the dependence of the twinning evolution on the strain rate in TWIP steels, which results in negative strain hardening rate sensitivity (SHRS). Electron microscopy and electron backscatter diffraction (EBSD) techniques were carried out to characterize the evolution and development of the microstructure.

Chapter 6 was reserved for a combination of nano-indentation, macro-indentation and EBSD experiments undertaken by TWIP steel. The chapter presents some aspects that are little studied in literature, regarding the hardness characterization of the steel involving

different micro and macro techniques, which led to the opening of new interesting directions of research in the future.

The thesis ends with general conclusions in *Chapter* 7, that include the synthesis of the results obtained, as well as the outstanding issues that need further effort and perspectives in the context of results.

CHAPTER 2

Literature review

CHAPTER 2 – Literature review

This chapter makes a review of the literature that serves as theoretical basis on which this study relates.

2.1. Basic deformation mechanisms in metals and alloys

Sheet metal forming is a major fabrication process for the economical manufacturing of metals and alloys products into a three dimensional complex shape by plastic deformation. This process is increasingly widespread in aerospace industry, car bodies, electronics, automation, and many other domains. There are many different metals that can be made into sheet metal, such as aluminum, steel, copper, nickel, titanium, etc. Since operations like bending, stretching, stamping, blanking or pressing, occur within a high-volume industry, even small improvements in materials properties, simulations, and manufacturing costs will translate into substantial savings. Metals and alloys are deformable solids with elastic and plastic properties. Plastic deformation is always preceded by elastic deformation. After removing the external force, the elastic deformation is recovered and only plastic deformation remains.

Plastic region of the stress-strain curve is of primary interest in most applications. In plastic region, a metal's behavior can be approximated as:

$$\sigma = K \cdot \varepsilon^n \quad (1)$$

with K= strength coefficient; n =strain hardening exponent.

Plasticity describes the deformation of a material undergoing non-reversible changes of shape in response to applied forces [Callister1994]. For example, a solid piece of metal being bent or pounded into a new shape displays plasticity as permanent changes occur within the material itself [Osakada2008].

At room temperature, plastic deformation usually occurs through non-diffusive mechanism like slip (dislocation motion) and twinning [Karaman2000]**.** The Stacking Fault Energy (SFE) will determine the deformation mode. In high SFE materials, as in aluminum (Face centered

cubic-FCC crystal), the plastic deformation occurs mainly by dislocation motion. In TWIP steel (FCC structure) or magnesium (HCP structure), where the SFE is medium or low, twinning develop. In the next section we are going to describe these two major plastic deformation modes.

2.1.1 Mechanism of Slip Deformation

2.1.1.1 Single crystal plasticity

In single crystal, during plastic deformation, slipping occur along the specific crystallographic directions [uvw] in which the atoms are more closely spaced lying in associated crystal planes {hkl} with highest atomic density. These define the slip system in which dislocations can move. Their nucleation and multiplication/growth under stress govern the mechanical behavior of materials.

During slip, two parts of the crystal are sheared (fig 2.2). Atoms tend to move along the plane where the resistance is lowest [Haasen1965]. This condition is fulfilled on close packed planes [Roylance2008].

In table 1 below is shown an example of slip system specific for FCC metals.

Table 1 *– Slip System specific for FCC*

Lattice	Metals	Slip Planes	Slip directions per slip plane	Number of Slip Systems
FCC	Feγ, Cu, Al, Ni, Pb, Au	4 {111}	3 <110>	12

FCC have high plasticity that show many possibilities for sliding under low stress (figure 2.1).

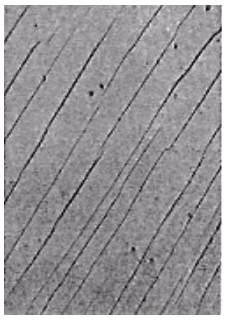

Figure 2.1 *Sliping mechanism in Single Crystal [Callister1994]*

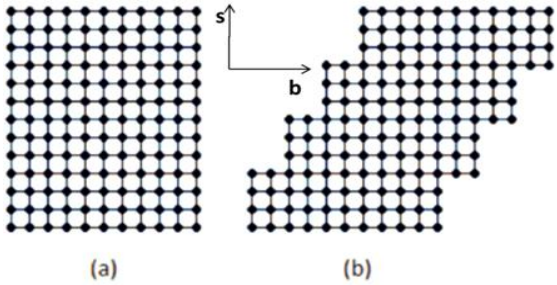

Figure 2.2 *- Shearing of crystalline plans during deformation [Wierzbanowski2011]*

To activate a slip system, shear stress (τ^S) has to achieve a threshold value: the critical resolved shear stress *(CRSS or* τ^S_{CRSS}*).* In uniaxial tension, the applied shear stress fulfils the condition:

$$\tau^S = \frac{F.\cos\theta}{A_s} = \frac{F.\cos\theta}{A_0/\cos\varphi} = \sigma(\cos\theta.\cos\varphi) \equiv \frac{\sigma^s}{m^s} > \tau^S_{CRSS} \qquad (2)$$

where *F* is the applied force, *A* the cross-section area, and Θ and φ are the angles between *F* and the slip direction and the slip plane normal, respectively. Parameters of *equation 2* are visible in figure 2.3.

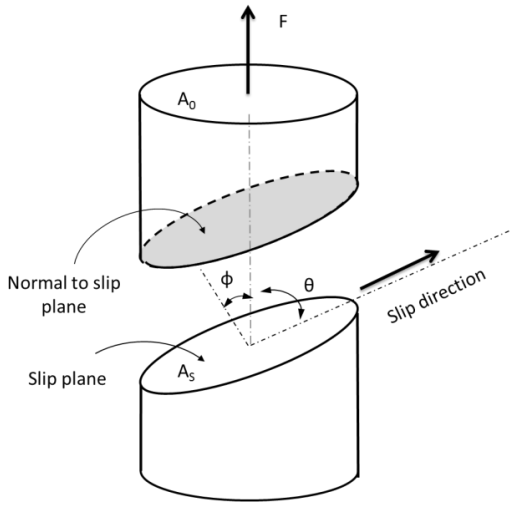

Figure 2.3*– Sliping mechanism in single crystal showing the definition of angles θ and φ [Callister1994, Roylance2008]*

The product of the cosine of φ and θ angles is the Schmid factor *(m^S)*, of the slip system *(s)* and characterize the influence of the crystallographic orientation of the crystal on the activity of the slip systems. Therefore, Schmid's law indicates that for slip to happen [Schmid1924]:

$$\tau^s = m^s \sigma^s > \tau^s_{CRSS} \quad (3)$$

When the product of the Schmid factor and the applied stress *(σ)* reaches the critical resolved shear stress (CRSS) value, the slip system *s* is activated and plastic deformation occurs. This threshold value depends on the lattice friction, solute and precipitates contents, interactions between dislocations, temperature and strain rate. The orientation of the grain, with respect to the deformation, will define the stress at which the slip system activates.
In a given crystal, there may be many available slip systems. As the tensile load is increased, the resolved shear stress on each system increases until eventually τ^s_{CRSS} is reached in one system [Schimd1924, Lopes2001]:

- When τ^s is equal with τ^s_{CRSS} the slip system *s* is activated. When this happen the slip system is known as the primary slip system. The stress required to cause slip on the primary slip system is the yield stress of the single crystal. As τ^s is increased further, τ^s_{CRSS} may be reached on other slip systems. This can be explained by the movement of the dislocations present in a real single crystal.
- When τ_s is smaller than τ^s_{CRSS} the slip system is not activated.

i. Dislocation microstructure evolution during hardening

During loading, plastic deformation and the density of dislocations in the material increases as a result of dislocation multiplication processes. This corresponds to a decrease of the dislocation mobility and, consequently, to an increase of the CRSS value with the strain.

This phenomenon is called strain hardening (or work-hardening) and is responsible of the increased resistance of the material to the plastic strain. For monotonic deformation, the shear stress necessary to deform a monocrystal depends on the dislocation density ρ through the relation:

$$\tau = \tau_0 + \alpha\mu b\sqrt{\rho} \quad (4)$$

where τ_0 is the stress related to the lattice friction, solute and precipitate contents, α dislocation interaction factor, μ the shear modulus of the material and b the Burger vector of dislocations. In this expression, the dislocation density is the result of two competitive processes: dislocation accumulation and dislocation annihilation or recovery.

From a mechanical point of view this phase belongs to Stage I in stress-strain curves, characterized by low hardening rate as can be observed in figure 2.4. The hardening rate can be expressed by the formula 5 below. When a single slip system is activated, dislocations define parallel cells which are parallel to the trace of the slip plane with highest activity (micrograph (a) of figure 2.5).

$$\theta = \frac{\partial\sigma}{\partial\varepsilon} \quad (5)$$

With activation of a two non-parallel slip systems, a new set of cells develops, giving rise to two sets of dislocations cells (micrograph (b) in fig. 2.5). In this line, the beginning of stage II is activated, characterized by a linear increase of the hardening rate. As the amount of active slip system increases, dislocation cells appear (micrograph c, d in fig. 2.5) giving rise to the last stage of hardening mechanism in single crystals, distinguished as Stage III. During this stage the diameter of the cells decreases with straining due to dynamic recovery process as a result of mutual annihilation of dislocations and cell refinement.

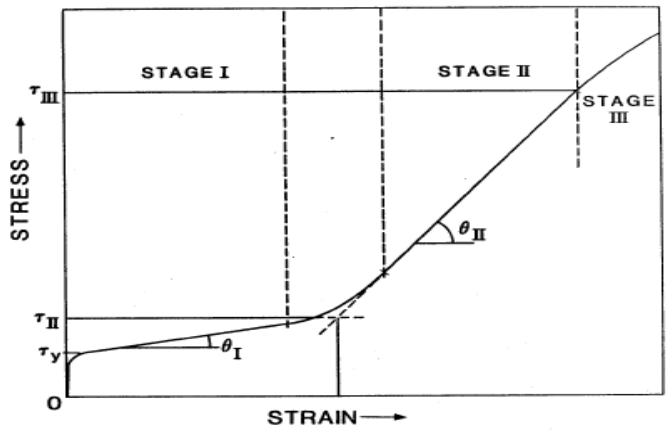

Figure 2.4 *- A typical true stress-true strain curve for a Cu single crystal showing the three stages of work hardening: Stage I = "easy glide" single slip system; Stage II with high, constant and athermal hardening rate, multiple slip systems; Stage III with saturation of hardening rate, cross slip, and very sensitive to temperature and strain rate [Diehl1956].*

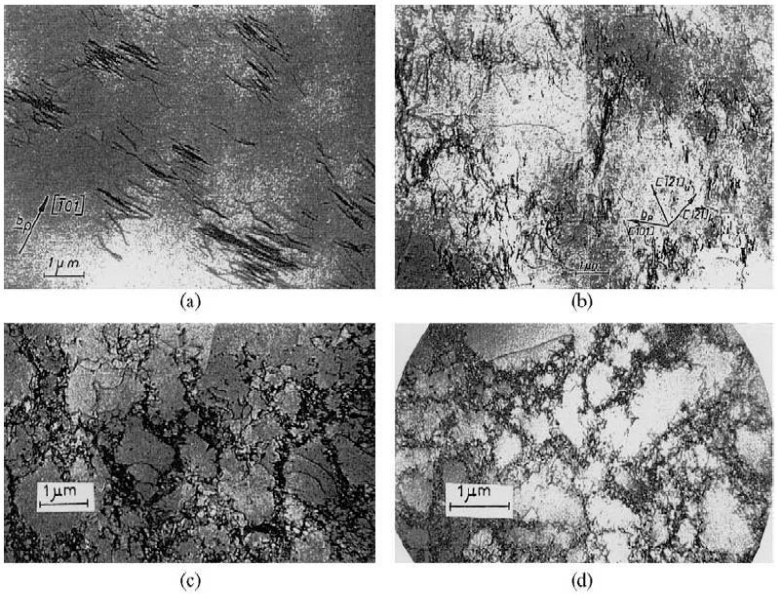

Figure 2.5 *- TEM images of dislocation microstructure developed during plastic deformation evolution in Cu single crystal: (a) end of stage I; (b) stage II; (c) and (d) are from <100> crystal and shows the evolution of discolation cells during Stage III. All Tests were done at room temperature [Kocks2003].*

Dislocation motion is ruled by several parameters like : strain, strain rate and temperature. Changing those parameters will affect materials hardening. For example, an

increase of the test temperature results in material softening due to recovery effect. Oppositely, the strain hardening increases with the applied strain rate.

2.1.1.2 Polycrystalline plasticity

Polycrystals are composed of grains with relative different crystallographic orientations. If the material is untextured, grains are randomly oriented (unordered). When deformed, each individual grain undergoes a slip. The load when the sliding start in each grain depends on its orientation relative to the global loading axis, following the *Schmid's law*. The change of shape in a plastic deformed grain may be constrained by neighboring grains which had not yet reached the point of flow. In addition, the boundaries between the grains act as strong barriers against dislocation movement. Also the internal stress around the concentrations of dislocations in the grain boundaries, which were subject to creep (flow) can create dislocation sources operating in neighboring grains [Hansen1996]. In conclusion, a grain in a poly-crystal is not free to deform plastic as a single crystal, because have to stay in contact with others and to adapt to the changes of shape of its neighboring grains.

However, the slip mechanisms occurring in a single crystal also hold for polycrystals but the deformation response is more complex in polycrystalline materials (fig. 2.6).

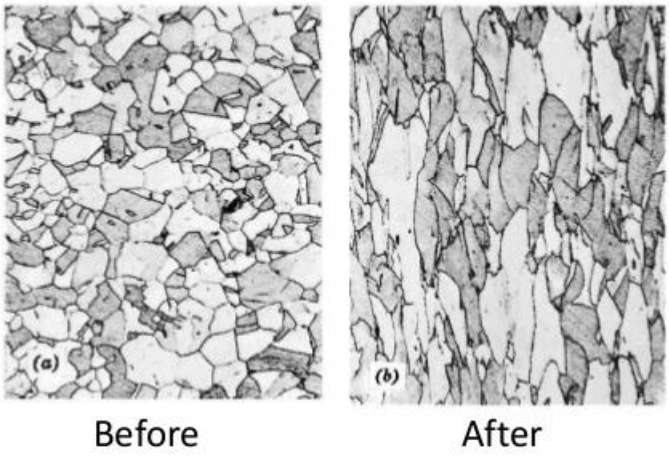

Figure 2.6 *– Deformation of polycrystal material causing elongation of grains along the applied stress [Dieter1984]*

From one crystal to another, the orientation can be very different. Assuming the deformation is compatible with the next grain strain state, each grain influence the deformation and stress state of the surrounding grains.

i. Microstructure and crystallographic texture evolution

Considered in a global manner, the orientations of every grain in a polycrystalline aggregate, can be concentrated, in big or small scale, around some specific orientations. Any material will develop crystallographic texture or preferential orientation if it suffers large plastic deformation by dislocation glide on restricted slip planes. For metallic materials the preferential orientation of the grains occurs during thermomechanical processes as solidification, cold or hot work processes, etc. In this way, the crystallographic texture can be generally defined as a condition in which the grains orientation distribution of a polycrystalline material is not randomized. It is important to understand that the texture does not refer to the shape of the grains, but rather to the crystallographic orientation of the grains.

There are different methods to describe the evolution of a polycrystalline material. For this, it is required that the grains orientations in a particular crystallographic plane (hkl) with a specific direction [uvw], is being determined. X-Ray diffraction is a traditional method, in which is measured the diffracted intensity by (hkl) plane, being associated with a given crystalline orientation of the sample. In a polycrystal, millions of grains are analyzed with this method. Nowadays, EBDS technique allows the determination of individual orientation of every grain in a much simpler and rapid way, through direct pole figures (PF). However, in the case of sheet metal, a quantitative and complete description of crystallographic texture can be obtained with the help of ODF (*Orientation Distribution Function*), in which the occurrence frequency of specific orientations in a 3D space are specified. This space is defined by the three *Euler* angles*:* φ_1, ϕ and φ_2 which constitute three consecutive rotation applied to [100], [010] and [001] axis of the crystal cell, so that they coincide with the ND, TD and DD of the sample (figure 2.7 and figure 2.8).

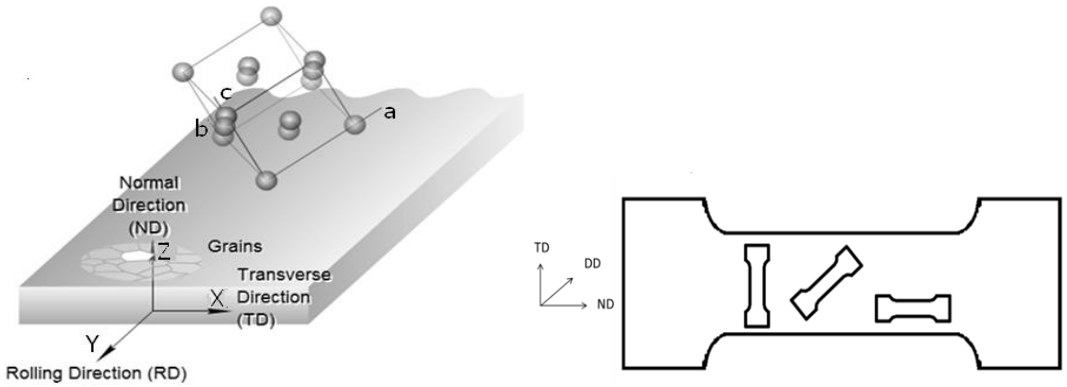

Figure 2.7 *– Crystal fixed axis (a, b, c) and specimen fixed axis (X, Y, Z) defined for a sheet and a dog-bone shape sample [www1].*

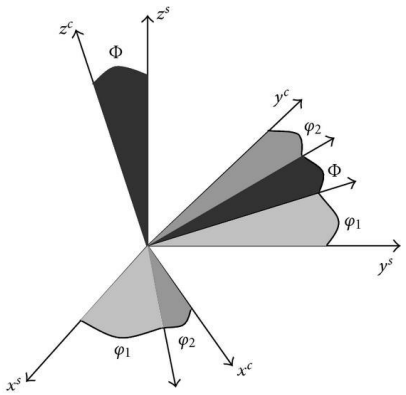

Figure 2.8 *– Euler's angles definition after Bunge notation [Bunge1982].*

Knowing the crystallographic orientation ($g=(\varphi_1,\Phi,\varphi_2)$), the crystal can be represented by one point in Euler space like in figure 2.9. In FCC or BCC crystals with no sample symmetry, the range of Euler's angles is defined as $0\leq\varphi_1\leq 2\pi$, $0\leq \Phi\leq \pi/2$, $0\leq\varphi_2\leq \pi/2$ [Lopes2010, Vincze2007, www1]. Considering the orthotropic sample symmetry, the subspace defined for the Euler's angles will range from 0 to 2π [Nolze2015].

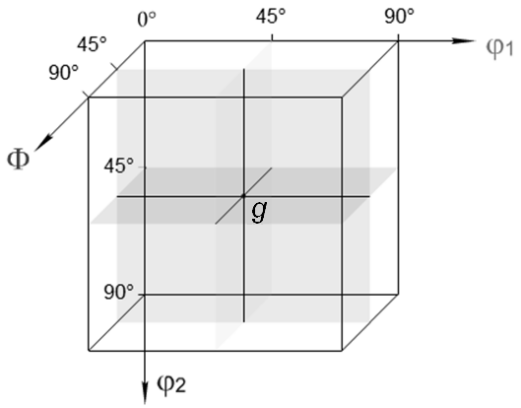

Figure 2.9 *– Euler Space [Houtte1987]*

ii. Polycrystal modelling of plastic deformation

Due to the different orientations of slip planes from one grain to another, the chemical or structural inhomogeneity, the processes of plastic deformation of polycrystalline aggregates are much more complex than in single crystals. Over the years, this fact has represented a challenging task. There are many models developed for this purpose, linking behavior of single crystal with polycrystal through homogenization methods [Osakada2008, Lopes2001, Vincze2007, Kocks2000, Lebensohn1994]. These techniques had been utilized to define the transition from microscopic to macroscopic scale. Among the classics we can mention: Sachs model, fully imposed conditions models (Full Constraints FC) as formulated by Taylor [Taylor1938], relaxed conditions by Honnef and Mecking [Honnef1978] and self-consistent as developed by Lebensohn and Tomé [Lebensohn1994].

In BCC and FCC metals the models that involve a homogenous deformation of polycrystalline aggregate foretell the development of highly concentrated crystallographic textures for intermediate deformation and associated mechanical anisotropy. Nevertheless, in HCP crystals the hypothesis of plastic homogenous deformation seems not sufficiently satisfactory to predict the evolution of the deformation texture. Just sometimes, the full constraints model has been applied to slip analysis in hexagonal closed packed metals,

because twinning has a great influence on their homogeneous and large-scale deformation [Morita2011]. However, the predictions of the model can be considerably improved if the local heterogeneity of rate gradient induced by the interaction between neighboring grains is considered [Lebensohn1994, Molinari1987].

In this section, three incremental rate-insensitive micro-mechanic models, are summarized to predict the reorientation of the crystals, the evolution of anisotropy, crystallographic texture and hardening during plastic deformation of an aggregate of anisotropic structure.

a. Sachs Model

First model for plastic deformation was proposed by Sachs in 1928 [Sachs1928]. According to him, every grain within a polycrystalline aggregate subjected to a macroscopical stress undergoes the same stress as in the bulk material. In other words, the Sachs hypothesis deals with identical stress and macroscopic spin in all crystals and ensures intergranular equilibrium at the expense of intergranular compatibility [Sachs1928, Havner1992]. In *2.1.1.1* it was proposed, according to Schmid law, that when the product of the Schmid factor and the applied stress (σ) reaches the CRSS value (τ_c), the slip system is activated and plastic deformation occurs. Therefore, the macroscopic applied stress of the polycrystal is given by the following relationship:

$$\sigma = \langle m^{-1} \rangle \tau_c \tag{6}$$

Where, $\langle m^{-1} \rangle$ is the average value of the Schmid factor and τ_c is the resolved shear stress acting on the grains.

Even if Sachs model contradicts compatibility, this assumption may also be used to predict a plastic flow curve by implementing a hardening law [Clausen1997].

b. Taylor Assumption

Full Constraints (FC) Taylor model assumes that every grain undergoes the same change in shape, namely the microscopic plastic deformation of each polycrystal grain is identical to macroscopic plastic deformation of the sample. To satisfy the full constraints

condition (accommodate the macroscopic strain), multiple slips systems were introduced in each grain. In the tension mode, the compatibility in a polycrystalline aggregate can be achieved with the activation of five independent slip systems in each grain [Hosford1993]. In this way the deformation energy is minimized and Taylor constitutive equation can be written as:

$$(W_{int})_{min} = \left(\sum_{s=1}^{S} \boldsymbol{\tau_c^s} |\gamma^s| \right)_{min} \quad (7)$$

Where:

- $(W_{int})_{min}$ is the minimum internal dissipated energy for polycrystalline deformation
- τ_c^s and γ^s are the the critical resolved shear stress and shear strain in the slip system *s* (in this case *S*=5)

The equivalence between internal and external plastic work during deformation allows to rewrite the equation 7 as [Kocks1970, Vincze2007, Havner1992]:

$$\sum_{i,j=1}^{3} \sigma_{ij}\, \varepsilon_{ij} = \left(\sum_{s=1}^{S} \boldsymbol{\tau_c^s} |\gamma^s| \right)_{min} \quad (8)$$

But $\tau_{CRSS} = \tau_c^s$ because, the critical resolved shear stress is independent of the slip system (*s*) and strain amount.

The same criteria for the active slip system can be expressed by the Taylor factor *M:*

$$\frac{\sigma}{\tau} = M = \frac{\gamma}{\varepsilon} \quad (9)$$

Where σ and ε are, respectively, the equivalent macroscopic Von Mises stress/strain. This means that the active slip system is the one with the minimum *M*-factor.

In other words, *M* represents the total of the slip rates in five independent slip systems for one deformed grain, and depends on the relationship between the tensile axis and grain orientation.

In the case of a polycrystalline aggregate, Taylor law can be written:

$$\sigma = \langle M \rangle \, \tilde{\tau} \qquad (10)$$

With $\langle M \rangle$ - average Taylor factor and $\tilde{\tau}$ – average shear stress

The calculated Taylor factor <*M*> for FCC polycrystals is 2.24 [Sachs1928] and 3.06 [Taylor1938] respectively.

It is well known that Taylor used this model to describe, successfully, the stress-strain relation as well as the texture development of polycrystalline metals in terms of the single crystal constitutive behavior, for the case of uniaxial tension. Just to compare with the previous model, in the figure 2.10 below, the theoretical tensile curves of a Cu polycrystal are represented, derived on the basis of Sachs model from an average single crystal curve and on the basis of the Taylor model from a single crystal of an orientation near <111> zone axis.

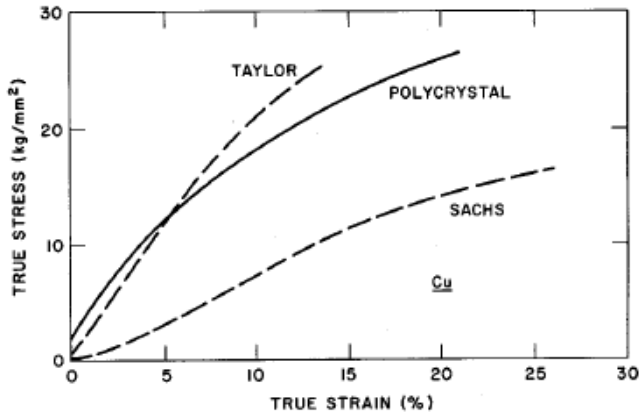

Figure 2.10*– True Strain-True Stress curves of Cu polycrystal with a grain size of 0.15 mm deformed at RT [Kocks1972].*

Like other models, the Full Constraints assumption has to overcome some drawbacks. The defect in the approach is that it says nothing about the activity or resolved stress on other non-active systems. This last point was addressed later on by Bishop and Hill in 1951 when they assumed that minimum (microscopic) slip system (Taylor) is equivalent to maximum work [Bishop-Hill1951]. In other works, the criterion for solving the Taylor ambiguity was extended to the *relaxed constraint model (RC)* [Van Houtte1981,Van Houtte1986, Kocks1970]. Modern approaches use the physically realistic strain rate sensitivity on each system to "round the corners" of the single crystal yield surface. For example, the most recent

work of M**á**nik and Holmedal [Manik2014] present a comprehensive way to solve the Taylor ambiguity by taking into account the strain rate sensitivity.

c. Self Consistent Visco Plastic Model

In the Visco-Plastic model, every grain is describe as an ellipsoidal visco-plastic crystal in which the material properties are the weighted averages of the grains properties, according to the crystallographic texture of the polycrystal [Clausen1988, Berveiller1979]:

$$E = \bar{\varepsilon} \text{ and } \Sigma = \bar{\sigma} \tag{11}$$

With E and Σ the macroscopic polycrystal strain and stress and $\bar{\varepsilon}$ and $\bar{\sigma}$ average strain and stress of each crystallite.

This successive treatment of every grain, one after the other allows to satisfy the local equilibrium and compatibility of the matrix. Taking into account the plastic anisotropy of every grain, unlike Sachs and Taylor models, in the viscoplastic self-consistent (VPSC) assumption every grain can undergo a different plastic deformation depending on its morphology and crystallographic orientation [Tome2002]. A series of authors proposed elasto-plastic constitutive equations to relate the model parameters [Kröner1961, Hill1965]. The most known incremental linearization equation based on the inclusion formalism belongs to Hill:

$$\sigma - \Sigma = -L^h\,(\varepsilon - E), \tag{12}$$

Where L^h is Hill's constrain tensor which depends of the shape and crystallographic orientation of the grains.

The viscoplastic model can be defined by the power law equation:

$$\dot{\gamma}^s = \dot{\gamma}_0 \left(\frac{\tau^s}{\tau_0^s}\right)^{\eta} \tag{13}$$

where, on the system (s), $\dot{\gamma}_0$ and τ_0^s are the reference shear rate and critical resolved shear stress and η is the inverse strain rate sensitivity of the material.

With this micro-constitutive relation it can be concluded that all systems are activated (but with a different magnitude) because the shear strain rate in each slip system $\dot{\gamma}^s$ is a

function of resolved shear stress τ^s. In this case the ambiguity of the Taylor model is overcome. For a better understanding this study proposes to establish a comparison between these two models.

Figure 2.11 shows the texture of an IF steel deformed in 4 passes via ECAE (Equal Channel Angular Extrusion), simulated by the VPSC and Taylor models [Li2006]. The results are compared with the experimental texture evolution. The Visco-Plastic model presents a texture simulation much more close to the experimental observation than the Taylor Assumption. This one seems to be unsuitable to model the evolution of the texture in different passes via ECAE, mainly because of the interaction between the grains and consequently, the heterogeneity of the deformation.

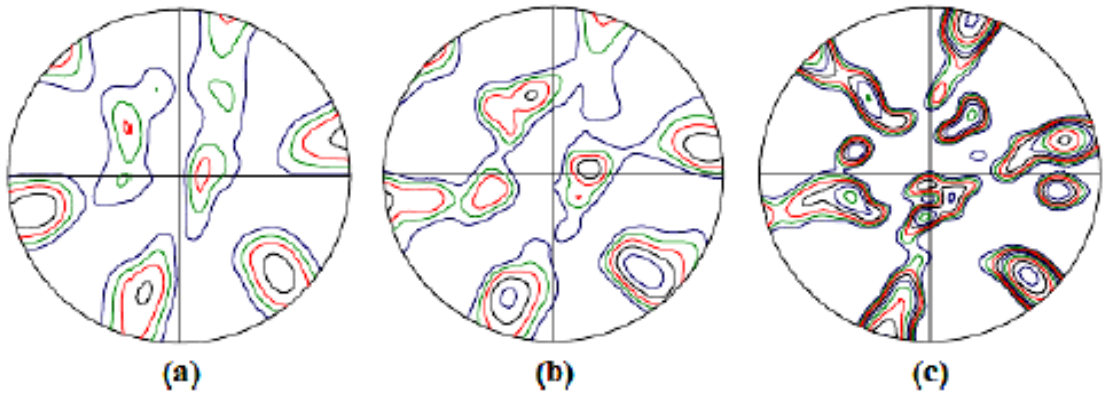

Figure 2.11 *– (111) Pole figures of IF Steel after 4 passes of ECAE: a) experimental; b) VPSC simulation; c) Taylor simulation [Li2006].*

This example, together with the others e.g. [Lebensohn1993, Tomé 2001] prove the excellent performance and superior ability of the VPSC formulation compared with the Taylor model, to capture the strong texture-induced anisotropy of polycrystals, the rapid textural changes induced by twinning/slip results in strong geometric hardening/softening, as well as the highly anisotropic slip-twin interaction [Segurado2012].

Summarizing, in Sachs model, the stress is assumed to be homogeneous and neighbor grains do not interact with each other. In Taylor model, the deformation of the grains is fully

constrained, and the strain is the same in all grains and equal to the macroscopic strain. VPSC model deals with the inhomogeneity of the grains treated as a solid and embedded in a homogeneous matrix subjected to macroscopic stress.

2.1.2 Mechanism of twinning deformation

Twinning is the plastic deformation in crystals defined as the collective shearing of one portion of the crystal with respect to the rest. It takes place along certain crystallographic planes and directions due to a set of forces applied on a given metal piece [Buerger1945, Cahn1954, Karaman2000].

A "twin" refers to a grain that has one or two twin boundaries with a larger grain in which it is embedded. In metals with hcp structures the twinning occurs with considerable ease, and thanks to the reorientation that produces this mechanism, may facilitate the activation of a slip system. This form of twinned structure becomes a mechanism to facilitate the deformation by dislocation movement, in structures even stiffer. Finally, metals with fcc structure, where slipping is greatly favored by the crystal structure, the mechanism of twinning is difficult to observe and often appears in unusual conditions like low temperatures or very high strain rates [Christian1995]. For this crystal structure, the twin boundary missorientation can be obtained by rotating the orientation of the parent grain 60° about <111> direction [Jin2013]. Such an FCC material that undergoes deformation by twinning is TWIP steel and it will be presented later in this thesis.

Under the microscope (EBSD), the twins appear in a different colour than the rest of the grains (figure 2.12 right), because they have different crystal orientation.

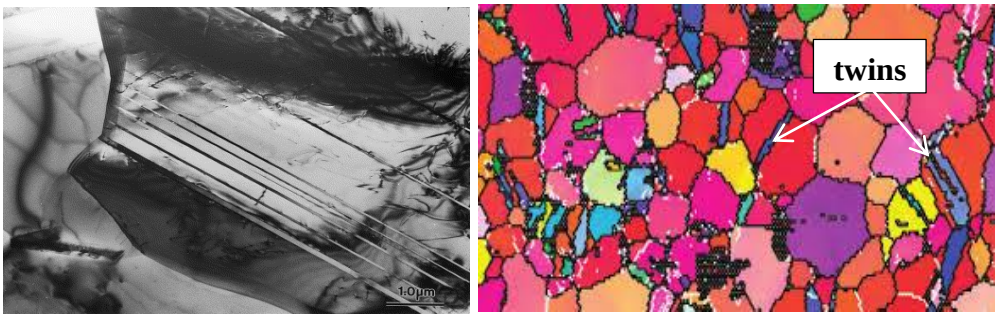

Figure 2.12*– left – TEM image showing twins in a γ grain (FCC); right: EBSD/IPF observation map of the deformation twins in AZ31B Magnesium Alloy.*
Specimen was strained under compression [Uota2009].

2.1.2.1 Stacking fault energy

For a FCC structure, the stacking sequence of the atomic planes is given by the following order: ABC ABC ABC. During plastic deformation, this order may transform to ABC ABA BC and planar ribbon like defects called *intrinsic stacking faults* form, which are bordered by an edge partial dislocation with a Burgers vector **b** = *a*/6<112> (Shockly dislocation). If the atoms are arranged ABC ABA CA BC, an *extrinsic stacking fault* is restrained, which is also bordered by a partial dislocation with a different Burgers vector **b** = 1/3<111> (Frank dislocation or double deformation – figure 2.13) [Frank1951]. The third type of fault encountered in the FCC structure, called twinning (growth fault), forms when the stacking pattern becomes ACBACB [Rosengaard1993].

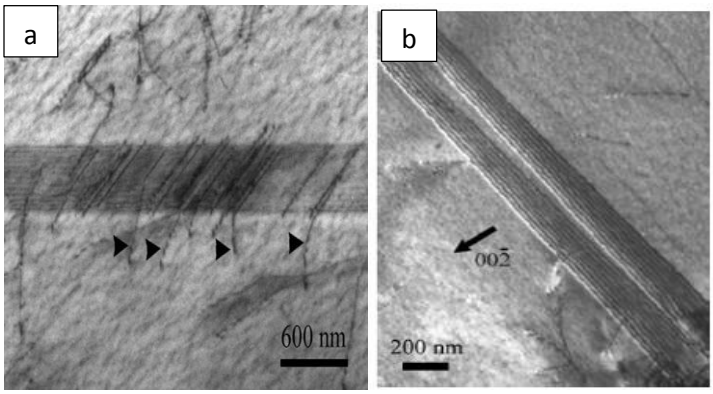

***Figure 2.13**– Microstructure of Fe–Mn–C TWIP steels: a) Frank dislocations in the material matrix; b) wide stacking fault in the (111) close-packed plane [Idrissi2010$_a$].*

All stacking faults have a finite energy associated with them namely stacking fault energy. The width of these faults is related to the stacking faults energy: the lower the stacking fault energy, the wider the stacking fault. For austenitic lattices with impurities (ex. TWIP steel) as the SFE decreases, plastic deformation mechanisms are modified as follows: a) perfect and partial dislocation glide; b) slip and mechanical twinning; c) slip and martensite transformation [Humphreis2004, Curtze2010, William2007]. DeCooman et al. [DeCooman2011], illustrate in the schematic drawing below (figure 2.14) the evolution of the deformation mode of different polycrystalline materials having low (<15mJ/m^2), medium (15-30mJ/m^2) and high SFE (>90mJ/m2).

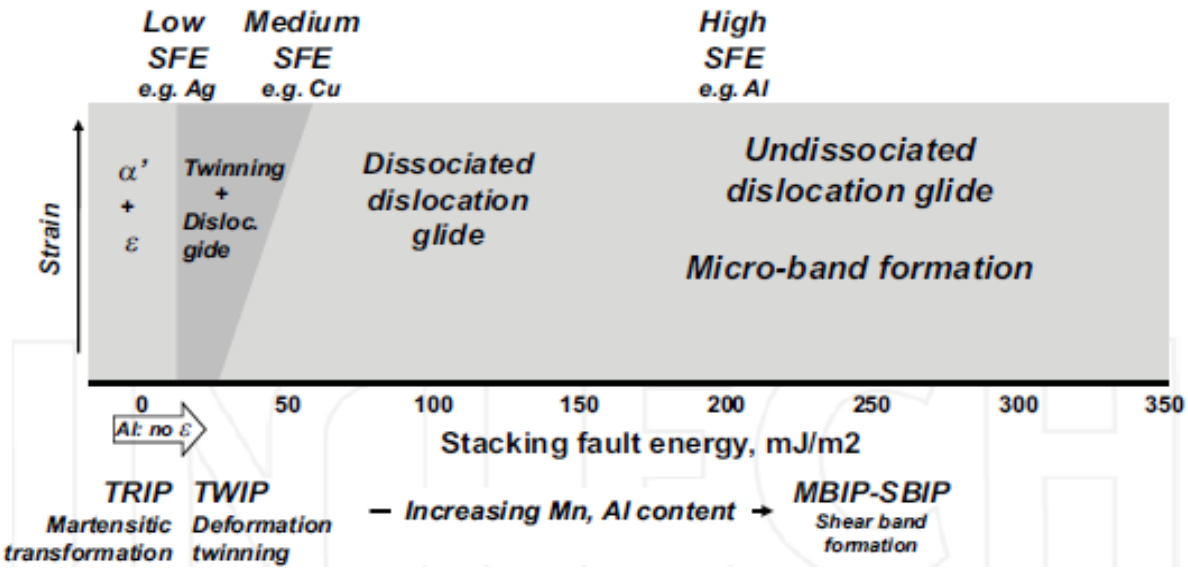

Figure 2.14– *Correlations between SFE and deformation mode in FCC materials [DeCooman2011].*

The types of heterogeneities developed during plastic deformation depends on the crystal structure, the deformation temperature, the chemical composition, the manner and rate of deformation, and especially the value of stacking fault energy (SFE). Classically, SFE of an FCC metal or alloy is believed to govern the dominant deformation mechanism according to its hardening mechanism [Kibey2007].

The different stages of hardening during a tensile test of FCC metals are illustrated in figure 2.15. It can be seen that both, twinning and cross-slip, typically observed at the onset of stage III of hardening are usually preceded by intense dislocation glide (slip activity). During this stage, depending on the value of stacking fault energy, the material will suffer twinning or cross-slip deformation. As is well-known, a low/medium value of stacking fault energy promotes twinning (Ex. TWIP steels, Austenitic Stainless Steels, Ni, Cu), while a FCC material with a high value of SFE will undergo slip deformation by deformation glide (Ex. Al-Mg alloys, Ferritic Stainless Steel).

Many authors report that in order to achieve optimal properties of a material that deforms by twinning (TWIP steel), the stacking fault energy (SFE) must be between 15 and 30 mJ/m^2 [Allain2004, DeCooman2011, Schuman1971]. Nevertheless, the critical stacking fault region to achieve twinning-induced plasticity is still unclear. Lower SFE leads to the

stress-assisted transformation of the metastable gamma phase (austenite) to alpha - α and epsilon-ε martensite. When the SFE energy increases in the range 50 to 150 mJ/m^2, twinning is also inhibited and regular plasticity takes place. Further increasing the SFE reduces the average separation distance between partial dislocations promoting wavy slip.

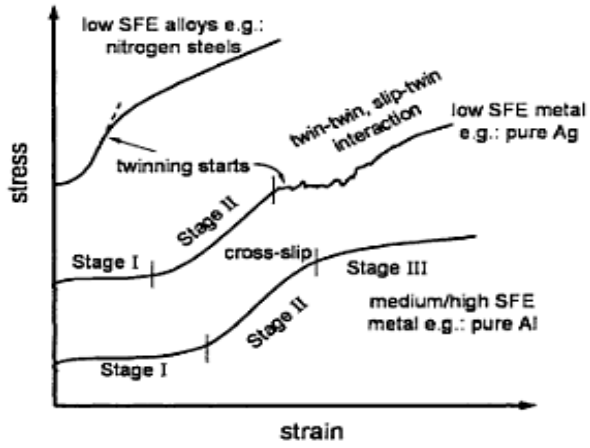

Figure 2.15– *Stress-strain curves for single crystal materials with different SFE stages of plastic flow [Kibey1999]*

Experimental Determination of Stacking Fault Energy

The measurement of SFE provides valuable information for understanding and prediction of mechanical properties, deformation substructure, microstructural stability and even the electronic configuration of metals and their solid solutions.

Whelan in 1959 [Whelan1959] measured experimentally radii of nodes of dislocations in stainless steel. Christian et al. [Christian1965] and Roy et al. [Roy2014] have made efforts to measure the stacking fault energies of metals and alloys, but no precise method had been reported. There are several techniques that allow to quantify the amount of SFE. Transmission electron microscopy and X-Ray diffraction offer attractive results in describing and analyzing the stacking fault configurations.

Hirth and Lothe in their book about the fundamentals of dislocations, propose an equation to calculate SFE after measuring the width of dissociated dislocations [Hirth1982].

$$SFE = \frac{Gb_p^2}{8\pi\Delta} \times \frac{2-\nu}{1-\nu}\left(1 - \frac{2\nu}{2-\nu} cos2\theta\right) \quad (14)$$

with G-shear modulus, b-Burgers vector of the partial dislocations, Δ - width of partials, ν - Poisson ratio and θ - angle between the dislocation line.

Youssef et al. [Yousef2011] study the influence of SFE on deformation behavior of bulk nanocrystalline (nc) Cu and Cu-alloy utilizing an in situ consolidation technique involving milling at room and liquid nitrogen temperature, which allows the intrinsic deformation to be determined without failures induced by processing defects. They were able to conclude that significant strength of nc Cu Alloys over nc Cu was enhanced due to the lower SFE of the material. This facilitates full dislocations to split into partials with a wide stacking fault ribbon and to create a high density of stacking faults that act as a barrier for the full dislocation to cross slip or climb and accordingly improve the strength of the nc Cu alloy over that of nc Cu.

Cotter and his coworkers made a similar investigation about the intrinsic stacking fault probability of aluminum alloys, silicon and magnesium as a function of their composition [Cotter1967].

The results of SFE measurements of the same material obtained by different methods showed a large scattering. A critical examination of the methods for determining the SFE resulted in the choice of X-ray diffraction method. Methods using transmission electron microscopy are the most accurate, but the use of each is restricted to 70mJ/m^2 [Reed1974, Alhers1970].

Stacking fault energy has a great influence on the mechanical properties of the materials. One aspect related to this is its dependence on solute concentration. At higher solute (ex. carbon, aluminum) contents, the SFE is reported to increase (depending on the base material). Carbon additions, less than 1 mass-% reduce the SFE to approximately 22 mJ/m^2 in Fe-22%Mn-C alloys [Yakubtsov1999]. Lu [Lu2012] studied the effect of alloying of Mn and Co on the stacking fault energy in austenitic stainless steels. He found that manganese decreases the SFE in alloys with less than 16 at. % Ni, beyond which the SFE slightly rises with Mn, while cobalt that is an hcp-stabilizing alloying element always tends to decrease γ_{SFE} in high Ni-alloys. Muzik et al. [Muzik2011] calculated using density functional theory, the stacking fault energy of aluminum and some of its alloys. After they compute the SFE as a function of alloying elements, they found an interesting implication for the design of nano-Al alloys. Alloying with Mg may improve ductility because it promotes twinning, which is considered an additional strengthening method. Tadmor and Bernstein [Tadmor2004] have shown that the tendency for partial dislocation emission and mechanical twinning in fcc

lattice depends strongly on the value of the so-called unstable stacking fault energy and unstable twinning energy. In principle this energy can be modified by addition of appropriate alloying elements.

In view of these considerations, one may propose in *Table 2* a series of SFE values of metals and alloys commonly used:

Table 2 *– Typical SFE values of different metals and alloys*

Material	SFE (mJ-m$^{-2)}$ (RT)	Source
Fe-22%Mn	30	[Yakubtsov1999]
Fe-18%Mn-0.6%C-1.5%Al.	33	[Jin2009]
Cu alloys	Twinning < 50 <dislocation slip	[Zhang2011][Youssef2011]
Al alloys	135-200	[Murzik2011]
Fe-Cr-Ni alloys	15-20	[Whelan1959]
Zinc	140	[Harris1965]
α- brass	14	[Roy2014]

Other example of the stacking fault energy dependence with mechanical behavior of the material is shown by the role played in severe plastic deformation (SPD) experiments. In different alloys, e.g. Al-Mg [Morishige2001], Cu-Al [An2008], or stainless steels [Huang2006], the minimum value of grain size (d_{min}) is found to be related strongly to the stacking fault energy (SFE). Namely, d_{min} decreases with decreasing the SFE. Hence, a relationship between grain size and SFE of the material can be written:

$$d_{min} = \frac{A\left(\frac{\gamma}{Gb}\right)^{q}}{b} \quad (15)$$

With: b the Burger vector, G - shear modulus and A, q - parameters that depend of the external loading conditions [Mohamed2003].

2.1.2.2 Types of twins

- Classification by origin

According to their origin the twins can be grouped in three categories: transformation or annealing twins, growth twins, and deformation twins [Buerger1945, Ezaz2011].
Transformation or annealing twins occur in the recrystallization process of the material, when a pre-existing crystal undergoes a transformation due to a change in pressure or temperature [Ezaz2011]. In other words, annealing twins are formed as a consequence of growth during the recrystallization (errors in the stacking of the {111} planes, which happen in a random way) [Haasen1996, Ezaz 2011]. Transformation twins appear more often in materials with law stacking fault energy because, as explained above the probability of prior defects in the original grain is much higher.

Growth twins are the result of an interruption or change in the lattice during formation or growth. Nevertheless, while the factors governing transformation and mechanical twins are clear, the formation of a growth twin is far from being well-understood, and this poses severe limitations to the synthesis of crystals of technological interest. An example of annealing and deformation twins observed in the work of Chen et al. is illustrated in the figure below [Chen2013]:

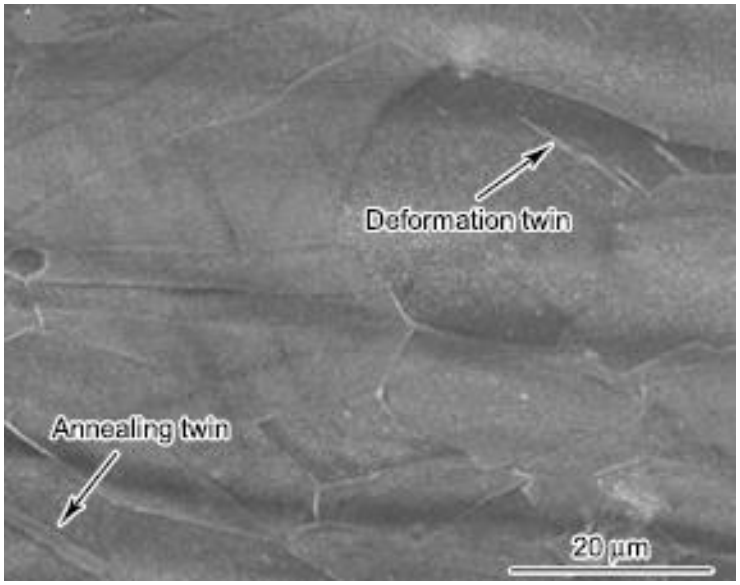

Figure 2.16 *- SEM images showing two types of twins in Fe-23Mn-2Al-0.2C TWIP steel tensile deformed [Chen2013].*

In a fcc lattice slip deformation is more favored than twin induced deformation because of the many closed-packed planes that the partial dislocations can move in. Even though deformation twinning in Al is difficult due to its high stacking fault energy, there have been several recent reports on deformation twinning in pure Al [Guan2005]. It should be emphasized that if a FCC metal like Al is subjected to extreme stresses, it will experience twinning as seen in the case of explosions.

- Classification by symmetry

With respect to their corresponding crystal symmetry one may distinguish reflection twins and rotation twins. For cubic crystals there is no distinction between these two types of twins, i.e always rotational [Klassen-Neklyudova2012].

- Classification by spatial relationship

If two twinned crystals are joined along a well-defined plane they are called contact twins and the plane of contact is called the composition plane. The rotation axis may be normal (normal twins) or parallel (parallel twins) to this composition plane [Christian2002].

2.1.2.3 Mechanism of Twin formation

Twin faults form during plastic deformation (deformation twins) as well as during solidification and recrystallization (growth twins). It should be noted that the insertion of an intrinsic fault at every plane of a FCC structure gives the twin of that structure, while an intrinsic fault introduced at every other plane gives the HCP structure.

Consistent with the shear stress, has been shown by experience that the nucleation centers for twinning are stress concentration sites. This means that twins are formed only on metals that have undergone prior slip deformation and justify the necessary condition for the nucleation of twins: prevent sliding process, forming barriers to prevent the movement of dislocations in certain restricted areas [De Cooman2011].

Reducing the dislocation mean free path and improving the work-hardening rate, deformation-induced twin result in the "Dynamical Hall-Petch effect" as illustrated schematically in figure 2.17 [Idrissi2010$_a$].

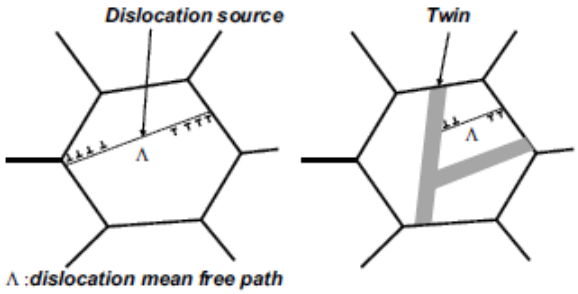

Figure 2.17*- Schematic picture of the dynamical Hall-Petch effect. Mechanical twins are formed due to the low stacking fault energy [Chen2007].*

2.1.2.4 Microstructure characterization in polycrystalline fcc materials

Mechanical twins in fcc materials form as very thin lamellae and they are considered as microstructural features. Figure 2.18 shows the twinning evolution under tension at room temperature for Fe–Mn–Si–Al TWIP steel strained to different level. It is well known that twin density (volume fraction) increase with strain. At an early stage of deformation, the main deformation mode is by dislocation glide, where sessile Frank dislocations can affect the growth and stability of a future deformation twin. During straining, overlapping stacking faults can act as twinning precursors because the passage of a partial dislocation in every Closed Packed Plane in FCC crystal result in the formation of a twin. For a strain level of 0.3 the presence of mechanical twins as thin parallel bands within the austenitic grains can be seen from EBSD micrograph (figure 2.18 a). On the other hand, the BF-TEM micrograph (figure 2.18 b,c) gives evidence that these thin bands are deformation twins in the case of a grain oriented near to the <111> zone axis.

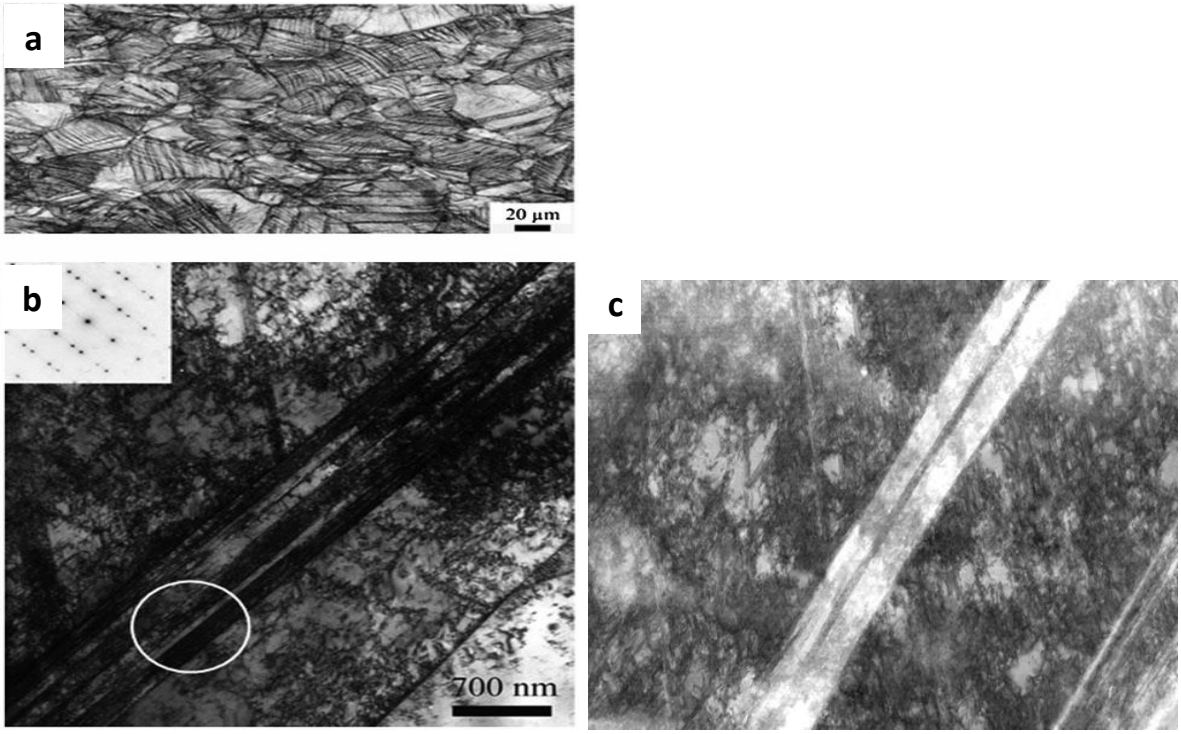

Figure 2.18 *- (a) EBSD map of the sample deformed at 0.3 true strain showing the twin population within the grains (b) BF-TEM micrograph obtained on sample deformed to 0.1. (c) TEM micrograph of a TWIP steel deformed at high strains close to fracture [Idrissi2013, DeCooman 2011]*

At moderate strains, where shear bands do not form, the twin lamellae are actually, apart from the geometrically homogeneously distributed dislocations, the only features observed in the microstructure. When the twin lamellae form at low to intermediate strains, they are no longer homogeneously distributed and the twin cluster forms "bundles" as can be seen from figure 2.19.

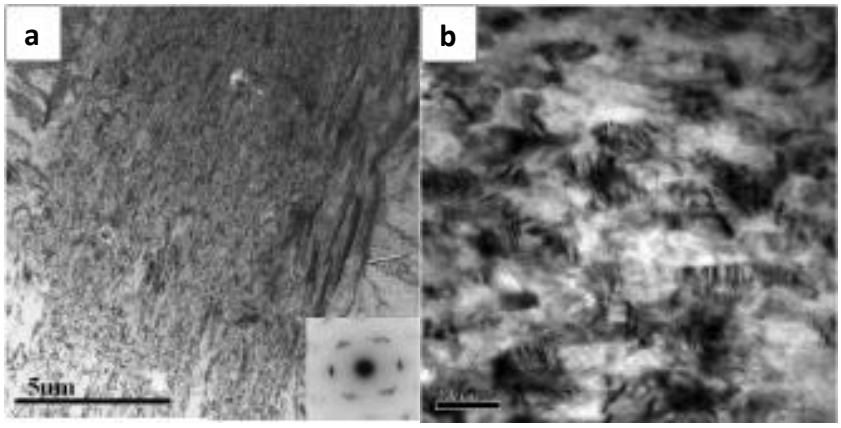

Figure 2.19– *Microstructure evolution of AZ31(a) individual twin-bundle twin bundles with high misorientations as suggested by the rings on the diffraction pattern at 0.77 true strain; (b) detailed microstructure within the twin-bundle in (a) at high magnification. Original twins were divided into smaller subgrains or grains with different orientations [Liang2012].*

The twins had an angle/axis misorientation relationship of 60°±5|<111> with the neighboring grain. At the large strain region (figure 2.18 c), the development of the pronounced <111> fiber in the rolling direction sustains deformation twinning and maintains the high strain hardening rate. With increasing deformation up to fracture, formation of different twin configuration with the occurrence of a secondary twin system seems to be the only mechanism governing the microstructure of fcc metals. These deformation twins could, however, be differentiated from annealing twins on the basis of their morphology and size. They mainly nucleated on grain boundaries and propagated across the grains. However, a study of the evolution of twinning density with strain and strain rate for TWIP steel presented in Chapter 5 will demonstrate a more unusual behavior. More intense twinning occurs with decreasing strain rate.

2.2 Factors that influence sheet metal forming processes

A good understanding of the deformation processes, of the plastic flow localization and of the factors limiting the forming of sheet metal is of key importance in monitoring the formability issue. Therefore, the main factors which best illustrate the physical basis of Al-Mg alloy and TWIP Steel formability will be presented in this section.

2.2.1 Dynamic strain aging (DSA) and the associate Portevin-LeChatelier effect (PLC)

Strain aging is a phenomenon of the interaction between interstitial or substitutional atoms and dislocations in steels or other metals [Stewart2004, Xu2006, Picu2004, Vincze2007]. There are two types of strain aging: static strain aging (SSA) and dynamic strain aging (DSA). While the SSA occurs after plastic deformation and when the material has aged for a period of time, DSA occurs during deformation and it is caused by the interaction between the moving dislocations and solute atoms.

65 years ago Cottrell and Bilby [Cottrell1949] proposed that strain ageing effects are due to the segregation of interstitial solutes to form atmospheres around dislocations, which then require an increased force to break away from these atmospheres to become mobile. There is, however, no clear consensus yet as to details of the mechanism of the DSA, although the Cottrell model became the basis for much of the study of strain ageing. In order to better understand this complex phenomenon of dynamic strain aging Picu [Picu2003] investigated first the physics at the atomic scale. They began by testing the validity of some previously proposed atomic scale mechanisms for DSA. This was performed by means of atomistic simulations of diffusion of Mg in Al. They demonstrated that the commonly accepted mechanism is not operable because Mg diffusion is too slow. According to the classical mechanism for DSA, mobile dislocations have an intermittent motion. They get arrested at forest dislocations or other obstacles in their glide plane. During this arrest time, solute diffuses toward mobile dislocations either through the bulk or along the core of the mobile dislocation, effectively pinning it. The longer the mobile dislocation waits at an obstacle (inversely proportional to the strain rate), the larger the stress required to put it back in motion. This leads to negative strain rate sensitivity [Picu2003].

The macroscopic manifestation of DSA consists of discontinuous (or serrated) plastic flow in the stress-strain curve during loading. These irregularities were first studied in detail by Portevin and Le-Chatelier in aluminum alloys [Portevin & Le Chatelier1923] i.e *Portevin Le Chatelier effect* (PLC). This result, which severely limits ductility/formability is manifested by the repeated strain localization bands that leave undesirable traces on the surface of the final product. In general, two types of instabilities observed in a variety of f.c.c. and b.c.c.

metals and alloys are associated with strain aging: Lüders front (figure 2.20) and the Portevin Le-Chatelier (PLC) effect (figure 2.21).

Due to pre-yield micro-strain, in uniaxial tension, an upper stress yield is observed with apparition of Lüders bands. It appears at one end of the specimen and propagates with typically constant velocity, if the cross–head velocity is kept constant, towards the other end [Butler1962]. Subsequently, stress decreases abruptly and stress plateau follows while bands propagate (fig. 2.23). Once the gauge is covered by the bands, strain hardening proceeds.

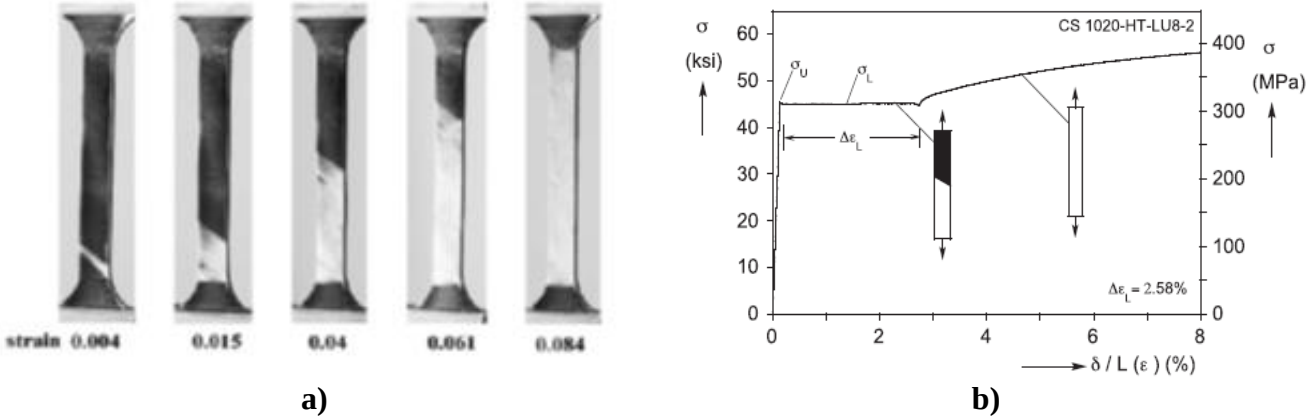

Figure 2.20 *- (a) Experimental records of the propagation of Lüders bands: single bands [Sun2003]; (b) Lüders strain on a generic material [Hallai2011].*

Signature of PLC effect can be seen from the fig. 2.21 as a function of temperature. In this situation, the flow instability appears as a series of serrations observed during strain hardening that continue until the fracture of the sample.

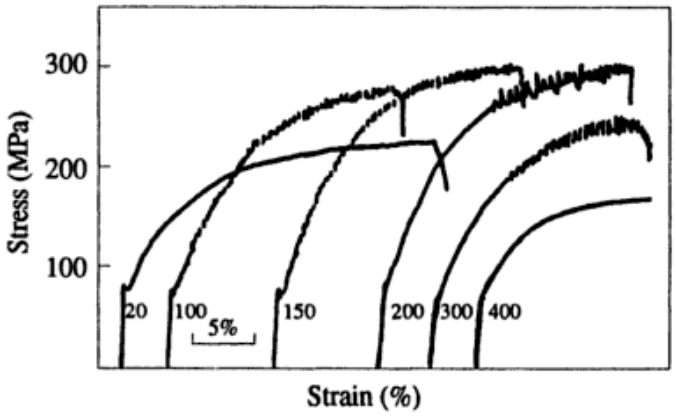

Figure 2.21 *- Portevin Le-Chatelier effect in mild steel tested at $10^{-4}s^{-1}$ at different temperatures [François1998].*

In the literature, this effect is observed in some ranges of temperatures and strain rates for which negative strain rate sensitivity is observed. Consequently the coupling between strain aging and plastic deformation depends on plastic strain (the microstructure), strain rate and temperature. Moreover, a material can be sensitive to DSA without exhibiting PLC effect (ex. TWIP steel).

For tensile tests at constant applied strain rate, three types of PLC effect, type A, B and C, are distinguished according to their different spatiotemporal aspects. The ranges of applied strain rates, grain size or temperature are factors influencing which type of PLC effect will occur. Figure 2.22 illustrates different types of serration observed in AA5185 aluminum alloy, tested at room temperature on strain rate range between 10^{-4} and $10^{-1}s^{-1}$ (the curves have been shifted on y axis to see better the differences between the serrations).

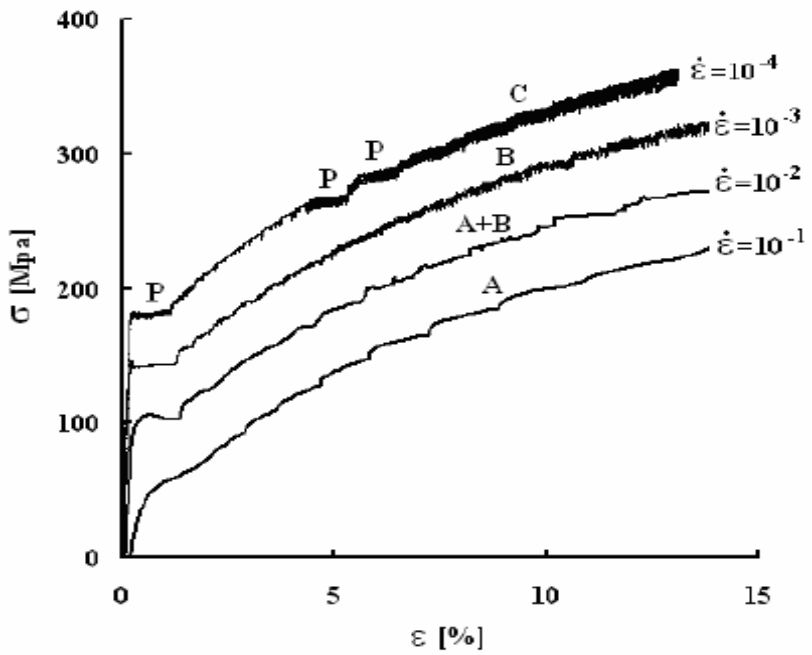

Figure 2.22*- Stress-strain curves showing bands types on the apperance of Portevin LeChatelier effect in an Al-Mg alloy tested at room temperature [Vincze2007].*

- At low strain rates or high temperatures *type C* bands appear at random in the space.
- At medium strain rates *type B* ("parallel bands") bands exhibit an oscillatory or intermittent propagation along the tensile axis. They appear as diagonal bands oriented

approximately 50º to the tension axis [Vincze2007]. The serrations are more irregular with smaller amplitudes than type C [Ananthakrishna2007].

- At high strain rates or low temperatures *type A* ("flamboyant") bands propagate over the entire specimen, continuously and smoothly as solitary plastic waves. Type A Lüders lines is associated to a plateau on the load-extension curve arising just after yielding. They appear on annealed or heat treated solid solution alloys, such as aluminum-magnesium and low carbon steel. They are usually described as continuously propagating with small stress drop at the onset of plastic flow. It is associated with localized deformation in thin bands [Sarkar2005, Vincze2007].

2.2.2 Strain rate sensitivity

Since the SRS is the one of the central themes of this work, it is briefly described in the following paragraphs. As the work will proceed, the parameter will be specifically analyzed for each material in part. Literature data shows that DSA is one of the responsible for the macroscopic negative strain rate sensitivity of the flow stress.

The concept of strain rate sensitivity was introduced by Penning, assuming that the strain rate hardening is negative over a finite interval of strain rates [Penning1972]. The reason for this decrease is based on dislocation motion that makes possible the increase of the concentration of the solute atoms while a dislocation is held up at an obstacle [McCormick1978]. The longer the waiting time, the higher the stress necessary for the dislocation to overcome the obstacle, and this leads to the negative strain rate sensitivity. Later on, Kubin and Estrin [Kubin1985] developed a model through instantaneous jumps where they explain and define the critical strains for the occurrence of the PLC effect in terms of the strain dependence of the mobile and forest dislocation densities.

In figure 2.23 are presented the consequences of mechanical properties under the influence of DSA. With the increasing of the temperature, the yield stress, the ductility "*A*" and SRS of the tested material generally decreases while the mechanical strength "*Rm*" shows an increase. In some cases, it is possible to see an apparent levelling or even an increase of the

yield stress with increasing temperature, but this happens only in the range of strain rates and temperatures in which negative SRS is also observed.

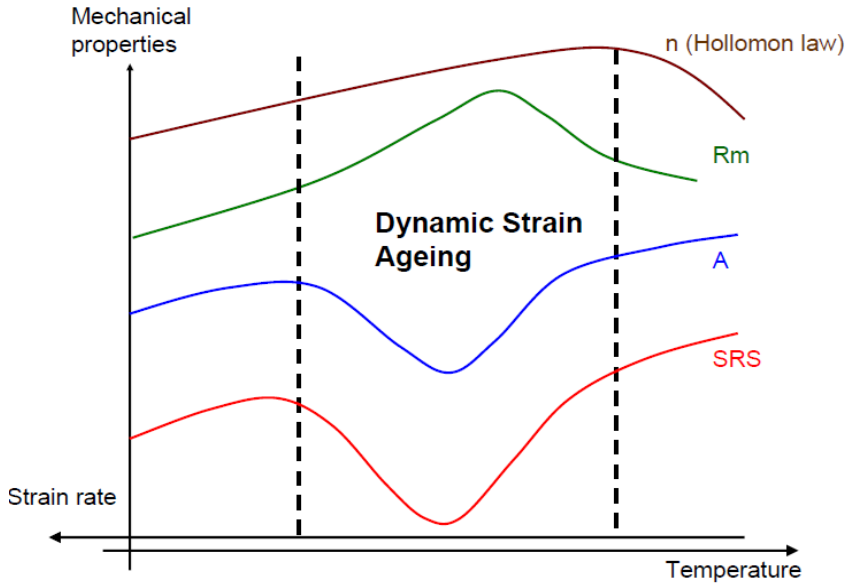

Figure 2.23– *Synthetic view of the tensile mechanical properties with respect to dynamic strain aging [Graff2006]*

In the literature many authors calculated and reported low or negative values of the strain rate sensitivity for different materials. For example Picu et al [Picu2005] observed PLC effect and hence negative SRS in AA 5182 Al-Mg alloys at all temperatures between −80 and 110 ^{o}C and at strain rates lower than 10^{-1} s^{-1} (figure 2.24). They offer a new explanation based on experimental explanation and model prediction for the negative SRS domain. Low positive values of the strain rate sensitivity were observed by Korbel et al. [Korbel1976] in 316 stainless steel and Cu-Zn alloys. Recent work by Chun and his co-workers [Chun2011], suggest that increased activity of contraction twinning at higher strain rates can lead to negative SRS and a decreasing trend of the coefficient with strain. Another material which displays a similar trend for SRS is Cu. Shen et al. in their work demonstrate that the increase in twin spacing is likely to be responsible for the decrease of *m (strain rate sensitivity)* vs. strain [Shen2006].

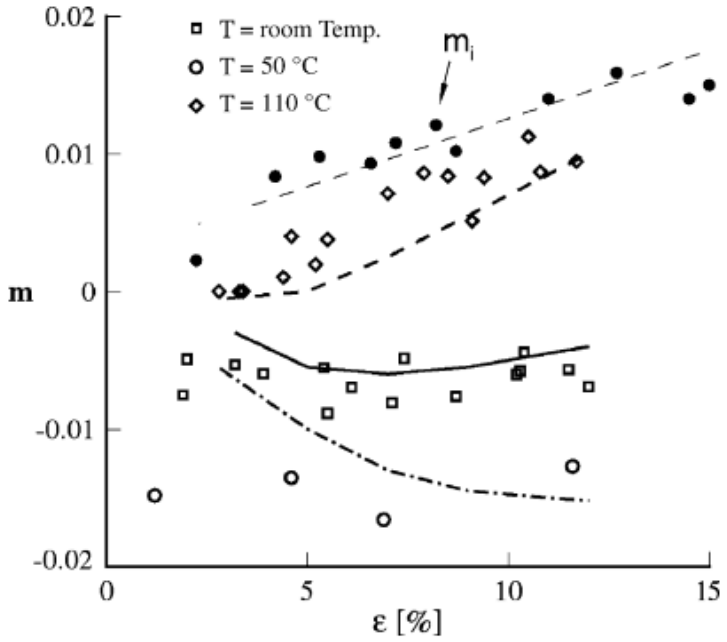

Figure 2.24 *- Variation of the strain rate sensitivity parameter m with strain at three temperatures within the negative SRS range. The open data points are obtained from strain rate jump tests, while the curves correspond to constant strain rate experiments. The filled symbols correspond to the instantaneous rate sensitivity, mi, and the dashed straight line is a fit to the data. [Picu2005]*

The rate at which the strain is applied can have an important influence on the plastic flow [Dieter1984]. The strain rate is defined as $\dot{\varepsilon} = d\varepsilon / dt$, and is usually expressed in s^{-1}. The strain rate influences the flow stress of a typical metal as shown in figure 2.25. It is observed that yield strength and ultimate tensile strength increases with increasing strain rates.

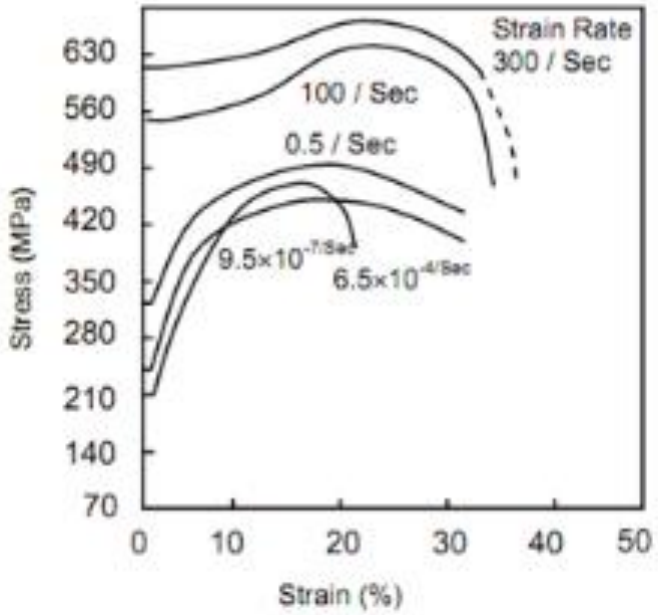

Figure 2.25 - *Strain vs Stress for mild steel at different strain rates*

True strain rate is given by the expression:

$$\dot{\varepsilon} = \frac{d\varepsilon}{dt} = \frac{d[ln(\frac{l}{l0})]}{dt} = \frac{1}{L}\frac{dL}{dt} = \frac{v}{L} \qquad (16)$$

where *v* is the grip displacement speed.

This equation shows that for a constant speed of the testing machine, working in tension, the true strain rate is decreased while the sample is elongated, so to keep constant the speed of deformation, the spindle speed must be increased in proportion with the increase in the length of the piece. The dependence of the plastic flow stress on the strain rate at constant temperature can be approximated with [Askeland1987]:

$$\sigma = C(\dot{\varepsilon})^{m}_{\varepsilon,T} \qquad (17)$$

In which *m* represents the strain rate sensitivity parameter. The exponent '*m*' can be obtained from the slope of the plot ln σ against ln $\dot{\varepsilon}$.

$$\boxed{m = \frac{\log(\sigma_2/\sigma_1)}{\log(\dot{\varepsilon}_2/\dot{\varepsilon}_1)}\Bigg|_{\varepsilon}} \qquad (18)$$

Where for a given strain Ɛ, the stress level σ_1 and σ_2 is measured for the different $\dot{\varepsilon}$. In the curve log (σ) vs. log (ἐ), the slope gives the *m* value. The instability domain starts with necking. At that point, there is flow localization, where the strain rate is different than the one applied by the machine. If the strain rate sensitivity is high, there will be a uniform propagation of the defect, and a relatively long straining of the sample occurs before fracture. On the other hand, if the *m* parameter value is negative, the necking will increase quickly and fracture occurs almost immediately.

2.2.3 Grain size

The grain size (or average grain diameter) of polycrystalline metals have great influence on their mechanical properties. Adjacent grains normally have different crystallographic orientations and, of course, a common grain boundary. During plastic deformation dislocations have to cross grain boundaries which therefore act as a barrier to dislocation motion for two reasons [Cao2003, Zhilyaev2008]:

- Since the two grains have different orientations, a dislocation passing into one of it will have to change its direction of motion, and as the crystallographic disorder increases this becomes more difficult.
- Atomic disorder in a grain boundary region will result in a discontinuity of slip planes from one grain to another.

These two reasons explain the increase of yield stress (σ_y) when the grain size (*D*) decreases, as the Hall-Petch equation expresses [Hall1951, Petch1953]:

$$\boxed{\sigma_y = \sigma' + KD^{-1/2}} \quad (19)$$

In this expression, *D* is the average grain diameter, and σ ' and *k* are constants that depend on the material. In other words, the yield stress of coarse-grained materials is inversely proportional to the square root of the grain size. But as Van Swygenhoven explains, at nanometer scale grain sizes this expression no longer holds, because a change in deformation mechanism is observed [Van Swygenhoven2002]. The interpretation is based on the

dislocation sources inside grains that can hardly exist because of size and image force limitations and the more important role sources at grain boundaries play.

A graphical representation of Hall-Petch law of a Cu-Sn Alloy can be seen from the figure 2.26 below.

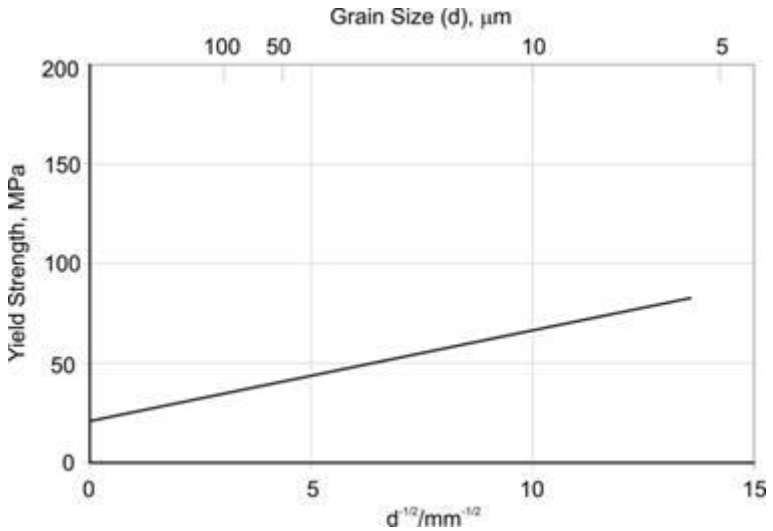

Figure 2.26 *– Typical $\sigma_y - D^{-1/2}$ curves of a metallic material for different deformation levels described by Hall-Petch law [Aoyama2010]*

Materials grain sizes may evolve due to recrystallization process whereby the internal energy level of the material, i.e. the grain boundary energy and the stored energy, is lowered. The nature of the dynamic recrystallization depends on the type of material under consideration. The recrystallization process in materials of low stacking fault energy, such as TWIP steels or Cu, is mainly a discontinuous process where new grains nucleate at sites in the microstructure that have enough stored energy [Hallberg2010]. In materials of higher stacking-fault energy, such as aluminum, dynamic recovery processes limit discontinuous dynamic recrystallization in favor of a continuous process. Najafi-Zadeh reported ferrite grain refinement in Interstitial Free steels by warm rolling [Najafi1992]. They concluded that dynamic recrystallization was responsible for decreasing the ferrite grain size to 1-3 μm.

Grain boundaries

As explained above, grain boundaries are interfacial defects created between two grains that have different crystallographic orientations. The properties and structure of grain boundaries are a function of the misorientation, so it is convenient to separate them in terms of the extent of the misorientation.

The misorientation at the boundary can be described as the transformation necessary to rotate the normal vector of one grain onto that of its neighbor.

A boundary is considered "low-angle" (LAGB) if it has a misorientation angle of less than 15° while a high-angle boundary (HAGB) is any boundary with a misorientation angle greater than 15° [Humphreis2004]. The simplest LAGB is a tilt boundary where the structure can be described in terms of dislocation arrays, consisting of a wall of parallel dislocations [Hull1965, Cui2000]. They are entirely formed of edge dislocations. HAGBs have a higher energy content than LAGB and are more mobile due to the consequently lower activation energy to move the boundary. The dislocations traverse the boundaries during deformation, but this requires higher stress and gradual accumulation of dislocations in pile-ups. In this case, the misorientation can be described in terms of a relative rotation of two grains relative to each other.

Dislocation motion in fine grain sized material is modified by the presence of grain boundaries [Derlet2003]. Small angle grain boundaries do not effectively block slip due to slight crystallographic misalignment. Moreover, the twinning boundaries block effectively the sliding process and increase the strength of the material. The boundary between two different phases are also strong obstacles for dislocations.

Effect of grain size on mechanical properties of crystalline materials

Reducing the grain size of a crystalline material has a great influence on its mechanical properties. With the decrease of grain size, the material's ductility at room temperature generally decreases but its strength increases greatly [Bintu2016]. The research of Kumar et al. show that the strain hardening exponent, n and the average plastic strain ratio, both increase with increasing grain size of low carbon steel [Kumar2002]. Another example is

presented in the work of Lopes, where, for the same material (low carbon steel) the author show a reduction of uniform deformation for sample with grain size equal to 20 μm. When comparing with samples with grains sizes with 40μm and 80μm, the authors present a reduction of about 20% and 30% respectively [Lopes2001].

The reason for this result may be associated with a decrease of the uniform deformation with decreasing grain size, which is a direct consequence of more accentuated decrease of work hardening rate associated with dislocation accumulation during plastic deformation. Calcagnotto and his coworkers investigate also the effect of grain refinement on strength and ductility in Dual-Phase Steels by applying hot deformation and large strain warm deformation at different temperatures [Calcagnotto2009]. Their deformation and fracture mechanisms were studied based on tensile data and microstructure observations (figure 2.27). They conclude that grain refinement leads to an increase of both yield strength and tensile strength. Uniform elongation and total elongation are also affected. The UFG (ultra-fined grain) steel has a lower total elongation than the CG (course-grain) steel, but has a higher reduction in area. Initial strain hardening rate and reduction in area increase as the grain size decreases.

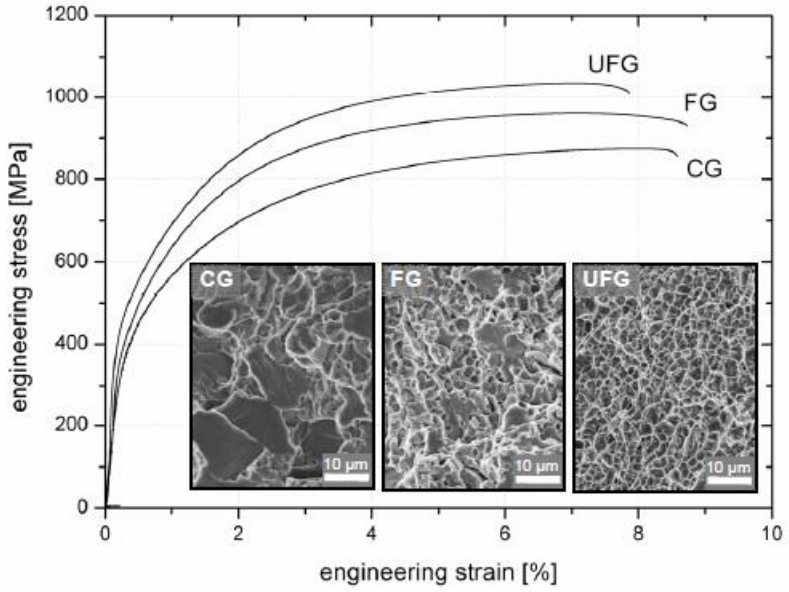

Figure 2.27 *– Mechanical properties of Dual-Phase Steel due to grain refinement. The inserted micrographs reveal the respective fracture modes of the steels [Calcagnotto2009].*

The critical strain for the onset of the serrated flow characteristic for Al-Mg alloys is dependent on the grain size as the work of Wagenhover relates [Wagenhofer1999]. Moreover, this present study will demonstrate later on, in *Chapter 4* the validity of this observation.

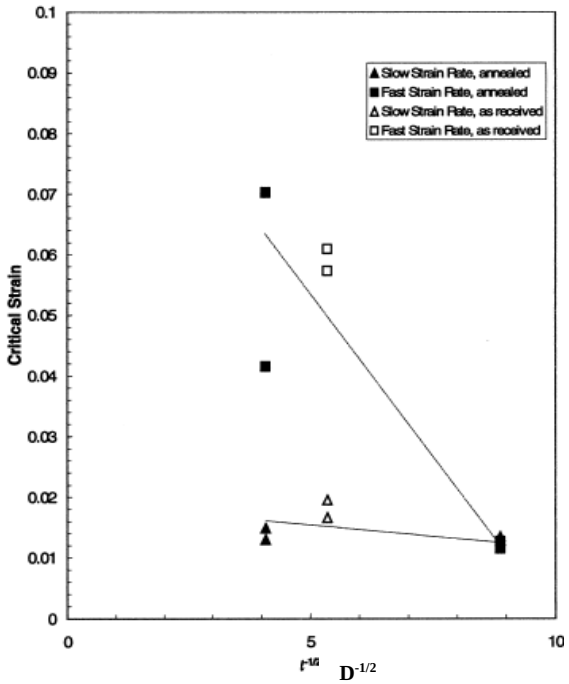

Figure 2.28 *- Variation of critical strain for the onset of serrated flow with grain size for Al-Mg5086, after fast and slow strain rate [addapted from Wagenhofer1999].*

From the figure 2.28 it can be seen that as the grain size increases from 13 to 61 μm, the critical strain for the onset of serrated flow increases as well.

Grain refinement techniques

During the last few decades, the severe plastic deformation (SPD) technique has been proposed to produce grain refined bulk metals [Valiev2004, Ahzi2008]. Some of the most investigated techniques are asymmetric rolling [Ji2009] and equal-channel-angular pressing (ECAP) [Valiev2006]. These methods require subjecting the material to large plastic strains and the resulting sample has preferential texture and reduced grain size. Just recently, other technique based on powder metallurgy, found its place in grain refinement processes. The procedure involves a nanoscale (or bimodal) powder of a metal or alloy, and subject it to sintering using a novel spark plasma technique (SPS) [Diras2009]. In this technique, the material is compressed at room temperature and a high intensity electric current is passed through, leading to sparks between granules and their eventual sintering. The procedure is advantageous since the mean temperature of the material remains low and grain growth is limited. This technique does not lead to preferential texturing in the sample and is ideally

suited to produce microstructures with desired grain distribution. SRS parameter of FCC materials in general usually increases regardless of the different technical routes used to produce the UFG/NC metals [Wei20007]

Between these grain refinement techniques, asymmetric rolling was selected in the present study to produce ultra-fined grains in AA5182 alloy sheet. Therefore, details and description of the method together with the discussion of the effect of UFG AA5182 on the strain rate will be given in the next chapter.

2.2.4 Temperature

The mechanical behavior of a sheet metal can significantly change with the variation in processing temperature. Under various temperatures the material will react differently to the same manufacturing operation i.e., may show different mechanical, physical and chemical properties.

The temperature at which a test is conducted has a strong impact on the stress-strain curve, as well as on the properties of plastic flow and fracture. Generally, the strength is reduced while the ductility is increased as the temperature increases. However, at certain levels of temperature structural changes may occur such as precipitation, strain aging or recrystallization that modifies regular behavior of materials [Dieter1984]. For these reasons, it is very important to understand the behavior of metals at various temperature ranges. For instance, at high temperatures, dislocation annihilation (reduction in material's strength) is mainly controlled by the climb of dislocations, a process controlled by the diffusion of vacancies; deformation twinning requires the dissociation of dislocations into partials and the formation of twin boundaries.

In industrial forming manufacture, there are three basic temperature ranges at which the metal can be formed, cold working, warm working, and hot working. Cold forming refers to forming at temperatures below the re-crystallization temperature of the metal. The strain hardening during the process improves the mechanical properties of the product. Hot forming is defined as forming at temperatures above the re-crystallization temperature of the metal, resulting in a decrease of yield stress and hence reduces the flow stress of metals.

Warm forming has come to be used in order to gain the advantages of hot as well as cold forming, though to a lesser extent. Since yield strength decreases with increase in temperature, the load on the equipment in warm forming is lower than in cold forming. Also the temperatures are not that high such that the surface layer damage can occur. Therefore, the advantages of cold forming are achieved, that is, better surface quality, better dimensional accuracy and better mechanical properties than in hot forming.

Figure 2.29 and 2.30 shows schematically the changes in the stress-strain curves that occur with changing temperature for Hadfield steel and Al-Mg alloy respectively.

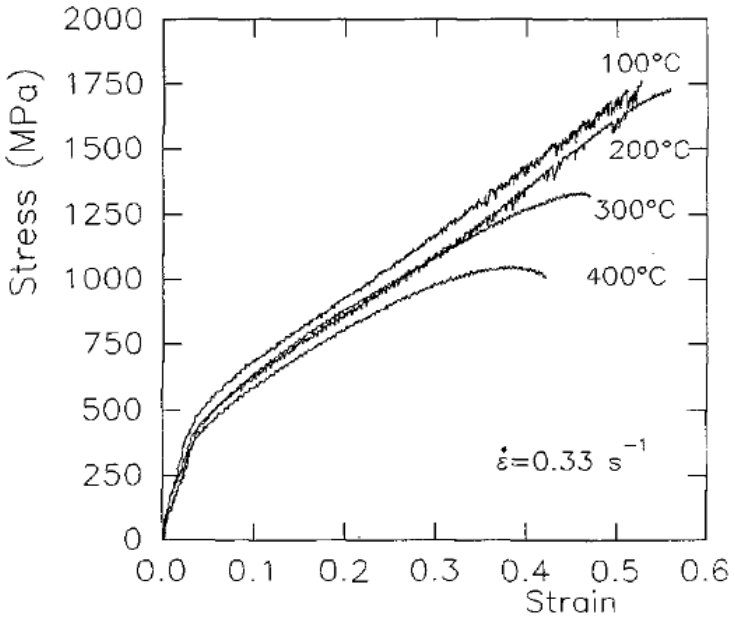

Figure 2.29 *- Stress–strain curve of Hadfield steel at different temperatures obtained from tensile test results [Bayractar1993].*

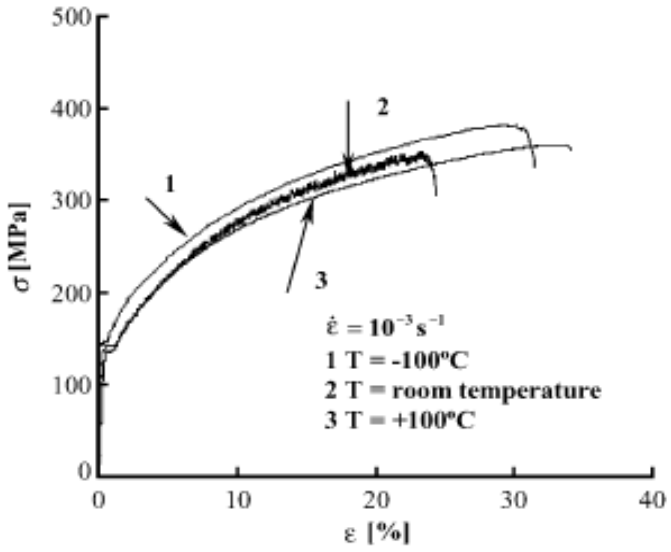

Figure 2.30 *- Stress–true strain curves for AA5182 Al-Mg alloy at three temperatures within and outside the PLC range [Picu2005].*

It is difficult to establish a generally valid relationship between yield strength, temperature, strain and strain rate because of complex behavior of metals, however, there are quite a few attempts to empirically describe the flow stress of certain metals as a function of these variables in specific temperature ranges.

The dependency degree of plastic flow stress with temperature at constant deformation and deformation rate is generally expressed by [Willkinson2003]:

$$\sigma = Ce^{Q/RT} \tag{20}$$

Where: Q - activation energy of the plastic flow, cal / mol

R - Universal constant of gases, 1.987 cal $K^{-1}mol^{-1}$

T - Specimen temperature, K

The value of the flow stress depends on the structure of dislocations existing at the time the stress is measured. Dislocation structure is modified with temperature, strain and strain rate.

2.2.5 Anisotropy

It is well known that crystallographic texture is one of the main factors influencing plastic anisotropy [Bunge1982]. The ratio between the sheet's deformation in width and its deformation in thickness, for a given set of conditions, is called anisotropy or the Lankford coefficient and is given by:

$$r = \frac{\varepsilon_{YY}}{\varepsilon_{ZZ}} \quad (21)$$

Where, ε_{yy} is the deformation on width of the specimen and is given by $\varepsilon_{YY} = \ln\left(\frac{w}{l_w}\right)$ and ε_{zz} represents the deformation on thickness along the sample and is defined as $\varepsilon_{ZZ} = -(\varepsilon_{XX} + \varepsilon_{YY})$ with $\varepsilon_{XX} = \ln\left(\frac{l}{l_0}\right)$ (w_0 and w are the initial and final width, while l_0 and l are the initial and final gauge length of the specimen, respectively).

Equation 21 has to be modified considering the measurement system:

$$\boldsymbol{r} = -\frac{\varepsilon_{YY}}{(\varepsilon_{XX}+\varepsilon_{YY})} \quad (22)$$

The planar and normal anisotropies are calculated from three values at specific directions with respect to the rolling direction usually 0º, 45º and 90º. Consequently, the planar anisotropy coefficient is given by [Banabic2010]:

$$\Delta r = (r_0 + r_{90} - 2*r_{45})/2 \quad (23)$$

And the normal anisotropy is given by:

$$\bar{r} = (r_0 + r_{90} + 2*r_{45})/4 \quad (24)$$

A high normal anisotropy value means that the thickness is decreasing less than the width and it is an advantage for forming processes. On the other hand, if the r-value is smaller than one, the thickness is thinning quicker than the width and that would cause rapid failure (fig. 2.31)

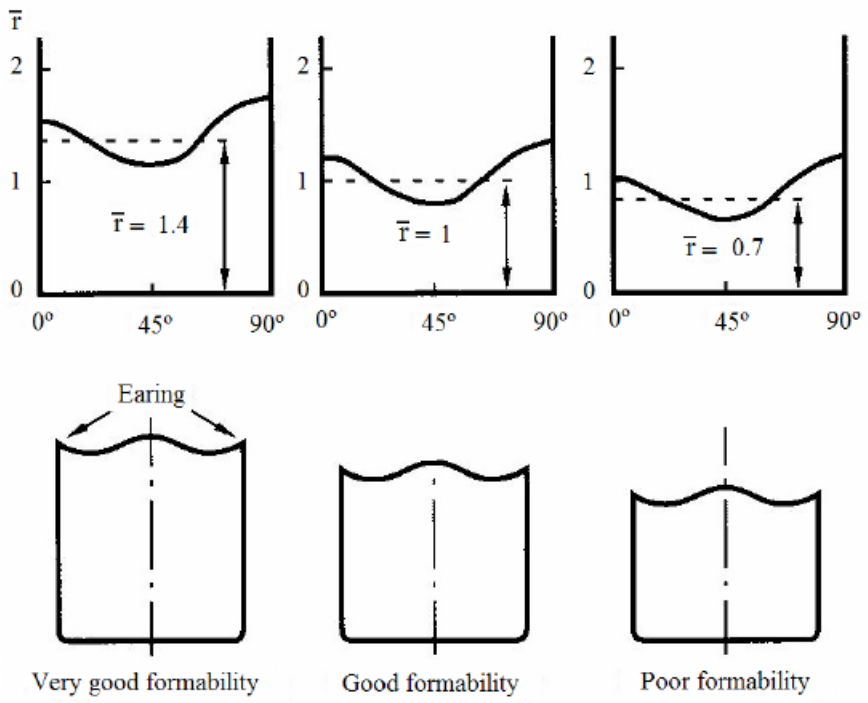

Figure 2.31 *- Effect of normal anisotropy on formability for positive planar anisotropy*

A more intuitive image of the planar anisotropy for AA5182-O is given by polar coordinate representation in the book of Banabic [Banabic2010]. Figure 2.32 shows the planar variation of the anisotropy with respect to the orthotropic behavior of the sheet metal.

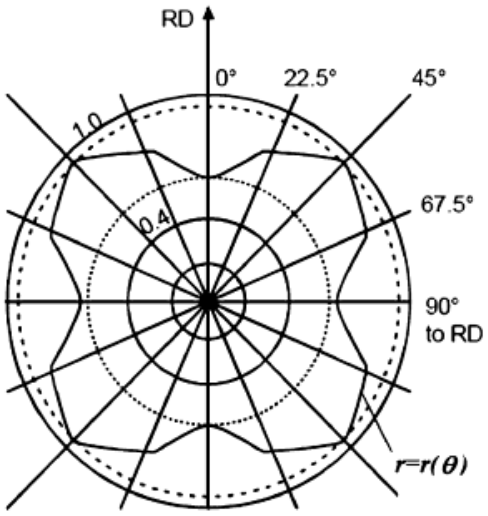

Figure 2.32 *– Variation of the anisotropy coefficient with respect to the plane of the metal sheet [Banabic2010.*

Understanding the texture of a material is fundamental for the characterization of its microstructure and physical properties. Therefore, the anisotropy of the mechanical properties of the materials plays a vital role on the material behavior during forming processes and consequently on its formability.

2.2.6 Strain hardening

The strain hardening behavior is generally used to evaluate the flow localization resistance of materials. When a material undergoes deformation, in order to have more uniform thinning, it has to spread deformation to its neighboring regions by increasing the stress to promote slip. Therefore, strain hardening promotes stable plastic flow and retards the onset of necking.

Two parameters are generally used to describe the strain hardening behavior of metals and alloys: Strain hardening rate: $\theta = \frac{\partial \sigma}{\partial \varepsilon}$ and the strain hardening parameter: $n = \frac{\partial ln\sigma}{\partial ln\varepsilon}$

Temperature has a strong influence on both θ and n. With increasing temperature, the strain hardening rate generally diminishes due to the decrease in the saturation concentration of immobile dislocations. The strain hardening coefficient presents a similar behavior with decreasing temperature. A good formability of sheet requires a high n value (0.2-0.5) at room temperature.

As mentioned before in section *1.1.1.1*, above the critical resolved shear stress can be observed three work-hardening stages. The extent and hardening rate of the 3 stages depend on the metal sheet, impurities, temperature and the orientation of the applied load. For example, the hardening rates in Stages I and II are insensitive to temperature whereas the Stage 3 hardening rate decreases with temperature.

Classical expressions developed over the years for description of the flow stress (σ) are:

Hollomon: $\sigma = K \cdot \varepsilon^n$ (25)

Swift: $\sigma = K(\varepsilon_0 + \varepsilon)^n$ (26)

Voce: $\sigma = A - Bexp(-C\varepsilon)$ (27)

With *K*, *A*, *B* and *C* material parameters.

Grain size, DSA, strain rate or dynamic recovery effects play important roles in the strain hardening behavior of materials. Moreover, strain hardening depends on the type of metal deformation. It is shown later in this work that the pronounced <111> fibre texture in the rolling direction sustains deformation twinning, which maintains the high strain hardening rate. Also, the present thesis will offer an excellent occasion to study the mechanical properties of TWIP steel by analyzing its strain hardening behavior.

CHAPTER 3

Materials and experimental procedures

CHAPTER 3 - Materials and experimental procedures

Firstly, in this section, the characteristics and properties of AA5182 aluminum alloy and TWIP steels will be reviewed. The discussion of each material will begin with an analysis of the mechanical properties, followed by an examination of the microstructure. This division will briefly encompasses the materials information which is necessary for carrying out the present research. A correlation between the mechanical properties, deformation behavior and possible applications of each material was also done.

The second part of this chapter focuses on the description of equipment used for mechanical tests of both materials. Finally, the third section summarizes the different methods used for microstructural characterization of the sheet metals in several stages of the work.

3.1 Materials studied

3.1.1 AA8152

Aluminum alloys are important technological materials primarily due to their advantageous strength to weight ratio. Among different aluminum alloys (from 1XXX series to 7XXX series), Aluminum Magnesium alloys (5000 class includes non-heat treatable alloys which are solid solutions of Al and Mg) have great potential as lightweight strong material due to its combination of low density (ρMg = 1.8 g/cm^3 and ρAl = 2.7 g/cm^3) and good corrosion resistance. As it is an alloy with good development prospects for further development, the investigation of Al-Mg alloys makes an interesting choice for the present thesis.

3.1.1.1 Overview of the mechanical behaviour

In many important industrial applications, such as aerospace, automotive and packaging, economic and environmental concerns have driven the need for lighter but safer structures.

The presence of magnesium as the major alloying element in 5XXX series leads to solute hardening of the material resulting in excellent properties like good strength level, high corrosion resistance, good weldability, low cost maintenance and great recycling potential.

Al-Mg alloys ensure at least 10% lower production costs compared to the other suitable Al-alloys, making them most attractive for sheet metal forming operations. Moreover, by using light-weighing Al-Mg alloy, weight savings of different parts in car body structures up to 50% can be achieved [Hirsch2011]. Such considerations make attractive the further research and improvement of the high strength Al-Mg sheets. Nowadays, the alloy is chosen for parts like power train, chassis, car body, bumpers and interiors, but mostly in high level class cars. Some examples of aluminum magnesium alloys used in automobile body applications are presented in figure 3.1.

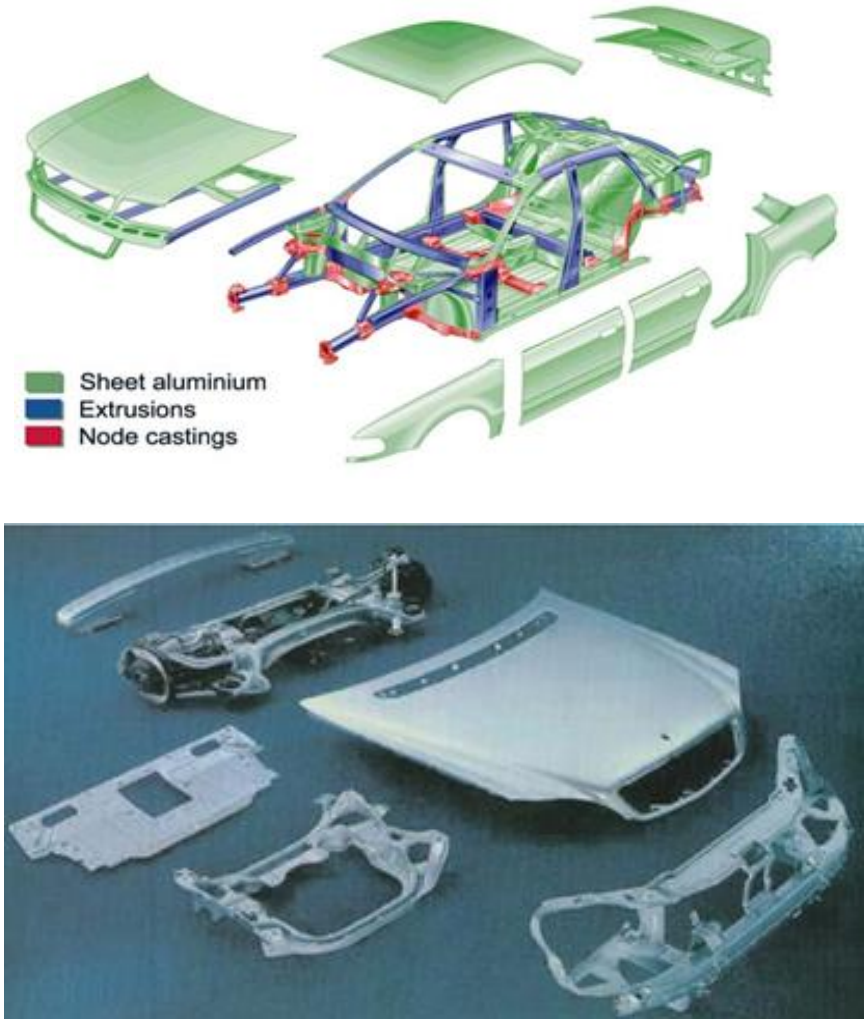

Figure 3.1 *- Applications of aluminum alloys on automotive industry: a)Audi A8 Space-Frame, b)Aluminum (AA5182) parts of the S-class Mercedes [www2].*

However, the deformation of these alloys at room temperature is discontinuous, with the strain localizing in narrow bands that leave undesirable traces on the surface of the final product. Figure 3.2 shows an unwanted surface appearance of AA5182 alloy sheet. These macroscopic marks damage product appearance and for some product groups, the visual appearance and optical properties of the material are of great importance.

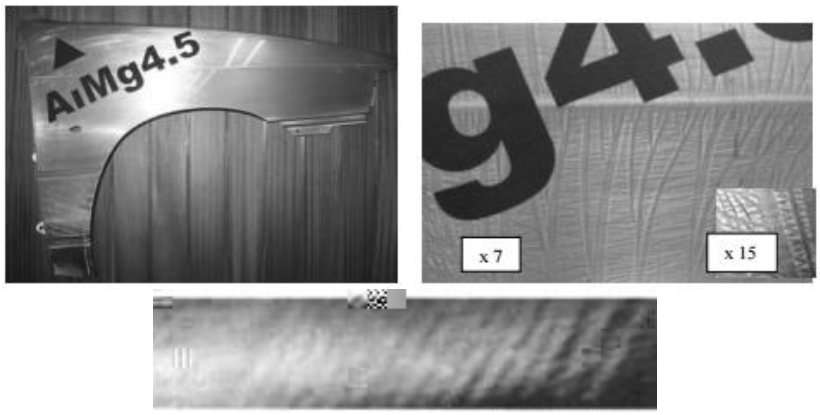

Figure 3.2 - *Photographs of the surface appearance at the fender made of AA5182 alloy sheet due to the PLC effect [Romhanji2002].*

The effect, which also severely limits ductility/formability is the signature of the Portevin-LeChatelier phenomenon (PLC). The repeated strain localization is due to the negative (SRS) of the material which, in turn, is caused by smaller scale phenomena associated with interactions between solute atoms and dislocations, referred to as dynamic strain aging (DSA). Hence, PLC is one of the macroscopic manifestations of DSA in Al-Mg alloys. The microscopic mechanism leading to negative SRS is still a matter of debate.

Both PLC and DSA were extensively studied over the last several decades [e.g. McCormick1989, Picu2004, Kubin1990] with the goal being to achieve a better understanding of the small-scale processes and of the multiscale mechanisms that link the nanoscale DSA to the macroscale PLC effect. One technological goal of this present thesis is to increase the SRS parameter in the range of temperatures and strain rates relevant for industrial processes. If m would increase to positive values, this would insure material stability during processing and would eliminate PLC.

The grain size is expected to be important in defining the SRS in Al-Mg alloys. Grain refinement leads to a dramatic increase of the flow stress, as described by the Hall-Petch law

[Youssef2006]. The deformation mechanism in nanocrystalline materials changes too; dislocation activity becomes more difficult, while grain boundary sliding increases in relevance [Sanders1997].

Aluminum alloys have lower formability than conventional steels, which limits their use in the fabrication of complex auto body shapes. The limitation of formability of aluminum alloys processed by standard, symmetric rolling (SR) and annealing is associated with the development of cube texture that results from the formation of beta texture [Ma2004, Sakai2001, Kang2005]. Asymmetric rolling (ASR) introduces a shear texture and produces through-thickness uniform plastic strain. This provides promise that the method represents an economical way to alter the rolled microstructure of aluminum alloy sheet such to improve formability [Jin2004, Simões2008, Lee2008]. In ASR, the speeds of the two rolls at the contact surface with the workpiece are different and hence intense shear deformation throughout the entire sheet thickness is achieved. This differs from the type of shear deformation imposed by conventional (symmetric) rolling. Since the effective plastic strains reached by ASR are larger than those obtained with SR at same rolling reduction, ASR has been studied as a method to impart severe plastic deformation to the material.

Lee and co-workers [Lee2008, Choi1998, Kim1999, Kim2001] performed SR and ASR studies on Al sheet. They found that sheets with a shear texture containing a component of the <111> crystallographic direction parallel to the sheet normal (ND) have higher ductility [Lee2008]. The shear texture results through the thickness of the ASR processed samples, as opposed to the superficial effect produced by SR [Choi1998]. This requires either large reductions or the use of reversed ASR (ASRR). Reversing the ASR direction reverses the shear direction in each pass hence leading to a more symmetric shear texture [Kim2001].

Jin and Lloyd [Jin2005] performed SR and ASR on the 5000 class alloy AA5754 with reductions up to 56% (obtained in 2 passes). They observe that this level of rolling reduction does not introduce significant shear texture, but report than ASR is more efficient at producing grain refinement than SR. Larger rolling reductions, up to 91.3%, have been used in [Cui2000] and strong grain refinement ensues. Equiaxed grains as small as 2 μm which are retained upon annealing up to 200^{o}C result.

Recently, the effect of the rolling parameters on the development of shear texture components for improved formability of asymmetrically rolled and annealed 1050-O

aluminum alloy sheets was evaluated by Simões et al. [Simões2008]. The results indicate that ASR has the potential to become an important tool to achieve significant improvement in mechanical properties of aluminum alloys.

3.1.1.2 Microscopic mechanism

In sheet metal forming, the mobile dislocations have an intermittent motion and their density progressively increases with plastic deformation. When these dislocations get arrested at dislocation tangles, the segregated magnesium atoms from AA5182 diffuse by pipe diffusion and form atmospheres around the dislocations resulting in an effective blockage. With increasing applied force, the dislocations break away from the atmosphere and move freely towards the next tangles [Wen2005]. Repeating the pinning and unpinning process leads to negative SRS and thus to serrations in the stress-strain curve, as pointed out in figure 2.23 and 2.25 in the previous chapter.

A new mechanism, based on a mesoscopic analysis of the interaction of a mobile, un-clustered dislocation with a clustered forest has been proposed [Picu2004]. It is shown that the strength of dislocation junctions is strongly affected by the presence of clusters on forest dislocations. At a given plastic strain, the residence time of forests is a function of the strain rate. In other words, increasing the deformation rate reduces the aging time of forests, which leads to smaller clusters and lower dislocation junction strength, i.e. negative SRS. Hence, the undesired mechanical behavior of AA5182 exhibits a powerful correlation with its negative strain rate sensitivity, transforming this parameter into an important factor for its characterization [Vincze2007]. In view of this consideration, the investigation of AA5182 alloy sheet is based on exploring experimental strategies including severe plastic deformation that permit to analyze the factors that control the strain rate sensitivity parameter through grain refinement process.

Grain boundary sliding (GBS) may increase the strain rate sensitivity of the material and reducing the grain size should increase the probability of GBS. However, GBS alone is expected to lead to activation volumes much smaller than determined experimentally [Van Swygenhoven1998, Van Swygenhoven1999] and hence it can be concluded that the enhanced SRS in fine grained materials should be associated with the intense interaction of plasticity within the grains and the activity along grain boundaries. A refinement of these ideas is

proposed in [Qian2010] which reports results from ECAP processing of AA6063 indicating that the microstructure refines continuously with increasing the number of passes, which leads to a continuous increase of the yield and flow stress. However, the SRS remains almost unchanged during the first passes since grain refinement proceeds in this stage mostly through the formation of low angle grain boundaries. As the number of passes increases, high angle grain boundaries form, which leads to an increase of the SRS. This observation agrees with that in [Kammers2015] where direct observations of the deformation field at the microstructural scale were made using Digital Image correlation in pure Al deformed by ECAP. These indicate lower and higher SRS in regions with low and high angle grain boundaries, respectively.

Using thermo-mechanical treatments results in recovered and/or recrystallized microstructures which can be used to engineer microstructures and mechanical characteristics. For example, several studies [Ferry2005, Singh2013, Ding 2009, Tamimi2014] investigate the thermo-mechanical processing of aluminum alloys with the aim of developing fine-grained and nanostructured materials. Studies on fine grained materials have shown that yield strength increases via grain refinement. During these years, efforts were made to increase the yield strength on fine grained aluminum alloys [Lloyd1980, Jin2004]. This investigation will add to the picture that was given by different authors on processing AA5182 via asymmetric/symmetric rolling and annealing.

Based on these observations, it is expected that grain size engineering using a combination of rolling and heat treatments can be used to modify the effective SRS while maintaining favorable strength and ductility properties.

3.1.1.3 As received material

The commercial AA5182 alloy was supplied by ALCOA Company in the form of rolled and annealed sheet of 3 mm thickness. It is a primarily solid solution of Mg in Al, with the composition shown in table 3.

Table 3 *– Chemical composition of AA 5182 used in this study (wt%)*

Cr	Cu	Fe	Mg	Mn	Zn	Si	Ti	Al
0.006	0.038	0.258	**4.94**	0.334	0.011	0.244	0.013	Balance

3.1.2 TWIP Steels

3.1.2.1 Overview of the mechanical behaviour

Steel is one of the oldest developed materials and is still playing an important role in manufacturing today. For the automotive industry, steel is one of the materials of choice. Car weight is directly related to fuel consumption and hence to pollution and environmental degradation. However, the weight is also determined by consumer expectations with respect to safety, performance, passenger comfort and overall vehicle quality. This has led to a continuous decrease of the net weight over the past years. Reducing the weight without compromising vehicle performance has to involve the use of higher strength steels. The use of high strength steels with ultimate tensile strength (UTS) in the range 1300-1500 MPa would lead to weight savings of 30-40%. Recent designs tend to use "Dual Phase" (DP) and "Transformation-Induced Plasticity" (TRIP steels) with UTS above 1 GPa. A more promising material for energy absorption applications is the *Twinning Induced Plasticity (TWIP)* steel. TWIP steels are austenitic, i.e. have a face centered cubic structure at room temperature. Austenite is stabilized by the high concentration of Mn (in the 15-30wt% range). Under load, these material twin, but no phase transformation to martensite is observed. The carbon content is also rather high, (0.5-1wt%). Si is added to prevent C precipitation and formation of carbides. However, Si leads to galvanizability problems and can be replaced, in part, by Al.

The exceptional properties of this material emerge from the TWIP effect, i.e. the formation of deformation twins during plastic deformation. In the underformed state, the deformation-induced twinning is favored by the low stacking fault energy of the material which, in turn, is controlled by the addition of Mn. In order to achieve optimal properties, the stacking fault energy must be between 15 and 30 mJ/m^2. A lower SFE leads to the stress-

assisted transformation of the metastable gamma phase austenite to alpha and epsilon-martensite, i.e., the TRIP effect. Also a further increase in the SFE value leads to wavy slip because of the decreasing distance between partial dislocations. The large strength and ductility observed in TWIP steel are also due to the truly exceptional strain hardening induced by the TWIP effect which amounts to a close correlation between dislocation activity and twinning during deformation and the associated high stability of homogeneous plastic deformation [Barbier2009, Kocks1996, Li2015, Idrissi2010, Lebedkina2009, Venables1964, Bouazis2008]. Deformation twins act as strong obstacles to dislocation glide and the increasing number of these defects during straining results in a continuous reduction of the dislocation mean free path [Gutierrez-Urrutia2010, Allain2004, Jin2009]. Dynamic Hall-Petch effect is consider to be the responsible for the mechanism underlying the strain hardening behavior of TWIP steels [Bouaziz2001]. However, the large flow stress and large ductility of the material imply significant energy dissipation during deformation, which makes these alloys useful in applications requiring large energy absorption before failure. TWIP steels have exceptional energy absorption, approximately twice as large as that of TRIP steels. For example, when measured at a strain rate of 10^{-3} s^{-1}, a TWIP steel with 25% Mn and 3%Si, 3% Al absorbed more than 0.5 J/mm^3, compared with an average 0.3 J/mm^3 for DP steels [Frommeyer2003].

As in the case of Al-Mg alloys, one of the major problems with TWIP steels is related to their reduced or even negative SRS leading to an apparent Portevin-LeChatelier effect characterized by serrations in the stress-strain curve [Zavatieri2009]. In some ranges of temperature and strain rate, SRS renders the mechanical behavior sensitive to notches and small geometric and microstructural defects. This behavior has attracted some attention recently since non-uniform deformation reduces formability. However, in TWIP steels the physical process is not identical as in AA5182 because of the large strain hardening rate that this material presents.

By choosing this material, this work will help to understand the origin of strain rate sensitivity and eventually to increase it. This can be accomplished only after gaining a detailed understanding of the dislocation-twinning interactions leading to the pronounced strain hardening observed and to reduced strain rate sensitivity.

3.1.2.2 Microscopic mechanism

The dominant concept related to microscopic mechanism in TWIP steel is related to the classical mechanism for dynamic strain ageing (DSA) which requires a certain degree of coupling between the intermittent motion of dislocations and the evolution of mobile solute atoms [Cottrell and Bilby1949, McCormick1972, Mulford1979, Picu and Zhang2004, Picu2004]. Some studies have focused their attention on DSA being important in TWIP steels [Renard2010, Haijun2013]. Specifically, mobile dislocations, in their intermittent motion, get arrested at forest dislocations. During the arrest time, the solute diffuses along the core of mobile dislocations by pinning it. So, the longer the time that a mobile dislocation waits at an obstacle, the larger the stress required to put it back in motion. This leads to negative strain rate sensitivity.

Besides DSA, another time-dependent process of importance for TWIP steels is related to the twinning rate. Considering that twin growth and, to a smaller extent, twin nucleation require time, one expects that some level of rate dependence of the TWIP effect should be observed. If twin nucleation can be considered an Arrhenius process, one expects also a strain rate dependence of the critical stress at which twins form. In fact, Shen et al. has observed the strain rate sensitivity of the twinning rate in nano-twinned Cu [Shen2006], while Chun and his co-workers have made similar observations for a wrought Mg alloy [Chun2011].

The twins contain a high density of sessile dislocation segments, probably due to the intense interaction between themselves and the mobile dislocations producing plastic deformation of the austenite domains between twins [Idrissi2010$_a$, Idrissi2010$_b$]. Hence, increasing twin density leads to a reduction of the mean free path for dislocations and consequently an increase of the flow stress. On the other hand, twinning dislocations may move freely along twin interfaces, which leads to the increase of the twin thickness. The competition between these two effects, correlated with the low barrier for twin formation leads to the observed exceptional properties of these steels [Li2013].

A large effort has been made over the last decade to understand the physical basis of the TWIP microscopic mechanism behavior [e.g. Curtze2010, Chen2013]. Barbier et al. [Bartbier2009] characterized the twinning microstructure in fine-grained 22 Mn–0.6 C TWIP

steels by electron backscattering diffraction (EBSD) and found that as the texture strengthens with the deformation, a strong <111> orientation dependence of twinning is observed. TEM investigation of the twinning deformation mechanism indicates stair-rod cross-slip as a mechanism for twin nucleation, especially in presence of stacking faults distributed within the grains which could act as preferential sites for the operation of this mechanism [Idrissi2013].

3.1.2.3 As received material

FeMnCSiAl austenitic TWIP Steel with thickness of 1.85 mm is used in the present study as "as received" material. The tensile specimen was cut at 0^0, 45^0 and 90^0 from RD. The sheet was supplied by POSCO Mill (South Korea). Table 4 summarizes the general chemical composition of the alloy.

Table 4 *– Chemical composition of TWIP steel used in this study (wt%)*

C	Mn	Si	Al	Fe
0.6%	18%	0.22%	1.5%	balance

3.2 Correlation among mechanical and microstructural characteristics of Al-Mg alloys and TWIP steel

Scientists continually strive to find new materials that will change or improve life and advance current technologies. They find new ways of manipulating matter, getting smaller scales, inspired more and more from our way of living. The importance of such work is truly remarkable.

The main motivation behind choosing AA5182 and TWIP steel for this study is justified by the development of various industrial sectors, among which stands out the automobile industry. Furthermore, when it comes down to the comparison of these two different materials people often get left in the dark unable to decide which one to choose. Both metals have their own positive and negative characteristics that serve to their advantage and it is those small differences that lead to a final decision as to which one is to be used.

When a close comparison of these two materials is made, one finds that where one material has a weakness, the other has strength in that regard. Nevertheless, the preference

between these two metals remains mostly personal, because each has its own appeal and advantages. Making a comparative investigation, in the example below (figure 3.3), both steel (because its costs and properties) and aluminum (because of smaller specific weight) are used as hood material. Even though the source did not reveal the material grade, investigation shows significantly higher stiffness of the steel hood in comparison to the aluminum hood, but also significantly higher weight [Schwarz2004]. So far, many inconveniences are linked to these groups of materials. In addition to price and sheet metal forming matters, shape tolerances and stiffness need to be mentioned here. Common steels do not suffer from these problems, but their specific strength is not high enough to allow for light-weight design. However, to overcome these drawbacks a producer can focus their attention on combining/replacing the properties of different grades of steel (ex. TWIP Steels) and aluminum alloys (ex. AA5182) in an efficient symbiosis, to achieve outstanding mechanical properties. In this way, the competition between these two materials may be overcome.

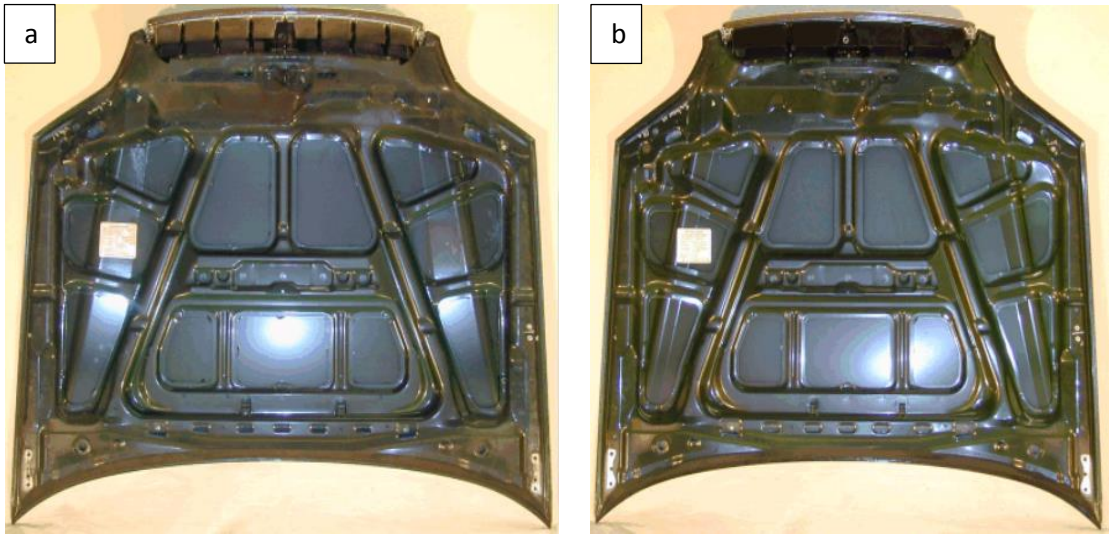

Figure 3.3 *- Actual series hoods made of a)steel (USA) and b)aluminum (Europe) with nearly the same design of inner hood structure [Schwarz2004].*

The comparison of experimental and theoretical results under deformation between TWIP steels and aluminum alloys has an important role in the choice of the material that would be better to a certain end [Miranda2008]. Thus, to eliminate any compromise between AA5182 and TWIP steels, instead of giving full interest to one of them, why not to focus all

the attention on both and try to correlate their properties. In this way, arises a great significance on the combination of interesting properties of these materials, allowing cost reductions and potential applications. In order to understand the tradeoff between aluminum magnesium alloy and TWIP steel, the level of agreement (common properties) between the two materials correlated within the motivation of the thesis has been analyzed and presented below.

- **Mechanical properties**

The strategy for choosing the materials in this investigation, takes into consideration the influence of the deformation routes on the two of the most promising engineering materials. Among them, TWIP steels and Al-Mg alloys have been extensively used in industries due to their excellent mechanical properties, light-weight and abundance. In section *3.1.1.1 and 3.1.1.2* these remarkable characteristics are summarized for each alloy.

- **Negative strain rate sensitivity**

The process of selection of the materials presented in this work is made taking into consideration an analysis of concrete undesired effects which appear in the industrial processing applications, namely negative strain rate sensitivity. The rate dependency of the mechanical behavior of metallic materials is a key factor in understanding the fundamental mechanism involved in the deformation process [Hadda2001].

AA5182 and TWIP steel exhibit negative strain rate sensitivity over a certain range of strain rates, i.e. higher flow stresses at lower strain rate. The negative strain rate sensitivity observed in Al-Mg alloys is a consequence of dynamic strain aging [Picu2005], whereas a combination of different processes causes this phenomenon to happen in TWIP Steels. More details about the influence of material strain-rate dependence on deformation behavior and microstructure can be found in section *2.2.2*.

- **Crystalline systems**

TWIP steels and Al-Mg alloys both have a face centred cubic crystalline structure - eight atoms at corners of the unit cell and one atom centred in each of the faces. In this sense, this couple of materials can be easily compared and correlated from the atomic point of view.

It is well known that the aluminium magnesium alloy crystallizes in the fcc with lattice constant of 4.05 Å. The crystalline microstructure consists of the intermetallic compounds, fcc β-Al_3Mg_2 equilibrium with the solid solution Mg in the aluminium matrix.

In the case of TWIP steels, Mn (15-30wt% range) increases the fcc lattice parameter and stabilizes the austenite, so that it can tolerate Al additions up to about 10 wt.% without becoming unstable, i.e. transforming into bcc-ferrite [Raabe2014]. Such an alloy design sustains many advantages, e.g. mechanical twinning and very high strain hardening.

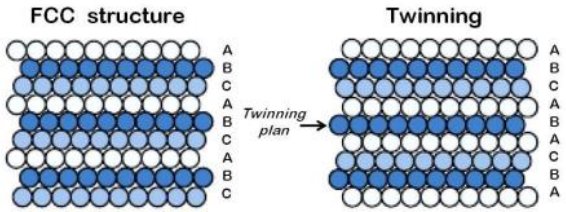

Figure 3.4 *- Perfect crystal FCC compared with a twinning deformation situation in the same crystalline structure [Gallot2011]*

- **Applications**

During the last decades there have been several advances in the production of steel and aluminum. The applications are the principal factor that help and govern which one of the two metals to choose, what grade of the chosen material to use or what combination of materials can constitute an efficient way to maximize the properties in different wide-range industrial applications. Understanding the basics behind the use for each of these materials will help to go a long way in terms of choosing the correct one for the service. Both materials have been in continuous use in the automotive industry for many years. While aluminum is the most abundantly available of the two metals for the light-weight design cars, the demand and scarcity of steel have caused immense interest for the same industrial sectors. Common steels do not suffer from these problems, but their specific strength is not high enough to allow for light-weight design [Niendorf2013]. Wohlecker et al. reported a series of body structures analysis that indicates aluminum mass reduction of 11 % to 34 % depending on whether it is compared to recent optimized steel designs or to former (non-optimized) steel designs [Wohlecker2009]. Consequently, this new group of steels that combine high strength

and formability – the high manganese austenitic twinning-induced plasticity (TWIP) steel show excellent promise for automotive applications.

- **Safety/Energy absorption**

Energy absorption is a key design parameter that depends on geometry, material strength and plasticity. Often factors that increase the strength of an alloy reduce its ductility, therefore the best energy absorbing alloys generally have an intermediate combination of both strength and ductility [Easton2006]. It is well known that the energy absorption capacity of Al-Mg alloys and TWIP steel promotes the enhancement of optimum mechanical properties. Both metals are now well established as structural materials (one with high SFE and other with low SFE), with major applications in BIW parts related to crash energy management (ex. longitudinal and side intrusion beams). TWIP steels have an advantage among other HSS/AHSS due to outstanding combination of plasticity and work hardening, hence elevate energy absorption capabilities. The composition concept of this material typically requires Si and Al additions to control the stacking fault energy [De Cooman2011].

The superior energy absorption properties of high-strength aluminum alloys (AA5182) and TWIP steels, matched with intelligent vehicle design, make aluminum and steel components for vehicles among the very safest on the road.

More and more vehicles on the road contain aluminum vs. steel parts and the relative crash worthiness of two like vehicles, will provide a safety advantage [Reisman2011]. Moreover, manufacturability and design issues associated with using steel and aluminum is under discussion.

- **Sustainability**

This section extends the analysis from other paragraphs, including new sustainability elements (manufacturability, functionality, recyclability/manufacturability) and it is aimed to developed a comparison during the entire life-cycle of the vehicle under two different material scenarios used in body-in-white structures for a typical vehicle. Figure 3.5 shows a comparison of BIW sustainability in steel and aluminum.

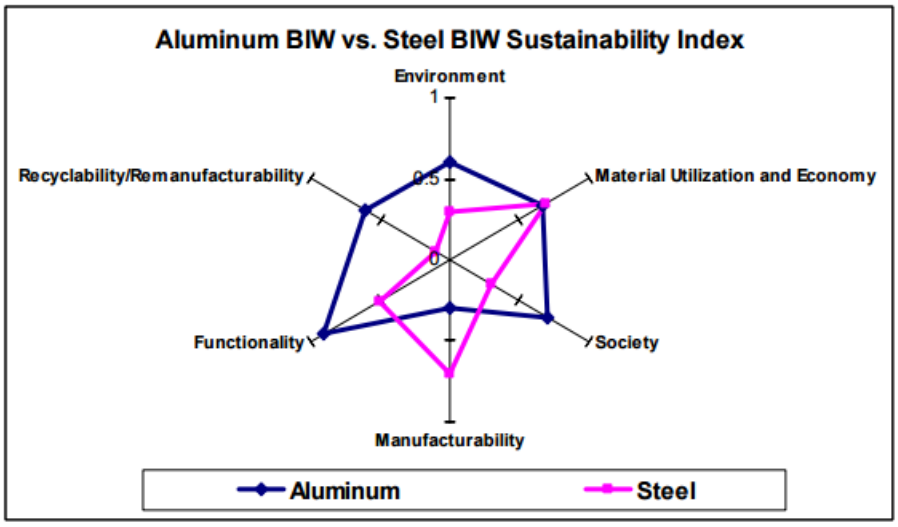

Figure 3.5 *- Aluminum and steel sustainability index comparison [Ungureanu2007]*

The overall index obtained by aluminum and steel can be easily compared and recommends these two materials as a potential future materials used in vehicle body applications.

- **Collaborative programs and projects**

The development of different collaborative programs and projects continually increased over the years, with the purpose of materials development for light weigh automobile design. Al-Mg alloy and TWIP steels are two of the candidates in the most world famous programs and projects related to BIW:

- *Experimental Composite Vehicle (ECV)* – oriented mostly for aluminum to improve fuel economy and general performance [Nicolaevich2014]:;
- *Ultra-Light Steel Auto Body* – with a huge impact over the 18 countries and concentrated more in light steel body vehicle, this program gain a colossal success between steel manufacturers [Nicolaevich2014];
- *Virtual Institute - Improving Performance and Productivity of Integral Structures through Fundamental Understanding of Metallurgical Reactions in Metallic Join* (2006) – the research topic of this program is the understanding of nonequilibrium metallurgical phenomena (i.e. precipitation, recrystallization and phase

transformation under high heating and high cooling rates) in metallic joints on lightweight materials, using in-situ synchrotron-based diffraction techniques. The following materials have been selected for this program: Al alloys (Aircraft): AlLi (2198), AlMgSc (8xxx) **Al alloys (Automotive): 6082, 5457**, Mg Alloys: AZ31 (wrought/rolled), **TWIP** and ODS steels [Dos Santos2006].

- *Super-Light-Car* – funded by Europe Commission, this program developed a multi material body in white concept for a running VW Golf V automobile (VW being the coordinator of the program), based on different lightweight materials like high-strength steel grades, magnesium and aluminum were the materials of choice. The multi-material concept is presented in fig 3.6. The final prototype concept reached a 34% weight reduction without losing performance while respecting the very demanding cost restrictions of such a popular model **[Superlightcar Project**2009].

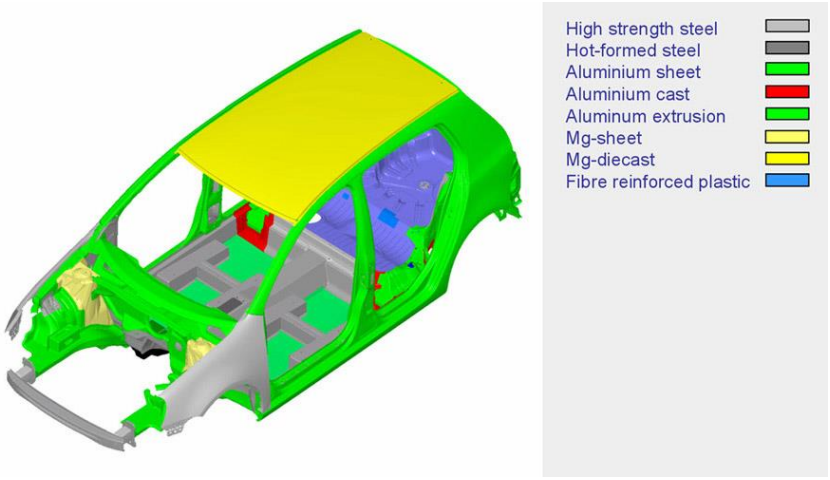

Figure 3.6 *- VW Golf V as a multi-material solution prototype [Superlightcar Project2009]*

- **Cost**

Cost and price are always an essential factor to consider when producing any finite industrial item. The price of steel and aluminum is continually fluctuating based on global supply and demand, fuel costs and the price and availability of iron and bauxite core. The cost of raw materials has a direct impact on the price of the finished product. It is generally well known that one product made from aluminum and other from steel, the aluminum part will almost always cost more because of the increase in the raw material price. Nowadays, the analysis of modern automobile designs shows some exceptions in the steel costs. In this category enter AHSS steels (TWIP steels) that has a considerable higher price than other common steels, because of their exceptional properties from a specific strengthening mechanism: twinning.

The fundamental criteria of material selection process had been discussed in this section. As a conclusion, by combining in materials design, the mechanical, chemical and thermal demands, improved, or possibly optimum, could be achieved. Therefore, aluminum magnesium alloy and TWIP steels will still continue to be the materials of choice for many years to come. However, further investigation is important after considering the factor of cost.

3.3 Experimental procedures

3.3.1 Mechanical tests

3.3.1.1 Uniaxial tensile test

The materials are tested in uniaxial tension using a Shimadzu Autograph Machine (Shimadzu, Japan) with maximum load capacity of 50 kN and the deformation was measured with a Messphysik ME46 video-extensometer (Austria). All the equipment is available at University of Aveiro and is shown in figure 3.7. From the load and displacement data, the true stress-true strain curves were established ($\sigma=f(\varepsilon)$).

***Figure 3.7** - Tensile Test Equipment used in this study: 1 - Shimadzu Autograph Machine, 2 — video extensometer.*

i. AA5182

For tensile testing, the material was cut along 0º from rolling direction and machined in a rectangular dog-bone shape with the following dimensions:

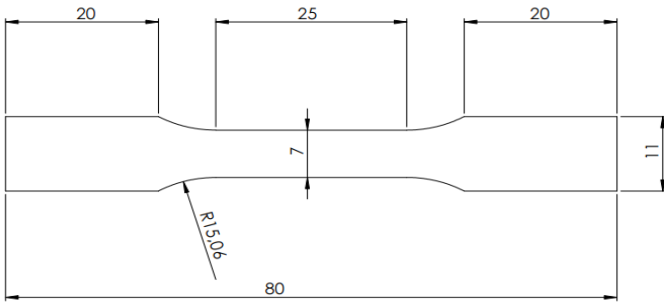

Figure 3.8 *– AA5182 specimen shape used for tensile test*

The material was tensile tested using the initial strain rate of 10^{-3} and $10^{-1}s^{-1}$in three conditions:

- as received
- after rolling
- after rolling and annealing

Strain rate sensitivity (SRS) calculation

To rationalize the effect of grain refinement on the strain rate sensitivity (SRS) parameter, $m = \partial log\sigma / \partial log\dot{\varepsilon}$ various authors [Asaro2005, Cahn2001] used the relation between *m* and the activation volume, V, V=kT/mσ, and assumed that V is a function of the length of the dislocation segment involved in an activation event.

For large grains, this length is determined by the density of forest dislocations, ρ, $V \sim \rho^{-1/2}$, while for nanograins, it is assumed to scale with the grain size, D, V~D. Further, the flow stress is written as a superposition of the effects of forest dislocations and finite grain size as $\sigma = A\sqrt{\rho} + BD^{-1/2}$. This leads to an expression for *m* which depends on both ρ and D. This analysis may indicate that m decreases or increases with plastic strain introduced by rolling (increase of ρ and decrease of D, function of the values of the parameters involved. Experiments on various Al alloys with grain of dimensions ranging from 100 μm to 100 nm [Wei2007, May2005, Miyamoto2006, Hoppel2005, VanSwygenhoven1999, Hayers2004] indicate that *m* increases with decreasing the grain size. This effect is highlighted in figure 4.8 from the next chapter.

ii. TWIP Steels

Tensile dog-bone shape samples of 1.85 mm thick are cut at 0°, 45° and 90° relative to the rolling direction of the metal sheet. The samples are subjected to tension with strain rates of 10^{-4}, 10^{-3}, 10^{-1} and $0.47s^{-1}$ in separate tests and strain rate jump tests. All tests are performed at room temperature.

Figure 3.9 *– TWIP steel specimens shape used for tensile test*

A series of interrupted tests at different percentages of deformation (10% and 20%) were performed to monitor the evolution of the microstructure.

Strain rate sensitivity (SRS) and strain hardening rate sensitivity (SHRS) calculation

The SRS and the SHRS are estimated from both monotonic stress-strain curves and from strain rate jump tests. In the strain rate jump tests the strain rate differential is 100, with a base rate of $10^{-3}s^{-1}$. When strain rate jump tests are performed, an instantaneous response is observed at the moment the strain rate is changed, followed by a transient. The instantaneous and transient SRS parameters were estimated as:

$$m^i = \left.\frac{\log(\sigma_i/\sigma_1)}{\log(\dot{\varepsilon}_2/\dot{\varepsilon}_1)}\right|_{\varepsilon} \quad \text{and} \quad m^t = \left.\frac{\log(\sigma_2/\sigma_i)}{\log(\dot{\varepsilon}_2/\dot{\varepsilon}_1)}\right|_{\varepsilon}, \tag{28}$$

where $\dot{\varepsilon}_1$ and $\dot{\varepsilon}_2$ are the strain rates before and after the jump, σ_1 is the stress at the moment of the jump and under strain rate $\dot{\varepsilon}_1$, σ_i is the stress after the instantaneous response following the change of the strain rate, and σ_2 is evaluated as the stress measured at the moment of the jump on the extension of the branch of the stress-strain curve corresponding to strain rate $\dot{\varepsilon}_2$ and

measured after the transient ends. The total strain rate sensitivity parameter, m, results as the sum of the instantaneous and transient parts, $m = m^t + m^i$ and hence

$$m = \frac{\log(\sigma_2/\sigma_1)}{\log(\dot{\varepsilon}_2/\dot{\varepsilon}_1)}\Big|_{\varepsilon} \tag{29}$$

When the SRS parameter is evaluated from constant strain rate tests, only the total *m* can be determined. In this case, the two values of the stress represent the flow stresses at the respective strain on the two stress-strain curves corresponding to the two strain rates.

The strain hardening rate is defined as $\theta = d\sigma/d\varepsilon$. The strain hardening rate varies with the strain rate. To characterize this effect, it is possible to evaluate the strain hardening rate sensitivity (SHRS) using a formula similar to eq. (29):

$$m_\theta^i = \frac{\log(\theta_i/\theta_1)}{\log(\dot{\varepsilon}_2/\dot{\varepsilon}_1)}\Big|_{\varepsilon} \quad \text{and} \quad m_\theta^t = \frac{\log(\theta_2/\theta_i)}{\log(\dot{\varepsilon}_2/\dot{\varepsilon}_1)}\Big|_{\varepsilon}, \tag{30}$$

and, the total SHRS is similarly evaluated as $m_\theta = m_\theta^i + m_\theta^t$ [Bintu2015].

3.3.1.2 Asymmetric/Symmetric rolling

One of the most efficient technique of controlling grain size is through severe plastic deformation (SPD) and annealing. Nevertheless modern techniques of grain refinement like equal channel angular extrusion process (ECAE) [Ivahashi1997, Chen2003, Li2013$_a$] or High Pressure Torsion [Xu2008], are available and successfully applied for Al-Mg system alloy, their application to large dimension structural materials is believed to be troublesome. However, rolling still remains the most suitable, cheap and convenient deformation process for the fabrication of large scale structural materials.

A rectangular slab of AA5182 initial material was cold symmetric rolled (SR) and reverse and continuous asymmetric rolled (ASRC/ASRR) in four degrees of deformation: 25%, 50%, 66% and 90%. The four reduction were obtained in 1, 2, 4, and 6 passes, respectively, with 32%±2% reduction per pass. The processes were carried out to reduce the thickness of the specimens from 3 mm to 2.75, 1.5, 1, and 0.3 mm. The reasons for such an

experiments are based on grain refinement approach in aluminium magnesium alloys for properties improvement.

The machine (figure 3.11) has identical upper and lower cylinders with a diameter of 180 mm, powered with independent DC electrical motors. The rotation speed and direction of each working-roll are controlled by a computer software. Symmetric (SR) and asymmetric rolling processes were carried out using 15-15 rot/min and 15-11 rot/min, respectively, for upper and lower rolls. Rolling was performed without lubrication.

The dimensional change produced by ASR is being performed either continuously (ASRC) or by reversing the direction of the in-plane shear at each pass (ASRR). The samples were rotated 180^0 around RD after each pass, like in the figure 3.10 below.

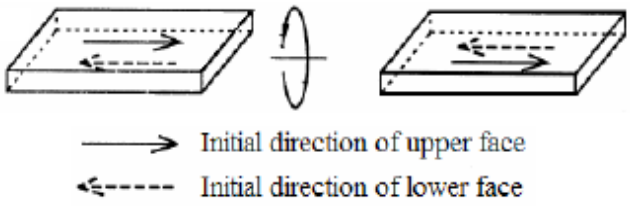

Figure 3.10– *Reverse asymmetric rolling illustration*

Figure 3.11 *- Asymmetric rolling machine available at University of Aveiro.*

3.3.1.3 Heat treatment

The aim of this intermediate investigation was to choose the best route of temperatures and times over which recrystallization may not occur for different levels of deformation in Al-Mg alloys.

Annealing is performed at the end of the rolling process. According to the previous results of processing AA5182, the temperature is set at 195ºC and four annealing times are considered namely 30, 60, 90 and 120 mins. The designation of the 4 heat treatments applied to each rolled sample in an electrical furnace are:

- HT1=195º/30min
- HT2=195º/60min
- HT3=195º/90min
- HT4=195º/120min

The annealing temperature is below the solvus line of the phase diagram of the Al-Mg system (figure 3.12), while the times are selected such to avoid considerable recovery and grain growth.

According to Golovin et al. recrystallization of cold worked binary Al–Mg alloys with 0.3–5%Mg takes place in the temperature range 270–300 °C related to the decrease in hardness [Golovin2013]. They present this behavior, supported by microstructural studies, in figure 3.13.

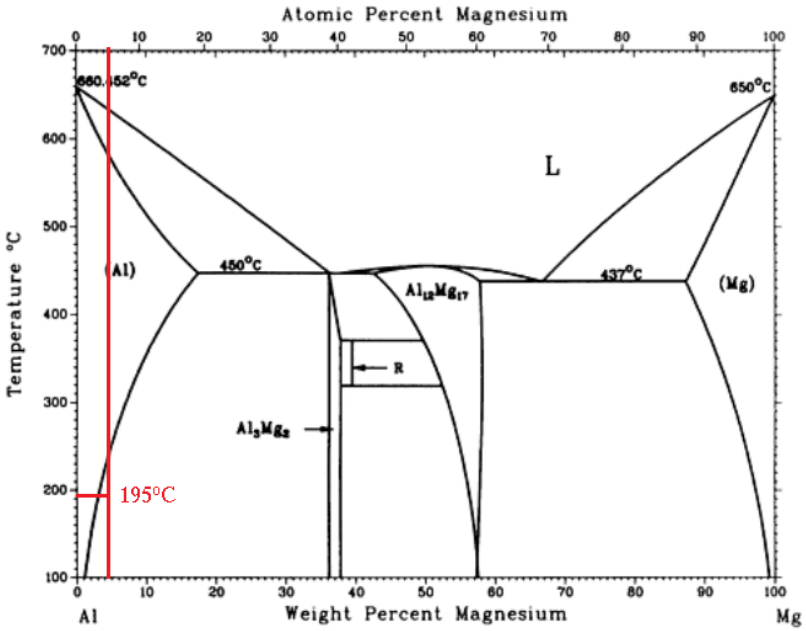

***Figure 3.12**- Al-Mg alloy equilibrium phase diagram [www3]*

This above diagram corresponds to the unprocessed material system. Strongly deformed material may exhibit small variations of the critical temperatures in the diagram.

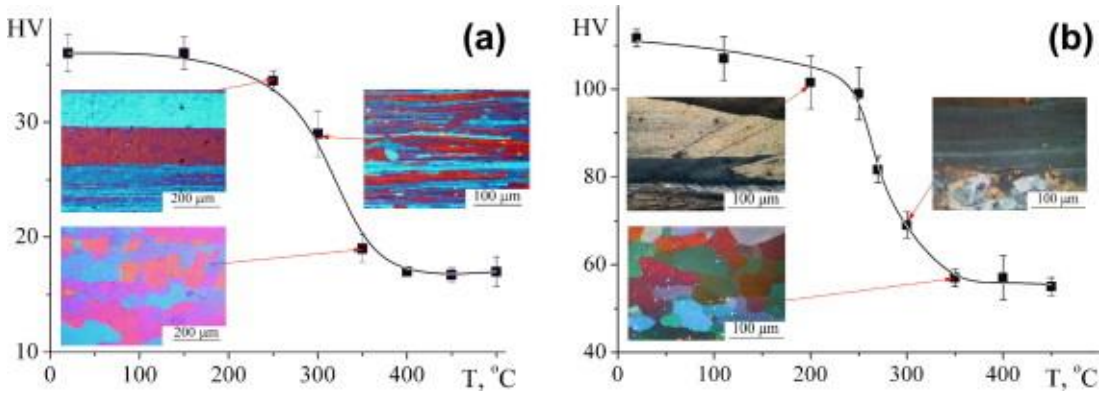

***Figure 3.13** - Hardness versus annealing temperature (annealing time 30 min) curves for cold rolled Al–0.3 Mg (CR 80%) (a) and Al–5Mg (CR 70%) (b) alloys. Insets: microstructures after annealing at corresponding temperatures [Golovin2013].*

3.3.1.4 Hardness tests

It is well known that hardness is a mechanical property that is often used for comparison between different materials and techniques. The hardness is either determined from the total test force to the penetration depth or the indentation area. Common static indentation tests including Rockwell, Vickers, and nano-indentation were performed in this thesis with the aim of reveal as much information as possible about the hardening mechanisms observable in TWIP steels.

Vickers hardness measurements were carried out on samples deformed up to 20% strain using a Shimadzu 2000-Vickers Instrument. A force of 4.9 N was applied for a duration of 10 s. Rockwell hardness (HRC) was also measured on same TWIP steel samples using a Karl Frank GMBH Frankoskop 38180 hardness tester.

3.3.2 Microstructural characterization

The goal of microstructural characterization is to define the microstructure evolution and resulting properties of the materials, connecting the different processing paths with grain refinement in Al-Mg alloy and twinning evolution in TWIP steels. This section will present the microscopy techniques used in the present work as well as metallographic preparation of samples

3.3.2.1 TEM / HR-TEM

The observations of the microstructural features is performed with a JEOL 2200FS High-Resolution Energy-Filtered Transmission Electron Microscope (HR-EF-TEM) operating with an accelerating voltage of 200 kV and equipped with a Schottky emission (SE) electron gun and an Omega type energy filter (figure 3.14). Electron microscopy was also performed with a Hitachi H-9000 (300 kV) transmission electron microscope (TEM).

Figure 3.14 *- JEOL 2200FS High-Resolution Energy-Filtered Transmission Electron Microscope available at University of Aveiro.*

AA5182 and TWIP steel foils cut parallel to the rolling plane are taken at the sheet mid-thickness location. The microstructural characterization was carried out after classical metallographic sample preparation which included mechanical grinding and polishing up to 6 μm diamond suspension, then electropolished using:

- double-jet thinner with a dilute solution of HNO_3 and methanol under 10-15 V tension at 20^{o}C for Al-Mg alloys.
- 5% perchloric acid in 95% acetic acid at 30V, 0.5A at room temperature (water running cooling system) for TWIP steel.

The samples were placed in ethanol immediately after grinding/electropolishing and ultrasonically cleaned.

3.3.2.2 SEM / EBSD

Scanning electron microscopy (SEM) equipped with Electron Backscatter Diffraction (EBSD) system (figure 3.15) is also used to characterize the samples.

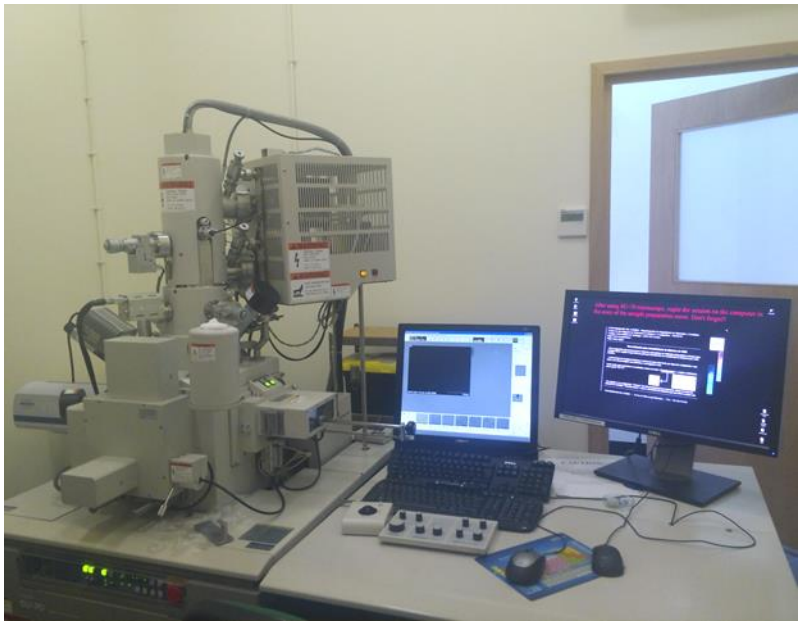

***Figure 3.15** - Hitachi SU70 - Scanning Electron Microscope available at University of Aveiro*

A HR-FESEM Hitachi SU70 equipment operating at 20 kV and endowed with a Quantax Cryst Align EBSD system from Bruker is used. A step size of 60 nm is employed to acquire the EBSD orientation maps and Kikuchi pattern quality (KPQ) maps from a large population of grains. This powerful technique was very useful to define the crystallographic orientations of TWIP Steel grains after nanoindentation. Considering AA5182, surface characterization by SEM was enough to reveal the grain refinement and existing precipitates.

For the observation, the surface of the specimen to be analyzed is first standard grinded followed by electrolytic polishing using a Struers A2 electrolyte. The process is carried out in a Struers LectroPol-5 automatic electrolytic polishing and etching equipment operated at 35 V for TWIP steels and 15V for Al-Mg alloys. After finishing the electrolytic procedure, the sample is immediately removed and cleaned with ethanol in an ultrasonic cleaner. To acquire high quality patterns for EBSD measurements, the specimens were placed in the sample holder inside SEM chamber at an angle of 70° relative to the electron beam (see

figure 3.16) in order to reduce the path of backscattered electrons and to decrease the fraction of absorbed electrons.

More information about the details of the EBSD measurements are given in the table 7:

Table 7 *– Example of settings for EBSD measurements*

Map size (area depends on working distance)	500x 375
EBSP map size	400x300
Exposure time	50ms
Required number of indexed band	7 or 5
Maximum BMM	2
Voltage	20kV

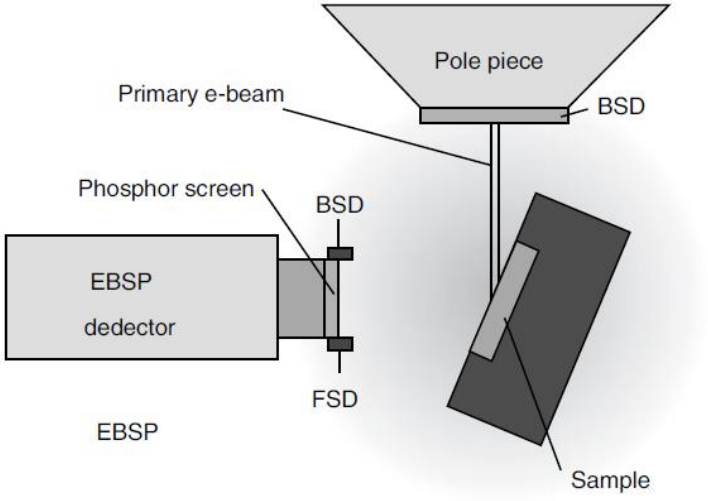

Figure 3.16*- Orientation of the specimen surface inside SEM specimen chamber* ***[****Maitland2007]*.

3.3.2.3 AFM

To gain a deep understanding of the twinning mechanisms that take place in TWIP steels, related microstructures and local material properties several AFM measurements were undertaken in contact mode with a Surface Imaging Systems (S.I.S.) from CSM Instruments. The equipment/technique was useful to find and select the proper grains aria prior and after nano indentation. All the AFM images and plots were processed with Gwyddion and Indentation 4.04 Softwares.

3.3.2.4 Nanoindentation

Nano-indentation tests were performed using a three-sided pyramidal Berkovich diamond indenter having a nominal tip radius of 20 nm, attached to a nano-indenter (TTX-NHT, CSM Instruments) and working in load control mode. Multiple arrays of 20 × 20 indents spaced 4μm apart were performed by applying a maximum force of 7mN. Some tests were performed with higher indentation loads, as specified below. Calibration of the indentation apparatus was carried out prior to each set of tests to ensure the indents fall exactly on the selected zone.

In order to examine the twin nucleation process the force of the indenter was varied from 50 mN to 100mN and 150mN.

To check whether deformation twins in TWIP steel are strain-rate sensitive under the indenter, the speed of the indentation was changed. In this case, 2, 20 and 200 mN/min were the selected rates. The hardness and elastic modulus were obtained from the curves using the Oliver–Pharr method.

The TWIP Steel specimens for Atomic Force Microscopy (AFM) observations were electro-polished as described above, to obtain clean surfaces after mechanical polishing. The examinations were made for the samples cutted parallel to the rolling direction and at the tensile strain of 20%, deformed with two extreme strain rates ($10^{-4}s^{-1}$ and 0.47 s^{-1}). A differentiation between two possible twin mechanisms in TWIP Steel is attempted. For this case, were chosen two extreme deformation rate cases, to observe the difference between twin density and mechanical properties.

The AFM plus Nano Indentation instrument is shown in the figure 3.17 below.

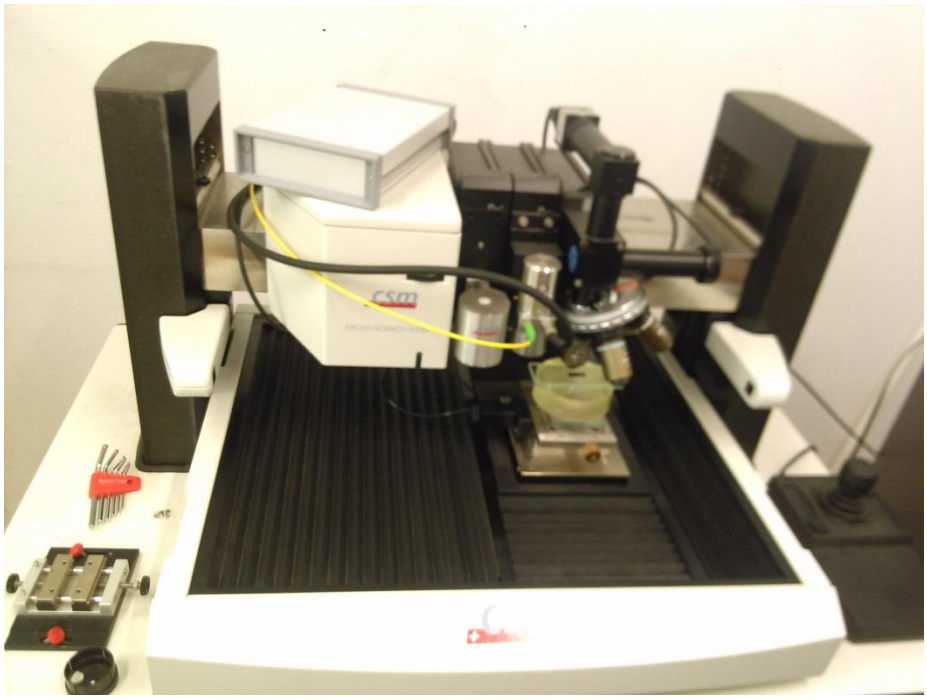

Figure 3.17 *– Atomic Force Microscopy and Nano Indenter system (0.1-500mN) available at University of Aveiro*

3.3.2.5 Flow chart

In the figure 3.18 it is presented the flow chart depicting the processing steps involved in mechanical testing and microstructure characterization of AA5182 and TWIP steels.

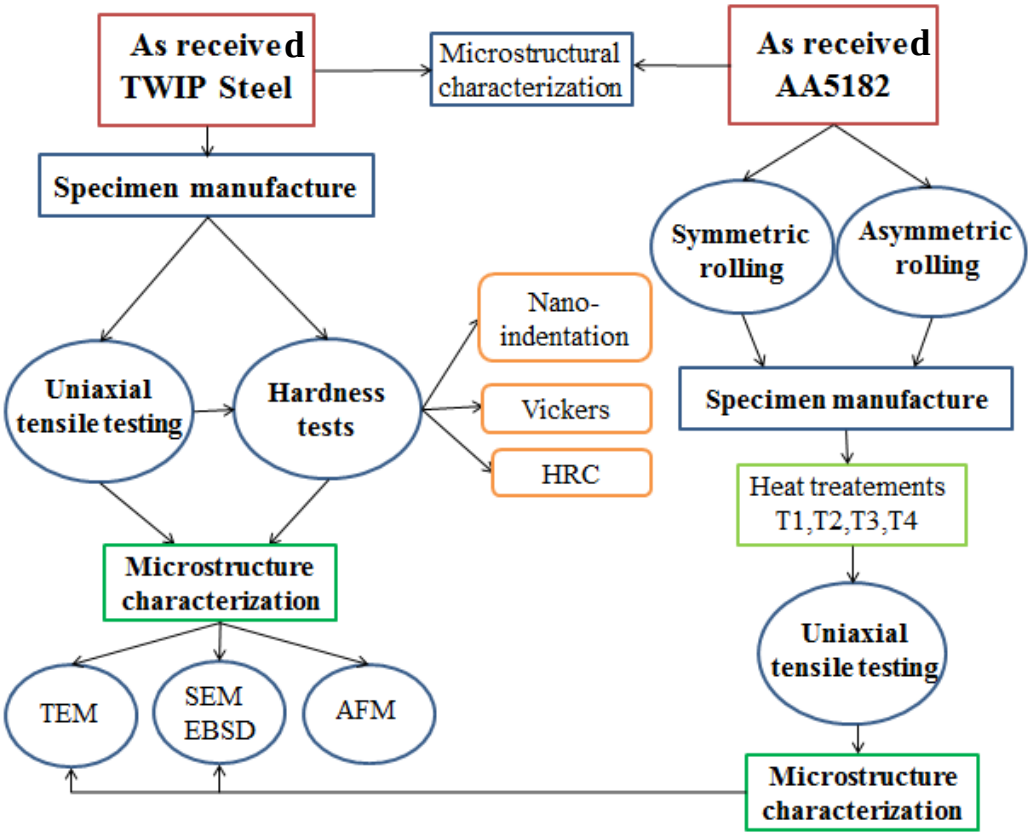

Figure 3.18 *- Flowchart of experimental work performed reported in this thesis for AA5182 and TWIP steel.*

CHAPTER 4

Thermo-mechanical investigation of strain rate sensitivity of AA5182

CHAPTER 4 – Thermo-mechanical investigation of strain rate sensitivity of AA5182

In the present chapter, it is presented the mechanical behavior and the underlying deformation microstructure after tensile testing and annealing of grain refined AA5182 specimens processed by symmetric and asymmetric rolling. A clear understanding of the material response under different deformation routes is crucial for this material future applications as a high-strength lightweight alloy. Thus, additional investigations are needed and this chapter will take care to enlighten and explore any haziness connected to the objectives of the thesis. To accomplish the objectives of this section, four test series corresponding to rolling reduction of 25%, 50%, 66% and 90% were undertaken and the tensile response of the deformed-grained sheet was investigated. Three rolling techniques are compared – conventional symmetric rolling, continuous and reversed asymmetric rolling – and the subsequent heat treatment is performed at 195^{o}C for times ranging from 30 to 120 mins.

Based on these observations, the possible approaches to improve the formability of aluminum-magnesium alloys are put forward. It is also interesting to determine whether the SRS may be rendered positive through such processing.

4.1 Mechanical behaviour after different rolling schedules and heat treatment

4.1.1 Influence of rolling reduction on the tensile flow curves

Figure 4.1 shows the true stress-true strain curves of samples deformed by ASRR to various degrees and subjected to the HT1 heat treatment following rolling. The curve corresponding to the initial material and that corresponding to the material rolled to 90% reduction and not heat treated are also included for reference. The expected behavior is observed: the flow stress increases and the ductility decreases with the rolling reduction. The shape of the curves changes too, but for reductions larger than 50% the strain hardening rate remains unchanged. The evolution of the key parameters obtained from these curves, i.e. the

yield stress, strain at failure and the ultimate tensile strength, with the rolling reduction is shown in Fig. 4.1(b).

Similar trends result when the material is processed using SR and ASRC. For given heat treatment, the stress-strain curves of samples processed by SR, ASRC and ASRR overlap, provided that the rolling reductions is smaller than 90%. Similarly, the stress strain curves obtained with samples rolled under the same conditions but annealed differently (HT1 to HT4) overlap, provided the rolling reduction is smaller than 90%. Some difference are observed for 90% reduction, as discussed below.

A similar advance in the mechanical behavior of the severely cold worked and annealed Al-Mg has been observed elsewhere in the literature [Radović2008, Taye2014].

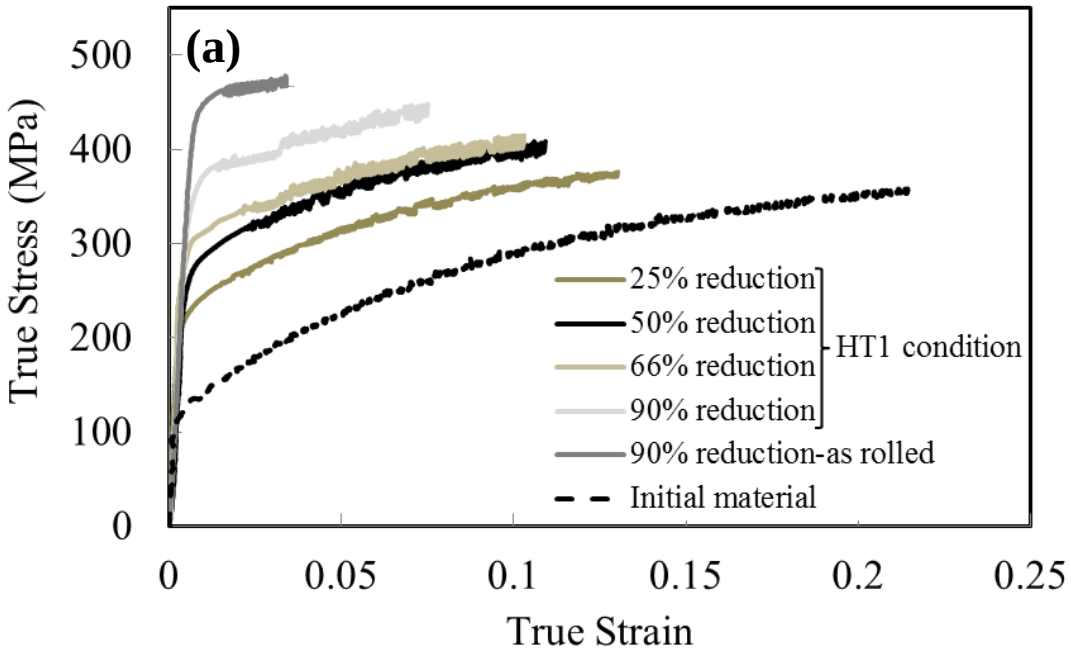

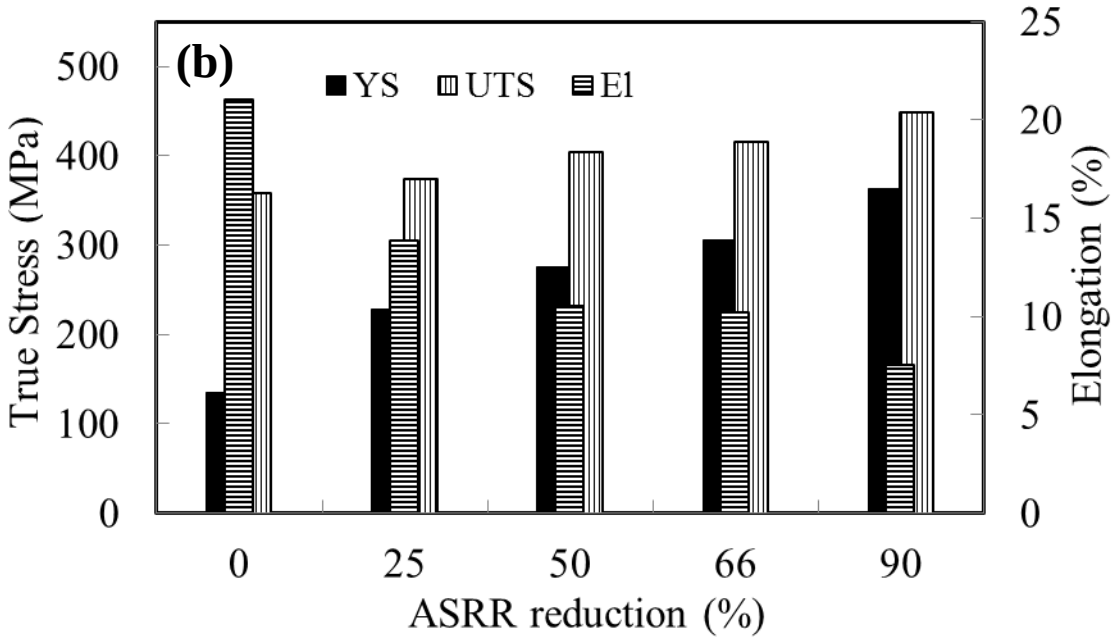

Figure 4.1 *– a) True Stress-True Strain curves of AA5182 subjected to reverse asymmetric rolling deformation (ASRR) up to 25%, 50%, 66%, 90% and annealing at 195°C/30 min (T1 regime). The curves are compared with the initial material and 90% as-rolled material; b) summarized mechanical properties, namely yield strength (YS), elongation (El) and ultimate tensile strength (UTS) corresponded to a). The curves were obtained with a strain rate of* $10^{-3}s^{-1}$

4.1.2 PLC interval

Nowadays, the study of the PLC effect has drawn continuing interest since it is a fascinating example of complex spatio-temporal dynamics arising from the collective behavior of various defects within the metallic alloy system. In microscopic sense, the physical origin of the PLC effect is associated with dynamic strain ageing (DSA) due to the interaction of gliding dislocations and diffusing solute atoms [Rizzi2004, Jiang2007, Chatterjee 2010]. The influence of rolling reduction and critical strain over the PLC interval will be highlighted in this section.

All stress-strain curves are serrated, which indicates that the PLC effect is not eliminated by rolling. A considerable decrease of the PLC interval with increasing rolling

reduction is observed. For the experiments considered here, the morphology of the serrations shows similar overall behavior - type *B* (hop through the specimen discontinuously) for the present strain rate ($10^{-3}s^{-1}$) in all the reduction. As reported by Abbadi et al., type A serrations are associated with normal behavior of the PLC interval, type C with inverse behavior, and type B marks the intermediate transition region called "plateau" [Abbadi2002]. It corresponds to the intermittent propagation of a localization band along the gauge of the specimen. Outside of these plateaus the serrations are random. This was observed in several specimens only and could not be related to particular microstructural or geometrical features of the specimens.

The serration amplitude is also largely independent of the rolling method used or the heat treatment applied if the amplitude is measured at the same strain differential relative to the critical strain for the onset of serrated flow, ε_c. Interestingly, the critical strain ε_c varies with the rolling reduction as shown in Fig. 4.2. As indicated above, this function is independent of the rolling method and type of heat treatment applied.

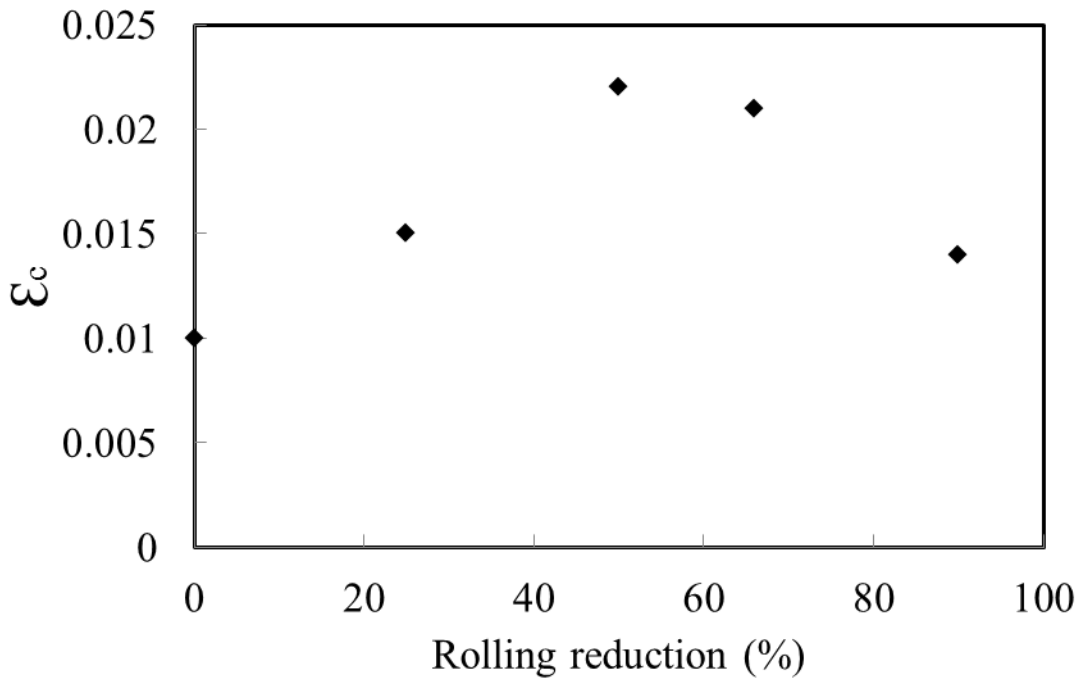

Figure 4.2 *- Critical strain for the onset of the PLC effect as a function of ASRR rolling reduction and for the HT1 condition.*

Feng et al. investigate the PLC band nucleation in AA5754 [Feng2012]. They report that the first band in a specimen is initiated at a critical strain which increases with the applied strain rate corresponding to the reduction in aging time solely due to an increase in critical strain.

Recently the Portevin–Le Chatelier effect was clearly observed in the work of Krishna et al. and similar behavior with the present case was reported - with smaller grain size (larger rolling reductions) and an increasing dislocation density, the critical strain for the onset of the PLC effect was lowered [Krishna2015].

4.1.3 Strain rate sensitivity parameter

The unstable plastic flow above described is basically traced back to a negative strain rate sensitivity (SRS) of the flow stress, namely a decrease of the flow stress with increasing applied strain rate. This assumes that the theoretical and experimental investigations on SRS should consider the rolling reduction factor and the annealing treatment. Each of this assumption will be discussed.

Influence of rolling reductions and annealing treatment on SRS

The observation of PLC in all samples, including those subjected to the largest rolling reduction, indicates that the SRS parameter, m, is negative. The value of m was evaluated from constant strain rate tests for all conditions. Figure 4.3 shows *m* computed at 5% true strain for all rolling methods used and for two heat treatments, HT1 and HT4 (check *3.3.1.3* for elucidation).

It results that *m* is independent of the rolling reduction, rolling method and type of heat treatment applied as long as the reduction is smaller than 50%. At larger reduction, m increases towards zero, but remains negative even for 90% reduction. The rate at which m increases depends slightly on the rolling method used. Specifically, the effect is more pronounced when asymmetric rolling is applied, and this seems to correlate with the fact that ASR produces larger equivalent plastic strains in the sample.

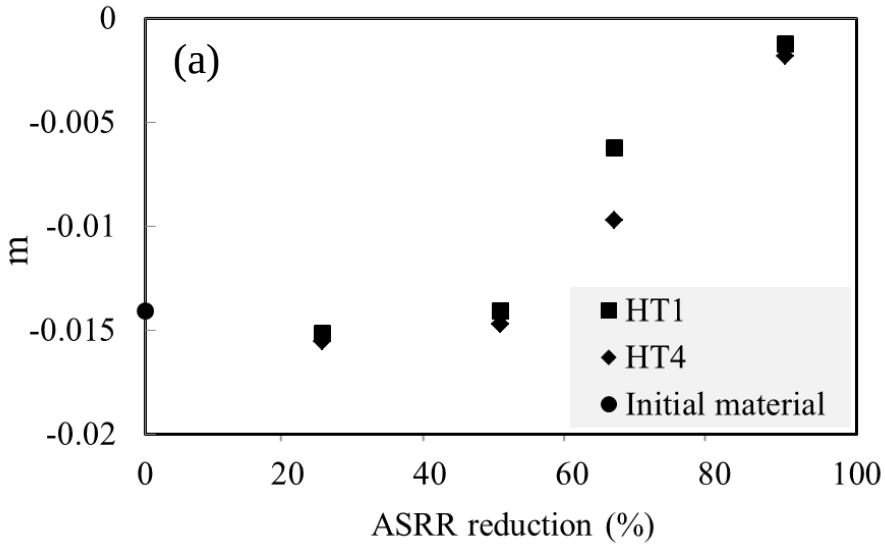
(a)
0
-0.005
-0.01
-0.015
-0.02
m
0
20
40
60
80
100
ASRR reduction (%)
HT1
HT4
Initial material

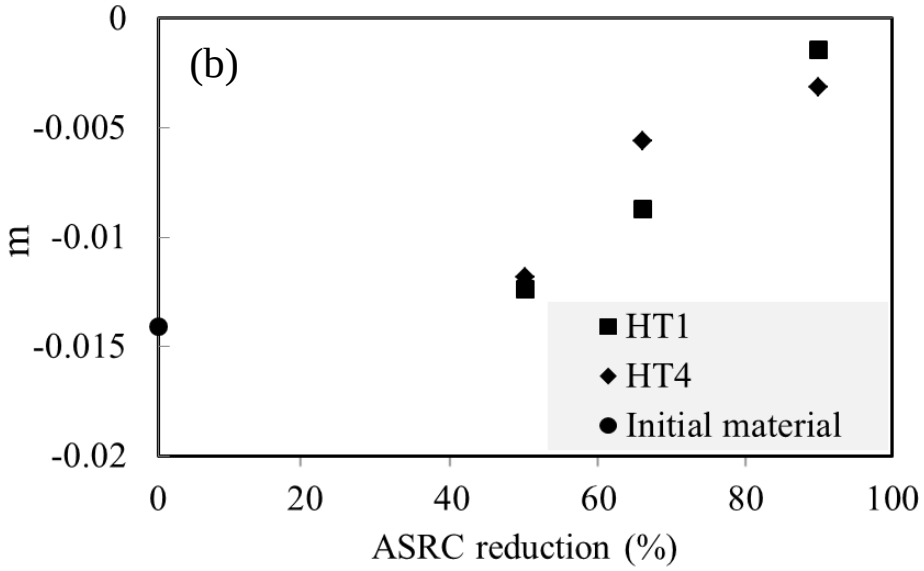
(b)
0
-0.005
-0.01
-0.015
-0.02
m
0
20
40
60
80
100
ASRC reduction (%)
HT1
HT4
Initial material

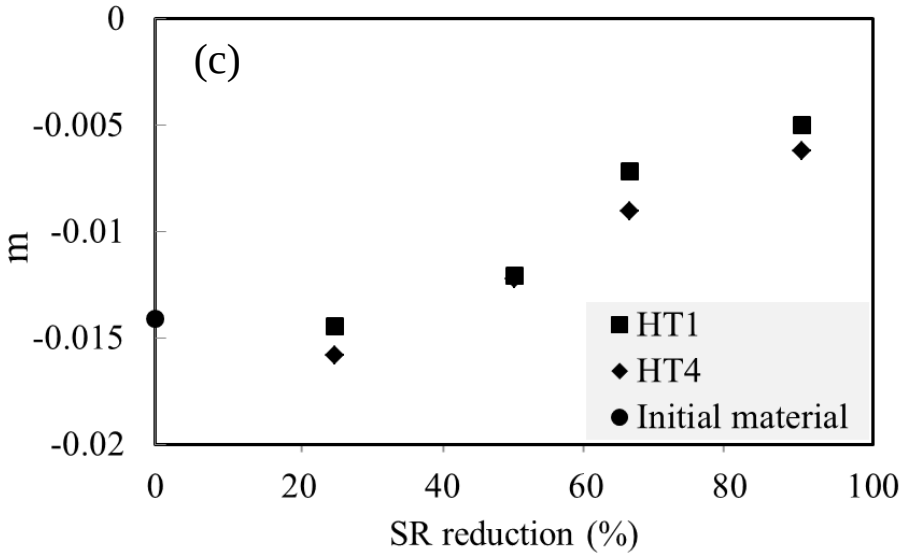

Figure 4.3 *- Strain rate sensitivity parameter (calculated at 5% strain) as a function of a) ASRR b) ASRC and c) SR rolling reductions. Data for two heat treatments (HT1 and HT4) is shown.*

The transition between negative to a less negative strain rate sensitivity values in different Al alloy was studied by several authors [Han2006, Khan2012, Karibian2014]. The conventional belief is based on the activation of DSA at certain temperatures and strains. Considering that DSA effect is triggered by the migration of the Mg solute atoms in the Al matrix, different amounts of Mg content would alter this effect. Hence, the negative SRS domain is not identical in different processed Al-Mg sample with different concentrations of Mg [Kabirian2014]. Curtin et al. and Soare et al. attribute the negative values of the SRS to a series of concurrent nano-scale phenomena, namely solute strengthening and dislocation forest aging while the first contribute to the reduction of SRS from positive values to almost zero, the hardening followed by dislocation forest aging decrease the coefficient to negative values [Curtin2006, Soare2008]. However, information about the variability of the sensitivity parameter with different rolling reduction and annealing for AA5182 are rare in the literature.

Rolling and grain boundary sliding may increase SRS due to two reasons: accumulation of dislocations (in a pure metal, with no solute content, *m* increases continuously with strain due to the accumulation of dislocations), or to the variation of cluster sizes. Plastic deformation homogenizes the structure, while annealing allows for

heterogeneity to form (either as solute clusters or as precipitates). Another mechanism that contribute to the increase of m with increasing deformation is the formation of high angle grain boundaries (HAGB) below explained.

4.1.4 Heat treatment effect

In an attempt to explore the outcome of symmetric and asymmetric rolling, one should consider also the annealing behavior of produced alloys after subjected to different heat treatments. The high density of defects, in this case grain boundaries and dislocations, accumulated in the material to increase the strength, increase the susceptibility to recovery, recrystallization and grain growth [Bazarnik2012]. On the other hand, in alloys containing solid solution, as this case, it may be expected that depending on the deformation temperature, time, mode, strain and thermodynamic characteristics of the alloy, the changing in solute percentages may influence the mechanical properties of the final sheet [Hutchinson2009].

The effect of heat treatment on the mechanical behaviour of samples processed with different rolling techniques requires further discussion. As mentioned above, as long as the rolling reduction is smaller than 90%, the heat treatment applied has no effect on the stress-strain curve of the resulting material. An example is provided in Fig. 4.4 that shows the true stress-true strain curves of samples processed by ASRR to 50% reduction, and subjected to the HT1 and HT4 heat treatments respectively. The two curves overlap. The similar curves obtained from samples processed by ASRC and SR up to 50% reduction (not shown) also overlap to those shown in Fig. 4.4. Differences are observed for samples subjected to 90% reduction. For these, the heat treatment and the rolling method applied make a difference.

To quantify this effect, Fig. 4.5 shows the variation of the yield stress with the annealing time (HT1 to HT4) for the three rolling methods and for samples with 90% reduction. The yield stress decreases with increasing the annealing time for SR, while for ASRR and ASRC it increases. This behaviour is surprising and indicates that different microstructures result at this large rolling reduction by using different techniques. The reduction of the yield stress with increasing annealing time observed for SR samples is similar to what is expected for the non-rolled material. The ASR samples exhibit an increase of the yield stress of up to 30 MPa (about 10%) as the post-rolling annealing time increases. The strain hardening rate is not affected much by the type of rolling and heat treatment.

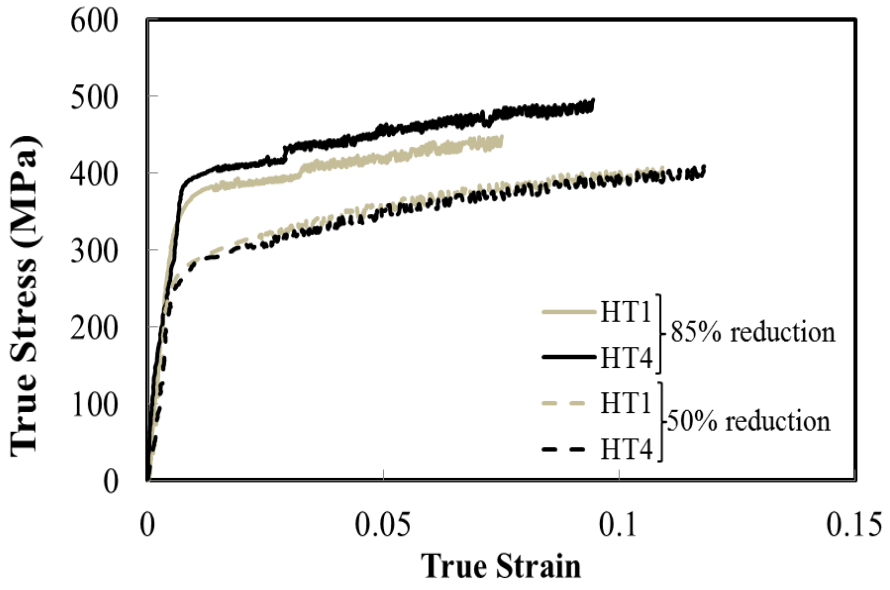

Figure 4.4 *- True stress-true strain curves of the 50% and 90% ASRR-deformed samples. Curves from samples processed by HT1 and HT4 are shown. All curves result from tests performed with a strain rate of 10^{-3} s^{-1}.*

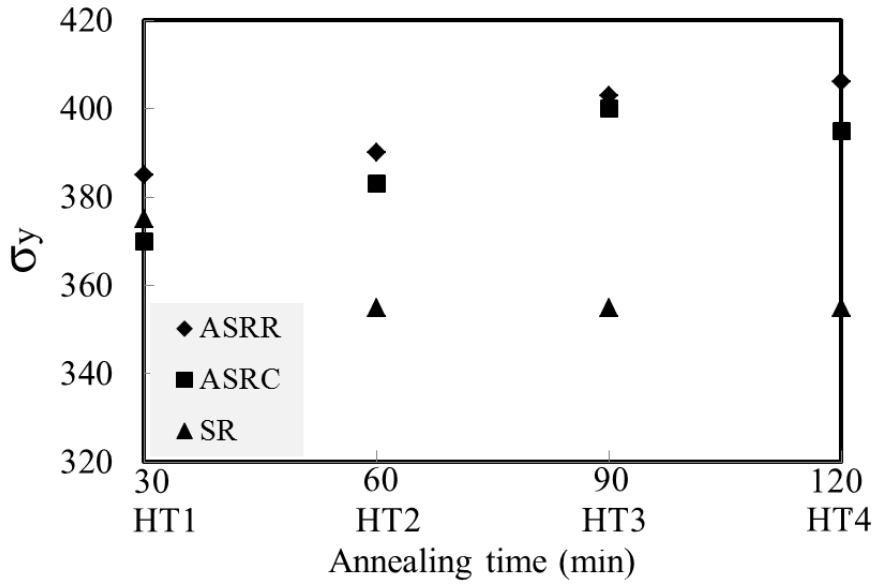

Figure 4.5 *- The effect of the applied heat treatment on the yield stress for the three rolling methods considered. All samples were rolled to 90% reduction and the subsequent mechanical test was performed with a strain rate of 10^{-3} s^{-1}.*

4.2 Microstructure evolution after cold rolling and annealing

4.2.1 Grain size refining

The microstructure of rolled and annealed samples has been studied using electron backscatter diffraction (EBSD) and electron microscopy (TEM). Figure 4.6 shows EBSD misorientation average images (EBSD-MO) for (a) as-received, (b) 25% SR, c) 25% ASRR and d) 50% SR samples. The microstructure of samples rolled to higher reductions cannot be probed with the same technique due to the high degree of defectiveness of the respective lattice. In fact, Fig. 4.6 (d) already shows significant damage of the microstructure. Samples subjected to 90% reduction have been investigated using STEM and TEM.

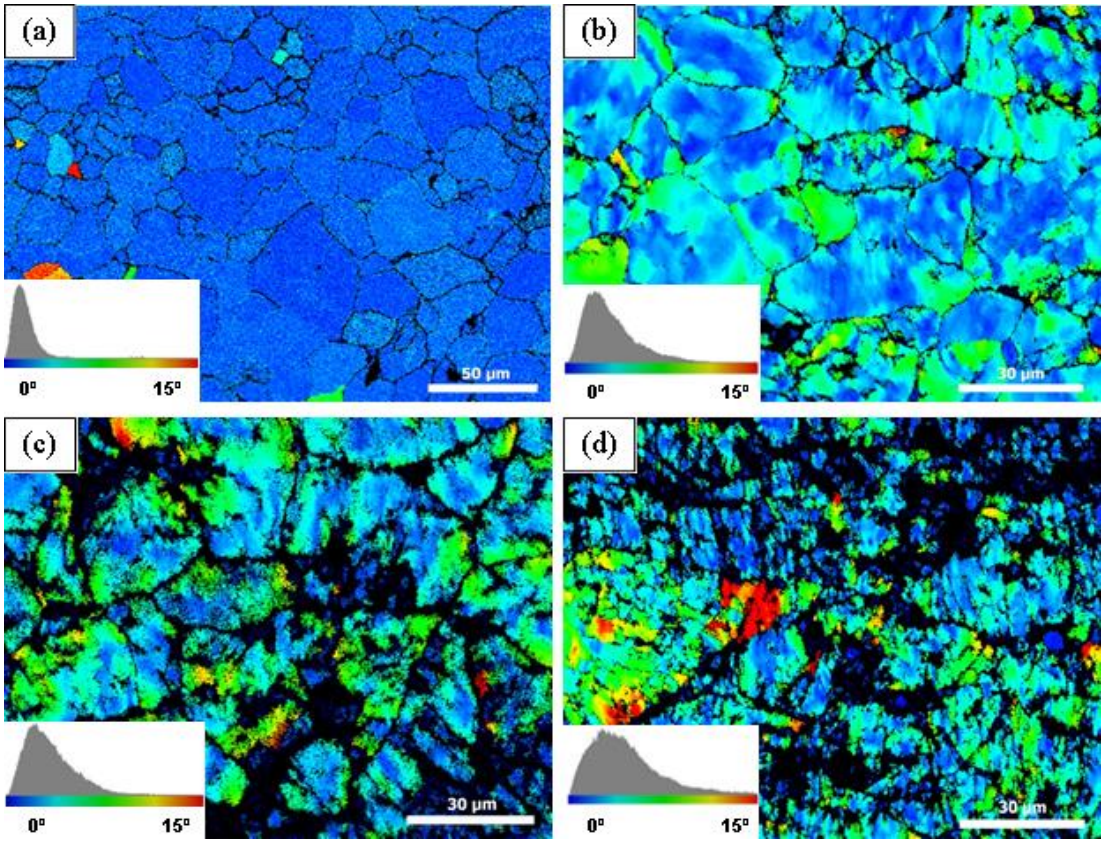

Figure 4.6 *– EBSD misorientation averages micrographs for a) as-received, b) SR with reduction 25%, c) ASRR with reduction 25%, d) SR with reduction 50% samples, followed by annealing in the HT4 condition (Note the change of grain size and shape, and dislocation density in the grain interiors after deformation). The insets show the color code corresponded to the degree of missorientation angles between the grains. The rolling axis is along the horizontal direction of the micrographs.*

The grain size was determined from the EBSD maps for samples rolled up to 50% reduction and based on TEM images for samples rolled with a reduction of 90%. The as-received material has a rather homogeneous microstructure with equiaxed grains of averarge size 33 μm. Rolling using SR or ASR up to 25% reduction does not change significantly the grain size, while samples rolled to 50% reduction have a slightly smaller average grain size, of 20 μm. STEM and TEM images of the microstructure of samples rolled to 90% reduction and HT1 and HT4 treated (Fig. 4.7) indicate an average grain size of 0.3 μm, independent of the heat treatment. These grains are not elongated in the rolling direction and, despite their small size, contain a large number of dislocations. The corresponded diffraction patterns located at the left bottom corner of TEM micrographs gives evidences, by the intensity and place of the diffraction spots, of grains rotation and formation of new nano-grains inside the parent grain. Grain refinement by conventional and asymmetric rolling in 6000 class Al alloys was also reported in several references [Kang2005, Kim2001] and it was observed that ASR is more efficient at producing fine grains uniformly through the thickness of the sheet. Similar studies were undertaken over the years and have demonstrated significant strengthening of aluminum alloys achieved through grain size refinement [Youssef2006, Tuan2015, Yu2015].

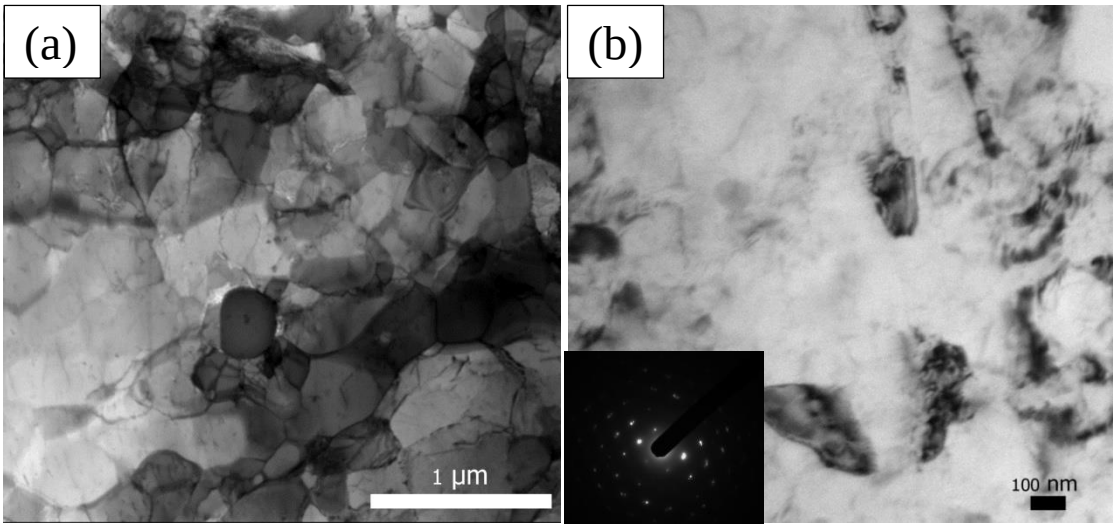

Figure 4.7 *– STEM micrograph showing the microstructure of AA5182 at 90% reduction obtained by ASRR followed by HT4; b) BF-TEM micrograph showing the microstructure of AA5182 at 90% reduction obtained by ASRR followed by HT4. In the inset it's shown the selected area diffraction pattern of TEM micrograph.*

It is useful to place the current findings in the context of the literature regarding the dependence of the strain rate sensitivity of Al alloys on the grain size. Figure 4.8 shows results corresponding to Al alloys of several types adapted from Ref. [Wei2007]. Parameter *m* increases as the grain size decreases and is positive for all cases reported. We add the present data set (Fig. 4.3) to the figure using the grain size estimates reported above. The trend as well as the rate of increase of *m* with decreasing grain size are similar to those of the other alloys. However, this comparison should be made with care. The SRS is controlled primarily by factors that are only marginally related to the grain size such as the distribution of solute and the activation energy for unlocking dislocations arrested at precipitates or within dislocation structures. The various materials used to produce the data in Fig. 4.8 have different precipitation states and have been processed in different conditions. This may explain the rather large scatter observed in Fig. 4.8.

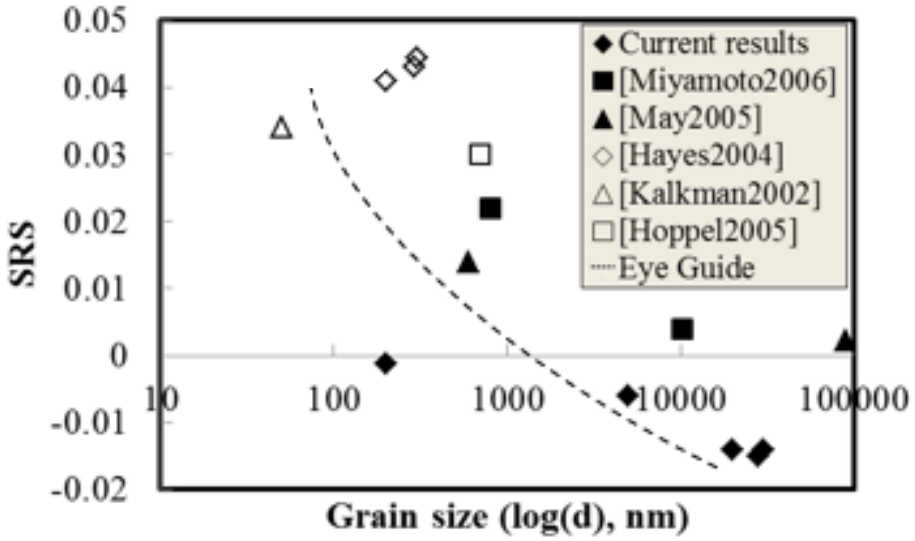

Figure 4.8 *– Strain rate sensitivity parameter versus the grain size for AA5182 (present data - filled diamonds) and several other Al alloys (adapted from [Wei2007]).*

4.2.2 Grain boundaries evolution

Additional information can be obtained from the EBSD-MO maps shown in Fig. 4.6. The as-received images show no sub-grain structures, which is expected for the annealed state. As the rolling reduction increases, the degree of grain sub-structuring increases. The insets in the four maps of Fig. 4.6 indicate the color coding as well as the distribution of intra-

granular misorientation angles. With a threshold separating low angle (LAGB) from high angle grain boundaries (HAGB) of 15º [Cui2000], it results that a rolling reduction of 25% is already introducing a significant fraction of LAGB and this fraction increases as the reduction increases. TEM observations of samples rolled to 90% reduction indicate the dominant presence of HAGB. Both the direct TEM observations and the associated diffraction patterns confirm the existence of nanoscale grains in these samples. Therefore, the LAGB produced in the initial stages of rolling evolve into HAGB, as also reported in [Qian2010] for AA6063 processed by ECAP.

The central result of this work is the observation that rolling, and in particular ASRR, to reductions above 50% leads to a monotonic increase of the SRS parameter even in alloys exhibiting $m < 0$. The exact mechanism leading to this effect cannot be identified based on the present observations. However, two candidate mechanisms can be outlined. One of these is based on the concept suggested in Refs. [Kammers2015 and Qian2010]. These authors indicate that the interaction of dislocations with HAGB increases the SRS parameter. Here we observe that severe plastic deformation introduces LAGB at small equivalent plastic strains and HABG at higher plastic strains. While this mechanism may operate in AA5182, it is also possible that additional physics is important. The negative SRS of Al-Mg alloys is due to the presence of Mg in solid solution. If deformation reduces the concentration of Mg atoms free to diffuse, it is likely that *m* increases. Since plastic deformation drastically increases the density of dislocations and other interfaces that may getter Mg, it is possible to envision that the effective concentration of Mg in solid solution decreases with increasing equivalent plastic strain. The effective plastic strain introduced by ASR is larger than that produced by SR for given rolling reduction and hence the effect of ASR on *m* is expected to be more pronounced than that due to SR; this is observed in Fig. 4.3.

4.2.3 Heat treatment effect

The unusual effect of the heat treatment reported in Fig. 4.5 indicates that multiple mechanisms are play. Picu at al. [Picu2006, Xu2007] observed that formation of solute clusters in AA5182 leads to a reduction of m (i.e. m becomes more negative). Samples of the same material were annealed in the solid solution domain, quenched and tested immediately,

while other samples from the same batch were annealed in the same conditions, quenched, kept at room temperature for 24h and then tested. The values of m for the first type of samples was negative, but closer to zero than for the second type of samples. This annealing was too short to produce any significant changes of the dislocation density, which was also confirmed by the fact that the flow stress did not change upon treatment. In the present case, no Mg precipitates were observed by TEM in the as-received state (which is compatible with the characterization of the manufacturer), but solute may form clusters. Plastic deformation leads to the partial dissolution of such clusters (not residing at dislocation cores or interfaces) which is expected to lead to an increase of m, as seen in Fig. 4.3. Subsequent annealing should favor the reformation of these clusters. The effect of this process on the yield stress depends on the relative contribution to strengthening of free solute and clustered/precipitated solute. It should also be noted that texture is generally considered to have a weak effect on m [Nicolau1997]. The different rolling methods used in this study lead to different textures and clearly, the rolling reduction determines the degree of texturing. The effect reported here is not expected to be directly controlled by the type of texture in our samples.

4.3 Partial conclusions

In this study we explore the possibility of using asymmetric rolling to increase the strain rate sensitivity of AA5182 which exhibits negative SRS and the PLC effect at room temperature. We observe that increasing the rolling reduction up to 50% leads to a significant increase of the yield and flow stress and a reduction of the ductility, but leaves the SRS parameter *m* unchanged. Larger reductions lead to an increase of m. At 90% reduction, m remains negative, but is close to zero. Further increase of the flow stress is observed as the rolling reduction increases from 50% to 90%, while the stain hardening rate remains unchanged. ASR is more effective in producing these effects, and ASRR is superior to ASRC from this point of view. The type of heat treatment applied after rolling is inconsequential for the mechanical behavior as long as the rolling reduction is smaller than 90%. At the largest reduction, increasing the post-rolling annealing time reduces and increases the yield stress for SR and ASR rolled samples, respectively, while the effect on *m* is small. Several mechanisms which may lead to the observed increase of m upon rolling are discussed.

CHAPTER 5

Investigation of the origin of the negative strain rate sensitivity parameter of TWIP steel

CHAPTER 5 - Investigation of the origin of the negative strain rate sensitivity parameter of TWIP steel

In this Chapter it is demonstrated for an austenitic TWIP steel with 18% Mn a strong dependence of the twinning rate on the strain rate, which results in negative strain hardening rate sensitivity (SHRS). The instantaneous component of SHRS is large and negative, while its transient is close to zero. The SRS is observed to decrease with strain, becoming negative for larger strains. Direct observations of the strain rate dependence of the twinning rate are made using electron microscopy and electron backscatter diffraction, which substantiate the proposed mechanism for the observed negative SHRS.

*5.*1 Mechanical behavior

5.1.1 Tensile flow curves

When comparing the stress-strain curves obtained from monotonic uniaxial testing at different strain rates some differences of the flow stress can be easily observable. Figure 5.1 a) shows the true stress-true strain response for samples cut in the rolling direction (0^o) tested at 10^{-1} and 10^{-3} s^{-1}. The remarkable strength and ductility of this TWIP steel is immediately obvious. The ultimate tensile strength (UTS) is in the range 1.3-1.4 GPa and the elongation at failure is approximately 0.4 true strain. This behavior is common to all TWIP steels and is due to the large and almost strain-independent strain hardening rate, which helps stabilize the deformation. Jerky flow characterized by serrations in the stress-strain curves, sometimes observed in TWIP steels, is not seen in our samples in this range of strain rates and temperatures.

A significant difference between the two curves is observed beyond approximately 0.15 strain. The strain rate sensitivity of the yield stress is very small, but the strain hardening rate is strongly dependent on the strain rate. This leads to more than 100 MPa difference in UTS between the two curves. Hence, exceptional failure stress and strain can be reached only upon reducing the strain rate to low enough values. This also implies promoting homogeneous plastic deformation.

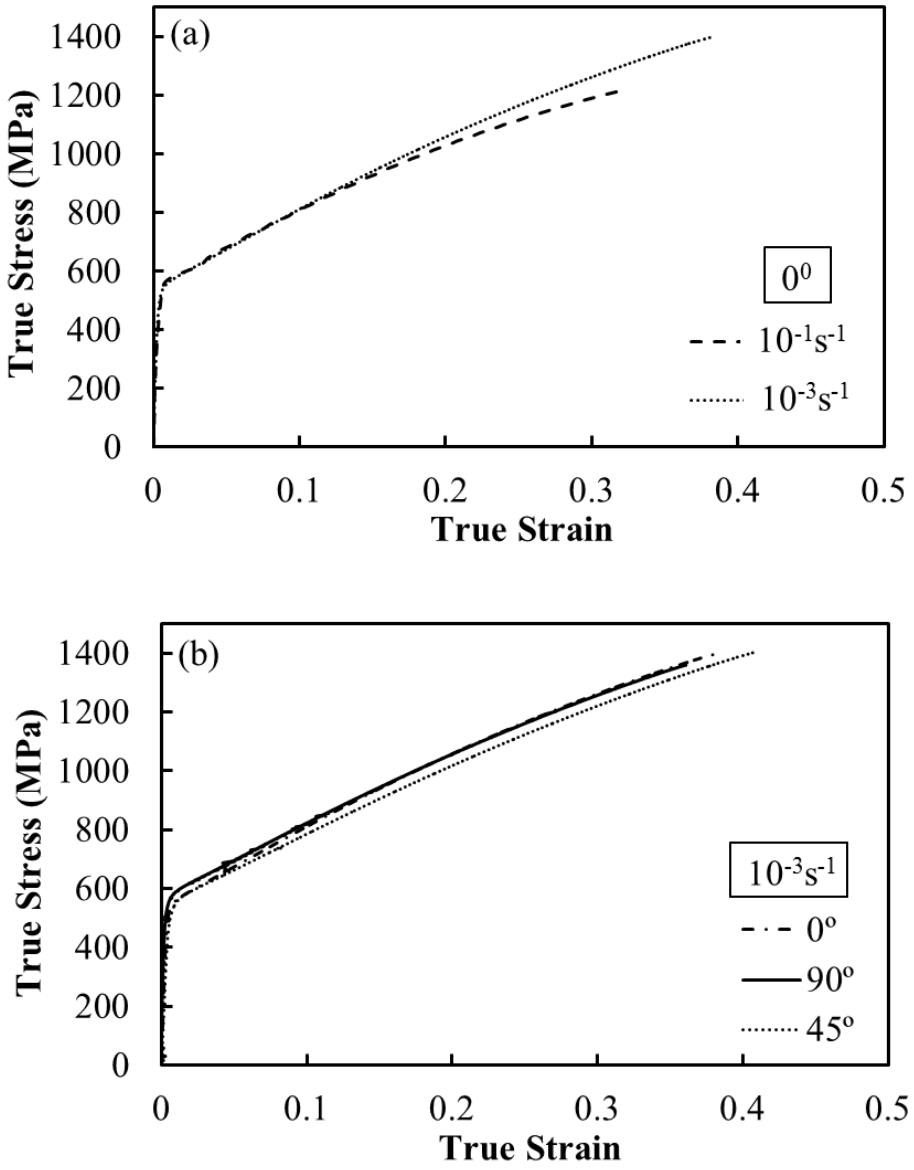

Figure 5.1 *- True strain-true stress curves for a) samples cut parallel to the rolling direction and deformed at 10^{-3} and 10^{-1} s^{-1}, and b) samples cut parallel, perpendicular and at 45^{0} to the rolling direction and deformed at 10^{-3} s^{-1}.*

Figure 5.1 b) shows the stress-strain response for samples cut parallel, perpendicular and at 45º to the rolling direction and deformed at 10^{-3} s^{-1}. The 90º sample has a higher flow stress, but approximately the same strain hardening rate with the 45º sample. The curves are essentially parallel, with a difference of ~ 20MPa between them. The sample cut parallel to the rolling direction exhibits a higher strain hardening rate.

5.1.2 Strain hardening rate sensitivity response

To quantify the dependence of the strain hardening rate on the strain rate, figure 5.2 a) shows the total SHRS parameter evaluated with eq. 30. Figure 5.2 b) shows the strain hardening rate computed from the monotonic curves of figure 5.1 a). θ decreases fast up to about 0.01 true strain and then decreases much more gradually up to failure. The curve corresponding to the sample deformed at 10^{-1} s^{-1} falls below the lower strain rate curve once the strain becomes larger than 0.05. The slope of the $\theta(\varepsilon)$ curves in the second regime, above ~0.01 strain, is almost constant suggesting sustained twinning throughout the deformation history. The slope is higher for the sample deformed faster. This indicates that the nature of the twinning process is not affected by $\dot{\varepsilon}$, but the rate of twinning depends strongly on the strain rate.

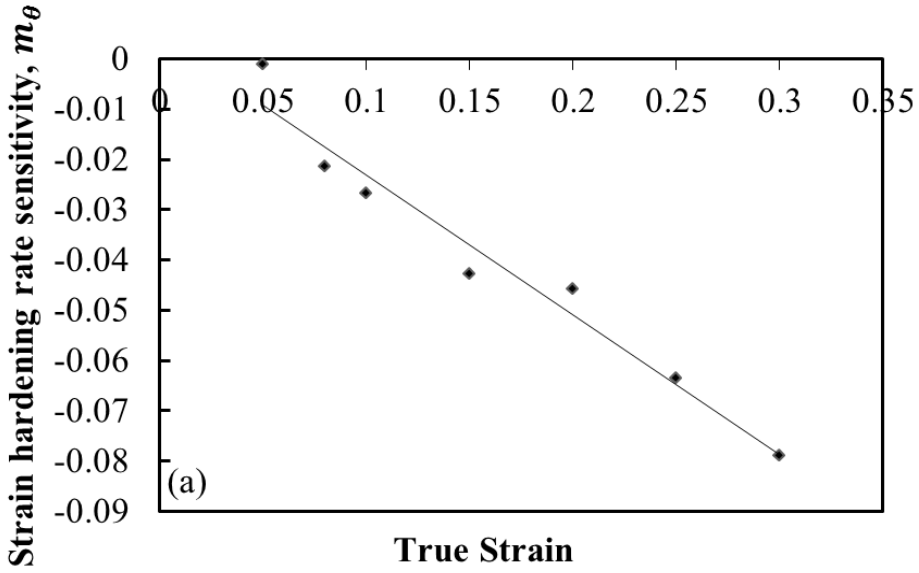

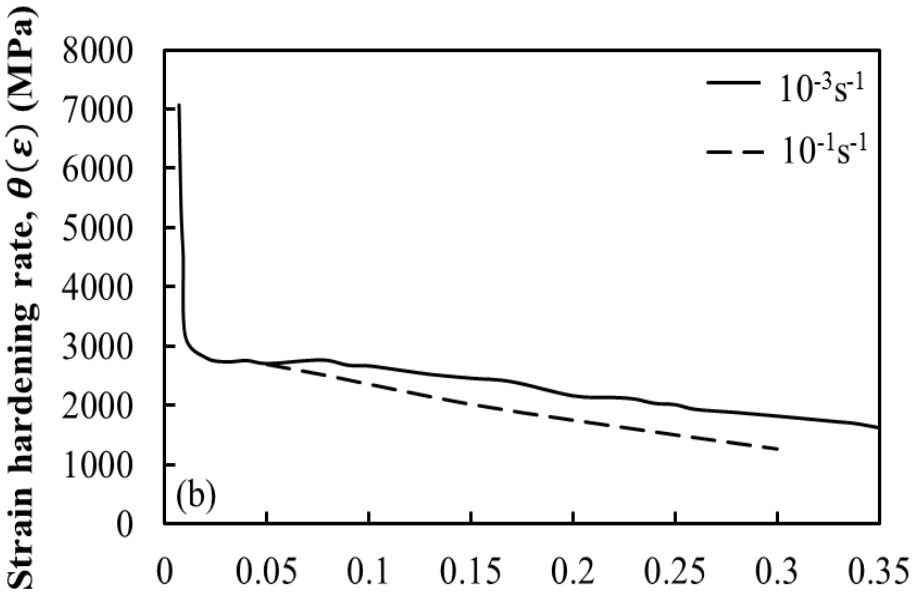

Figure 5.2 *- a) Total SHRS parameter m_θ vs. strain. b) Strain hardening rate, $\theta(\varepsilon)$, vs. strain for samples deformed at 10^{-1} and 10^{-3} s^{-1}.*

Figure 5.2 a) indicates that m_θ is always negative and decreases almost linearly with strain, reaching large negative values. It is further possible to evaluate m_θ^i and m_θ^t from strain rate jump tests. This allows observing that the transient component is essentially zero and the total m_θ reported in figure 5.2 equals the instantaneous component. This is made clear below, part of the discussion of the SRS. Let us turn now to the evaluation of the SRS parameter, *m*, based on strain rate jump experiments. Both strain rate jumps up, from 10^{-3} s^{-1}, with a differential of 100, and strain rate jumps down, from 10^{-1} s^{-1}, with the same differential are performed at various strains. Figure 5.3 a) shows the monotonic curves corresponding to the two strain rates (labeled $\dot{\varepsilon} = 10^{-3}s^{-1}$ and $\dot{\varepsilon} = 10^{-1}s^{-1}$, respectively) and curves from tests in which strain rate jumps up are performed at several strains. Figure 5.3 b) shows a detail of figure 5.3 a) in which only the monotonic curves along with two curves corresponding to jumps performed at 0.15 and 0.2 strain are shown. The data show several important features. Following a jump, the curve exhibits an instantaneous response followed by a transient, as usual. The instantaneous response is such that always $m^i > 0$. The transient is negative, $m^t < 0$, and rather short-ranged, in all cases extending over less than 0.002 strain. The inset to figure 5.3 b) shows a schematic of the stress-strain curve (continuous line) in the vicinity of

the jump to assist the interpretation of the data in the main figure. Three curves are shown: the monotonic curve corresponding to the strain rate before the jump (dashed line), the monotonic curve corresponding to the strain rate after the jump (dashed-dot line) and two segments parallel to this second line starting from the moment of the jump (point A). One of these starts from the point at which the jump begins (A), while the second is shifted down and represents the asymptote of the transient. The values of stress used to evaluate m^i and m^t (eq. 28) are also indicated.

Most revealing, after the transient the stress-strain curve becomes parallel to the monotonic curve corresponding to the respective strain rate and never asymptotes to this monotonic curve. This is opposite to the situation usually observed in solid solutions, such as those of Al and Cu, in which the memory of the deformation prior to the transient is gradually lost and the curve following the transient asymptotes to the monotonic one. This indicates that the structure of the material stores the information about the deformation history. We conjecture that the parameter of importance here is the twin density. Specifically, the twinning rate depends on the strain rate and is less sensitive to the current twin density. As the deformation proceeds, the twins accumulate at a rate determined by the current strain rate. The fact that m_θ^t is essentially zero indicates that there is little memory of the past twinning rate.

The twin density controls the flow stress. Therefore, the twins accumulated prior to the strain rate jump are never lost, the memory of this deformation regime persists after the jump and hence the curve after the jump never asymptotes to the monotonic curve corresponding to the strain rate imposed after the jump. We present microscopic structural observations in the next section to substantiate the conjecture proposed here.

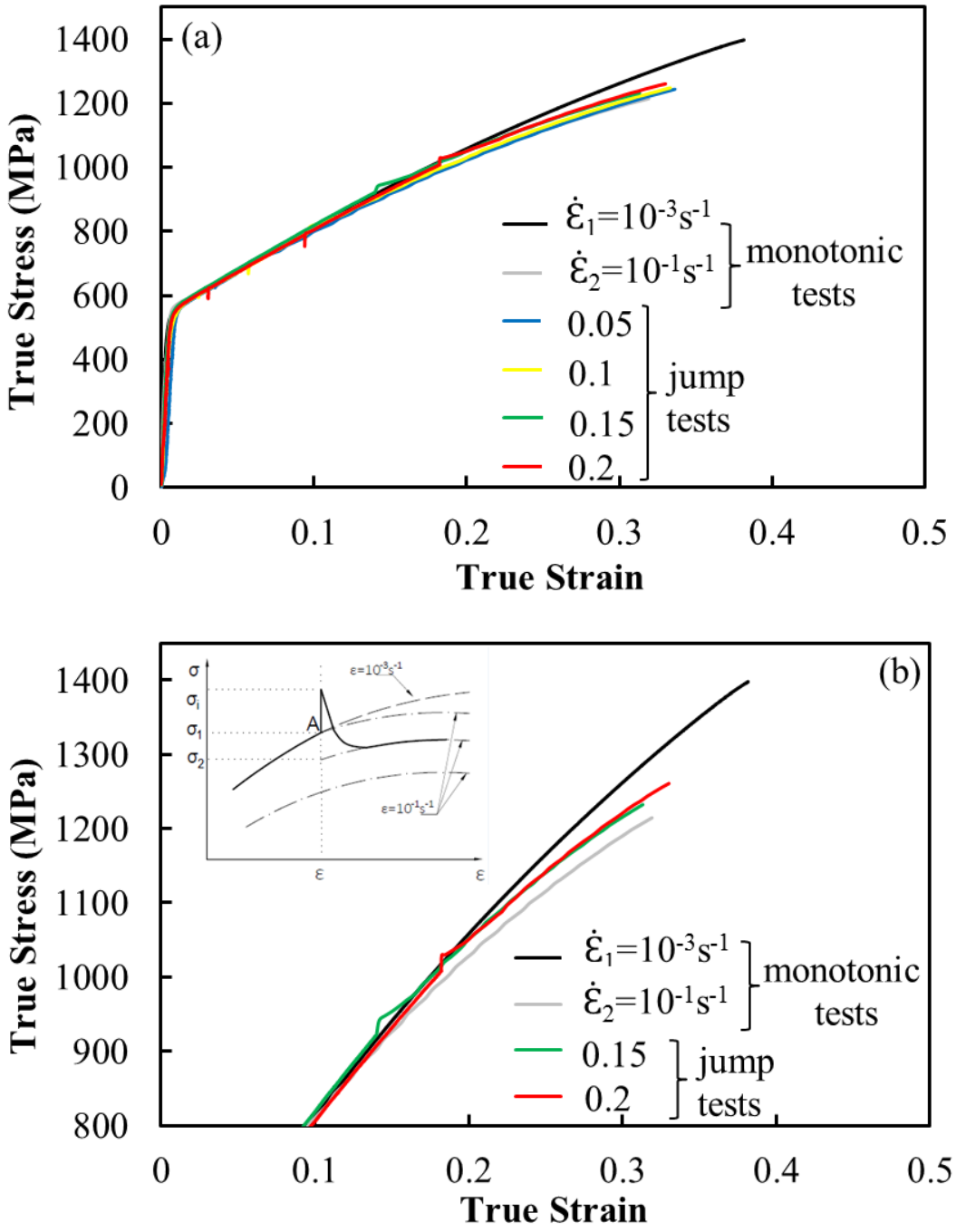

Figure 5.3 *- a) Stress-strain curves corresponding to the monotonic tests performed at 10^{-3} and 10^{-1} s^{-1} and to strain rate jumps from $\dot{\varepsilon}_1=10^{-3}s^{-1}$ to $\dot{\varepsilon}_2=10^{-1}s^{-1}$ performed at 0.05, 0.1, 0.15 and 0.2 true strain (indicated by different colors in the legend). b) Detail of the curves in a). The inset shows a schematic of the curve at a strain rate jump point.*

In order to understand better this effect, the particular case of TWIP steel material is compared with Al-Mg alloy tested in the same conditions. Thus, it can be seen in figure 5.4 that the curve corresponding to a jump test converges after the jump to the curve obtained from a constant strain rate test performed at the same strain rate. It is obvious that in this case the memory of the material is erased.

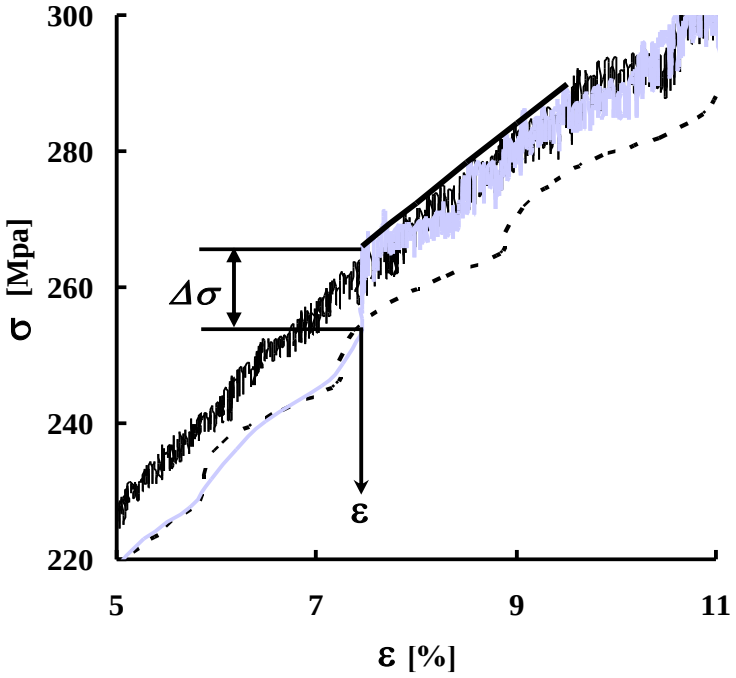

Figure 5.4 *- Al-Mg stress-strain curves of two strain rates in separate and jump test. Note that after jump the curve coincide with the one tested at constant strain rate performed with the respective rate [Vincze2007].*

5.1.3 Strain rate sensitivity response

Figure 5.5 shows the instantaneous (m^i) and total (m) SRS parameters function of strain. The instantaneous component is positive and almost strain-independent, while m decreases continuously with strain and become negative at a true strain of about 0.1. The fact that m < 0 indicates that DSA mechanisms are active, but instabilities and associated serrations of the stress-strain curves are not observed due to the stabilization effect of the large strain hardening rate.

It is important of observe that the strong strain hardening rate sensitivity does not affect the SRS values inferred from strain rate jump experiments. This is due to the fact that the strain hardening rate θ converges very fast to the value associated with the strain rate after the jump, i.e. $m_\theta^t \approx 0$. However, m evaluated from the monotonic curves is affected by the strong SHRS. To demonstrate the difference, we include in figure 5.5 the $m(\varepsilon)$ curve obtained from monotonic tests. Due to the strongly negative m_θ, this curve is below that resulting from strain rate jumps. The difference between them is small at small strains where the SHRS effect is less pronounced.

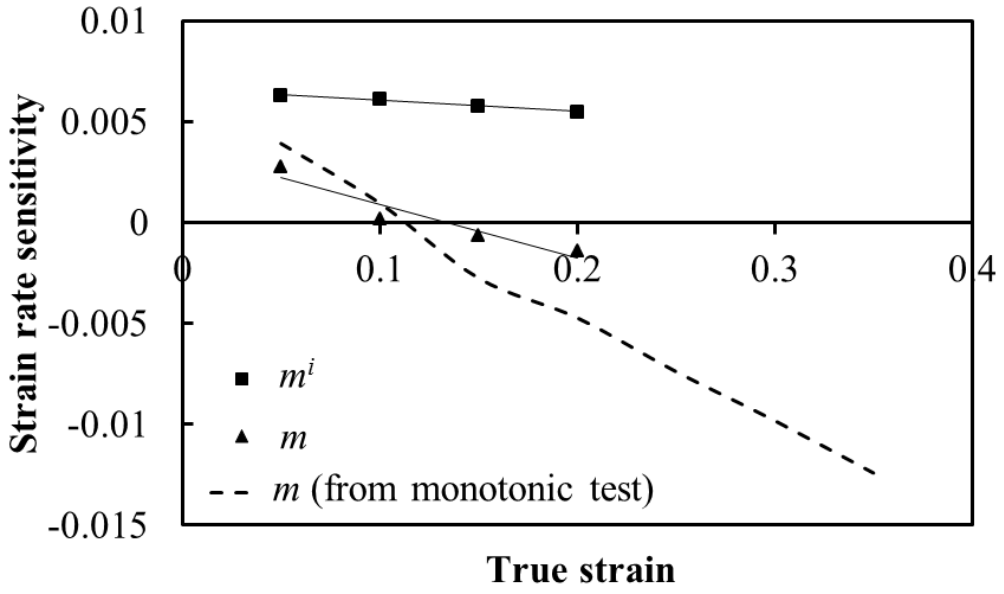

Figure 5.5 *- Instantaneous (m^i) and total (m) SRS parameters variation with the true strain resulting from strain rate jump tests (continuous lines are added to guide the eye). The equivalent m curve resulting from monotonic tests is also shown with dashed line.*

The relationship between the SHRS and SRS parameters can be written as:

$$m_\theta = \frac{\partial log(\theta)}{\partial log(\dot{\varepsilon})} = \frac{1}{\theta} \cdot \frac{\partial}{\partial log\dot{\varepsilon}}\left(\frac{\partial \sigma}{\partial \varepsilon}\right) = \frac{1}{\theta} \cdot \frac{\partial S}{\partial \varepsilon} = \frac{1}{\theta} \cdot \frac{\partial (m\sigma)}{\partial \varepsilon} = m + \frac{\sigma}{\theta}\frac{\partial m}{\partial \varepsilon} \quad (28)$$

where $S = \frac{\partial \sigma}{\partial log(\dot{\varepsilon})}$ is the strain rate sensitivity coefficient. Note that $\sigma > 0$, $\theta > 0$ and $\partial m/\partial \varepsilon < 0$, which implies that m_θ is more negative than m. The expression also suggest which mechanisms contribute to defining the SHRS parameter m_θ. If m and moreover $\partial m/\partial \varepsilon$

are affected by the mechanism producing DSA, the ratio σ/θ depends primarily on the twin density and the twinning rate. Therefore, m_θ is controlled by all these mechanisms.

Negative SRS was previously observed by several groups (e.g. [Kim2009$_a$, Chen2007, Zavattieri2009, Christian and Mahajan1995, Shen2006, Chun2011]) in TWIP steels and in other alloys in which intense twinning plays a central role in mechanical behavior. There seems to be no consensus on the mechanism causing $m < 0$, with potential mechanisms indicate being a) a negative strain rate dependence of the twin nucleation stress, b) of the twin growth rate and c) the general mechanisms leading to negative SRS in solid solutions and known collectively as DSA. The main contribution of this chapter is to indicate that while DSA may contribute to rendering m negative, the strain rate dependence of the twinning mechanism affects the strain hardening rate. The flow stress is controlled by the current twin density and only the strain hardening rate, θ, depends on the rate of twinning, which in turn depends on the strain rate (as shown in the next section). Hence, twinning contributes to the SHRS, while DSA affects the SRS.

Figure 5.6 shows the effect of texture on the measured values of strain rate sensitivity versus true strain obtained from monotonic tests and strain rate jump tests. Two orientations are considered: perpendicular and parallel to the rolling direction (0^o and 90^o). The values of m obtained from strain rate jump tests are only weakly sensitive to the texture. This result is consistent with data for face centered cubic solid solutions, such as Al and Cu alloys.

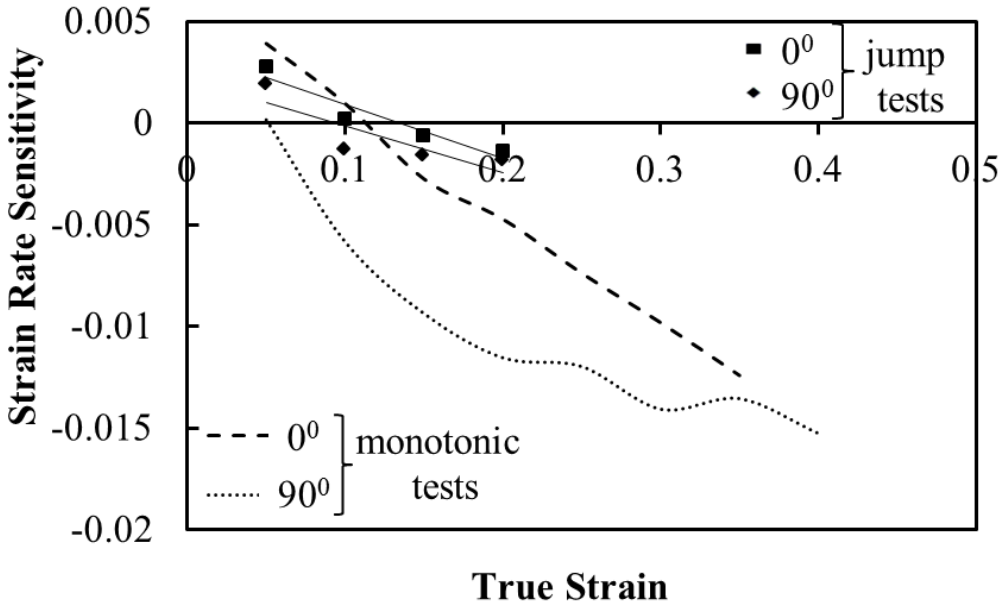

Figure 5.6 *- Strain rate sensitivity as a function of true strain for TWIP steel samples deformed using continuous strain rates of* $\dot{\varepsilon}_1 = 10^{-3}\ s^{-1}$, $\dot{\varepsilon}_2 = 10^{-1}\ s^{-1}$ *and jump tests.*

Allain et al. indicate that strain localization in an austenitic 22Mn0.6C steel was due to localized heating [Allain2008]. The temperature increase was evaluated and correlated with the occurrence of narrow Portevin LeChatelier (PLC) bands. To determine the temperature rise due to plastic deformation in our samples, we measured the temperature with a thermocouple attached on the surface of the sample. In figure 5.7 can be observed that the temperature increases almost linearly with the true strain with a rate of 0.15 ºC/% of true strain at $\dot{\varepsilon} = 10^{-3}s^{-1}$ and 0.66 ºC/% of true strain at $\dot{\varepsilon} = 10^{-1}s^{-1}$. The total temperature rise (above the ambient temperature) before failure is 6ºC and 22ºC for the samples deformed at $\dot{\varepsilon} = 10^{-3}s^{-1}$ and $10^{-1}s^{-1}$, respectively. We consider this increase in temperature insufficient to modify substantially the mechanical behavior.

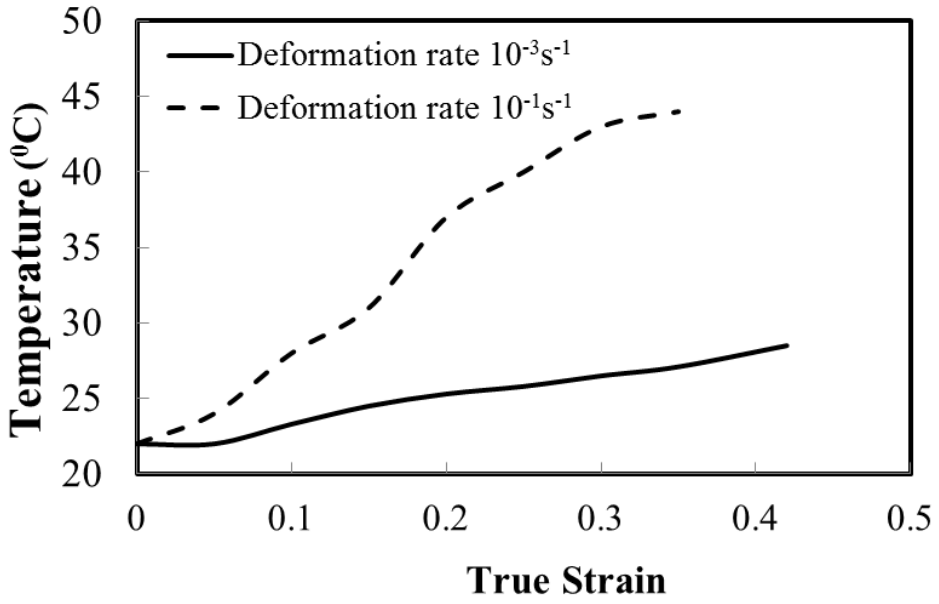

Figure 5.7 *- Variation of sample localized temperature with strain rate. Note that no more than 10^0C temperature rise was reveal when tested with the conventional strain rate of $10^{-3}s^{-1}$, and around 30^0C when the strain rate increase to $10=10^{-1}s^{-1}$.*

5.2 Microscopic structural characterization

5.2.1 Microstructure of as-receive samples

A typical undeformed microstructure is shown in figure 5.8. This analysis indicates the presence of a small number of twins with thickness larger than 60 nm. EBSD measurements was performed with a beam step of 60 nm and consequently only twins thicker than this limit can be observed. The twins are identified by detecting 60^o misorientation boundaries within the grains. Their density is not changing significantly with the strain and some are also present in the undeformed samples. Therefore we conclude that they play little role in plastic deformation and that, as reported in the literature, the active twins are much thinner than what can be detected with the resolution of our EBSD instrument. Nevertheless, the EBSD study allows determining the mean grain size and the texture of the sample. EBSD analysis is performed on samples deformed at the two strain rates up to various strain levels and on undeformed samples. On the order of 60 grains are observed for each sample. The grain size is 4.2±0.5 µm and the value decreases slightly with strain, such that at 0.2 deformation a grain size of 3.5±0.5 µm can be measured. The pronounced <111> fibre texture

in the rolling direction sustains deformation twinning which maintains the high strain hardening rate.

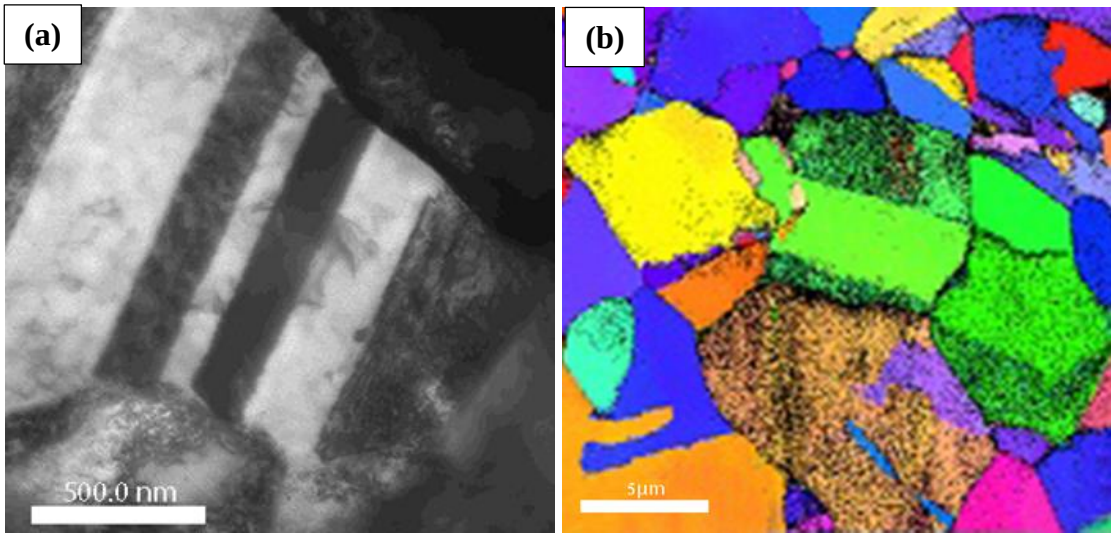

Figure 5.8 *- Microstructure of TWIP Steel in undeformed state (a) TEM micrograph; (b) EBSD Inverse pole figure map.*

5.2.2 Microstructure of deformed samples

Transmission electron microscopy observations of samples deformed at strain rates of 10^{-1} s^{-1} and 10^{-3} s^{-1} and up to true strains levels of 0.1 and 0.2 are also made to detect microstructural features finer than those observable with EBSD. Figure 5.9 shows typical TEM micrographs corresponding to the two strain rates and two strain values. These show both dislocation tangles and twins.

The twins are sharp features with thickness in the range 20 to 100 nm and propagate in many cases across entire grains. Dislocations are present in all images at relatively high densities. The dislocation density is larger in the samples deformed up to 0.2 strain relative to those deformed up to 0.1.

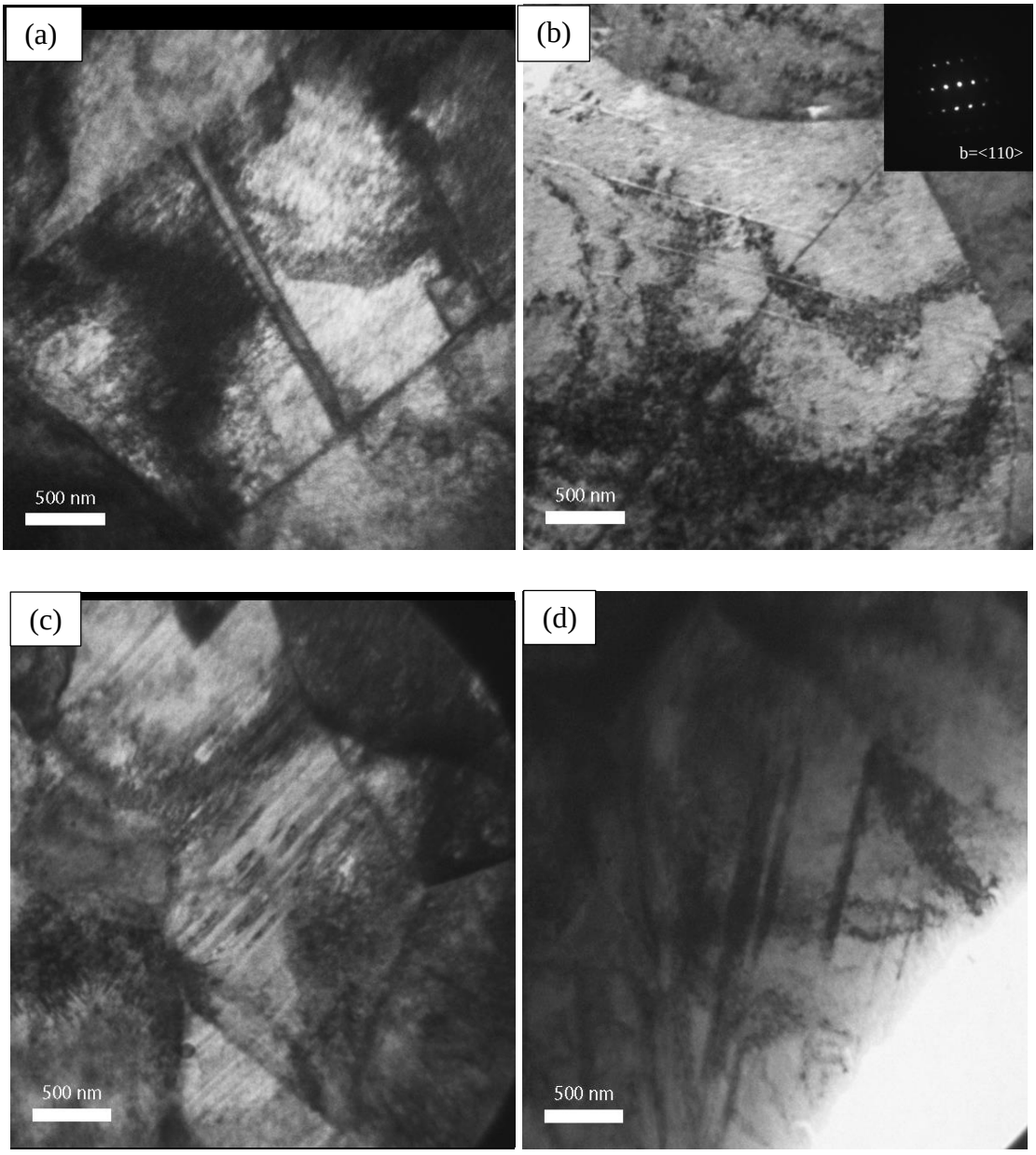

Figure 5.9 *- TEM micrograph of TWIP Steel microstructure tested after a) and b) 0.1 deformation at strain rates: a)$10^{-3}s^{-1}$, b)$10^{-1}s^{-1}$; c) and d) 0.2 deformation at strain rates: c) $10^{-3}s^{-1}$, d) $10^{-1}s^{-1}$. The selected area diffraction of the corresponded micrograph b) is shown.*

Dislocations do not seem to be positioned in any particular relation with the twins, but dislocation tangles are seen close to the twin boundaries. After tilting near the *b=<110>* zone axis the indexed patterns of the twins diffraction spots are identified. The diffraction pattern corresponding to the respective microstructure is shown in figure 5.9 b).

The most important observation for the present discussion refers to the twin density. No significant difference is seen between the two strain rates at 0.1 strain. Both twin and

dislocation densities are approximately the same. This agrees with the fact that at this strain the stress-strain curves for the two strain rates are almost identical. At 0.2 strain, the samples deformed slower exhibits a drastic increase of the twin density. This is in sharp contrast with the samples deformed up to 0.2 strain at the faster rate which exhibit about the same twin density as at 0.1 strain. To provide quantitative support, the number of twins per μm^2 of the TEM maps is evaluated directly from the micrographs. Specifically, we obtain 0.5 and 0.35 twins/μm^2 in samples deformed to 0.1 strain at 10^{-1} and 10^{-3} s^{-1}, and 0.4 and 0.87 twins/nm^2 in samples deformed up to 0.2 strain at 10^{-1} and 10^{-3} s^{-1}, respectively. This observation substantiates the interpretation of the macroscopic test results presented in section 5.1. In samples containing the higher twin density, the twins are less regular and have boundaries less neatly defined.

5.3 Partial conclusions

In this Chapter, an experimental and microstructural study of the deformation behavior of TWIP steel is presented. It was showed that twinning rate depends strongly on the applied strain rate. More intense twinning occurs at smaller deformation rates. This leads to negative strain hardening rate sensitivity, i.e. more pronounced strain hardening at smaller rates.

The strain rate sensitivity of this type of TWIP steel is positive at small strains, but decreases to negative values as the strain increases. The fact that $m < 0$ indicates that DSA mechanisms are active, this does not lead to instabilities and associated serrations of the stress-strain curves due to the stabilizing effect of the large strain hardening rate of the material.

The relationship between the SHRS and SRS parameters was shown. It suggest which mechanisms contribute to defining the SHRS parameter. While strain rate sensitivity is affected by the mechanism producing DSA, the strain hardening rate sensitivity depends primarily on the twin density and the twinning rate.

Typical TEM micrographs corresponding to the TWIP samples deformed at two strain rates and two strain values show the variation of twin density with applied strain rate and correlate well with the results obtained from mechanical tests.

CHAPTER 6

Size effects in measured SRS of TWIP steel

CHAPTER 6 - Size effects in measured SRS of TWIP steel

This chapter presents a continuation of the study on the strain rate sensitivity and strain hardening rate sensitivity of TWIP steels presented in Chapter 5 of the present thesis. An investigation utilizing nano and micro indentation in combination with SEM/EBSD and mechanical tests of a twinning induced plasticity steel is described. Combining different techniques this work will contribute to a better understanding of the local mechanical properties at the micro-macro scale in relation to their microstructure. Most of the studies from the specialized literature focus on the global deformation of TWIP steel [Barbier2009, Chen2013, Kim2015] while the local-scale underlying mechanism deserves further studies. The correlation of global and local deformation should lead to more insight into the operation of the fundamental mechanisms. The work of Gussev et al. on Ni-enriched austenitic 304 steel it's a relevant example [Gussev2015].

In the previous chapter it was shown that increasing the deformation rate leads to the reduction of the flow stress at given strain. This was associated with an inverse dependence of the strain hardening rate on the strain rate which, in turn, is caused by lower twin nucleation rate at high strain rates. The effect is associated with the time dependence of the twin nucleation and growth processes. Here we extend this work investigating the local response of the material to nano-indentation. It is shown that the mechanical behavior of TWIP steel deformed at different strain rates depends strongly on the scale of observation.

6.1 Global deformation behaviour of TWIP steel

Figure 6.1 shows the true stress-true strain curves corresponding to strain rates 10^{-4} s^{-1} and 0.47 s^{-1}. The yield stress measured at the two rates is approximately identical (~ 550MPa) and the strain rate sensitivity parameter (m) is positive, but small close to zero. Parameter m computed from the monotonic curves becomes negative at larger strains [Bintu2015].

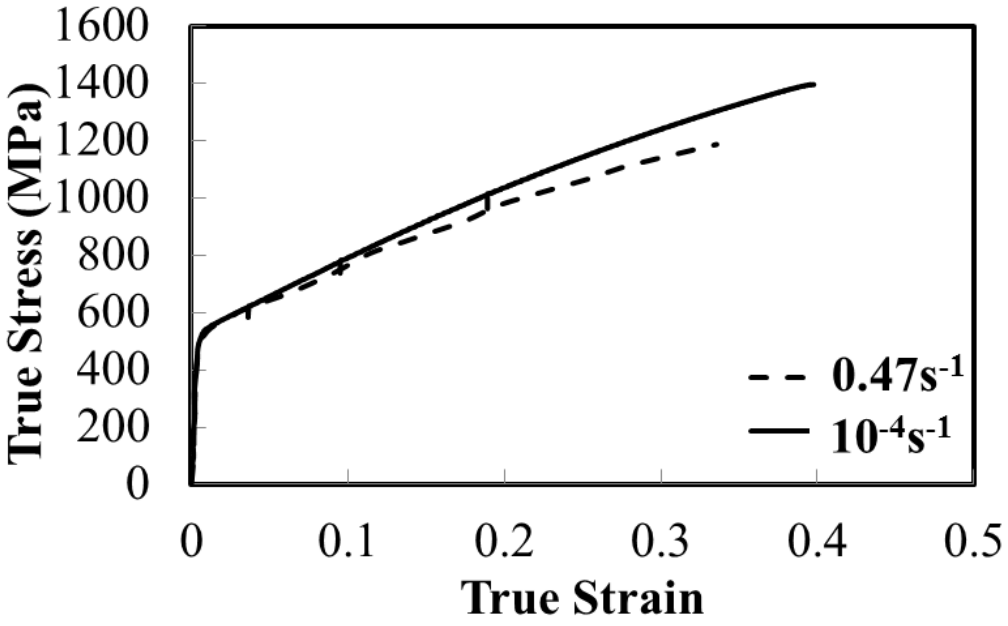

Figure 6.1 *- True stress-true strain curves corresponding to the two indicated strain rates.*

As discussed in Chapter 5 (also outlined in Fig. 5.1), strain hardening is more pronounced for samples deformed with the smaller strain rate and the difference between the small and large strain rate curves increases with strain.

Figure 6.2 shows the variation of *m* with the true strain for monotonic tests shown in fig. 6.1. *m* decrease continuously with strain and at the strain of 20%, which is the pre-deformation strain applied to samples subjected to indentation in the present study, *m* is clearly negative.

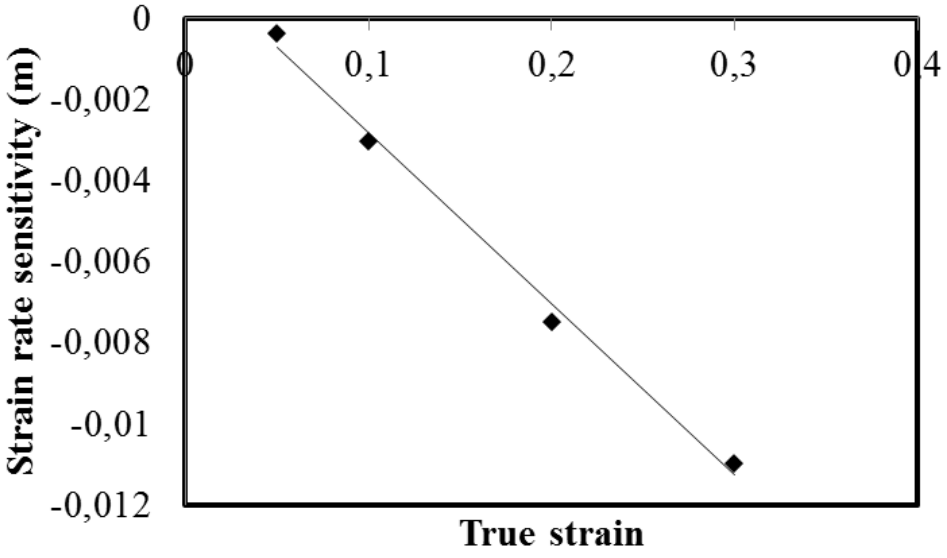

Figure 6.2 - Strain rate sensitivity parameter, m, versus true strain, estimated from monotonic tensile test performed with the two strain rates in fig. 6.1.

In [Bintu2015, Yang2014] this behavior seen in fig. 6.1 and 6.2 was assigned to the higher twin nucleation rate in samples loaded at smaller strain rates. Therefore, the difference between the curves is due to the negative strain hardening rate sensitivity of the material as show in the previous chapter. Moreover, it was observed that samples loaded with smaller strain rates have larger strains at failure and, since the strain hardening is almost strain-independent, larger ultimate tensile strength.

6.2 Local deformation behaviour of TWIP steel

6.2.1 Material behaviour probed by nano-indentation tests and characterized by means of SEM/EBSD

To investigate the local material behavior, were performed a series of nano-indentations in an electropolished surface as shown in SEM figure 6.3 (a). The tests were performed on samples pre-deformed in uniaxial tension up to 20% strain at the two strain rates indicated in figure 6.1. The array in micrograph 6.3 (a) contains 20x20 indents performed using the same tip and up to maximum force of 7 mN. SEM and EBSD images of this region of the surface were acquired before and after indentation. Figure 6.3 (b) shows the

EBSD orientation map obtained after indentation and corresponding to the sample region shown in figure 6.3 (a). The indents fall in different grains having different crystallographic orientation relative to the sample surface normal. No obvious texture is observed in this sample.

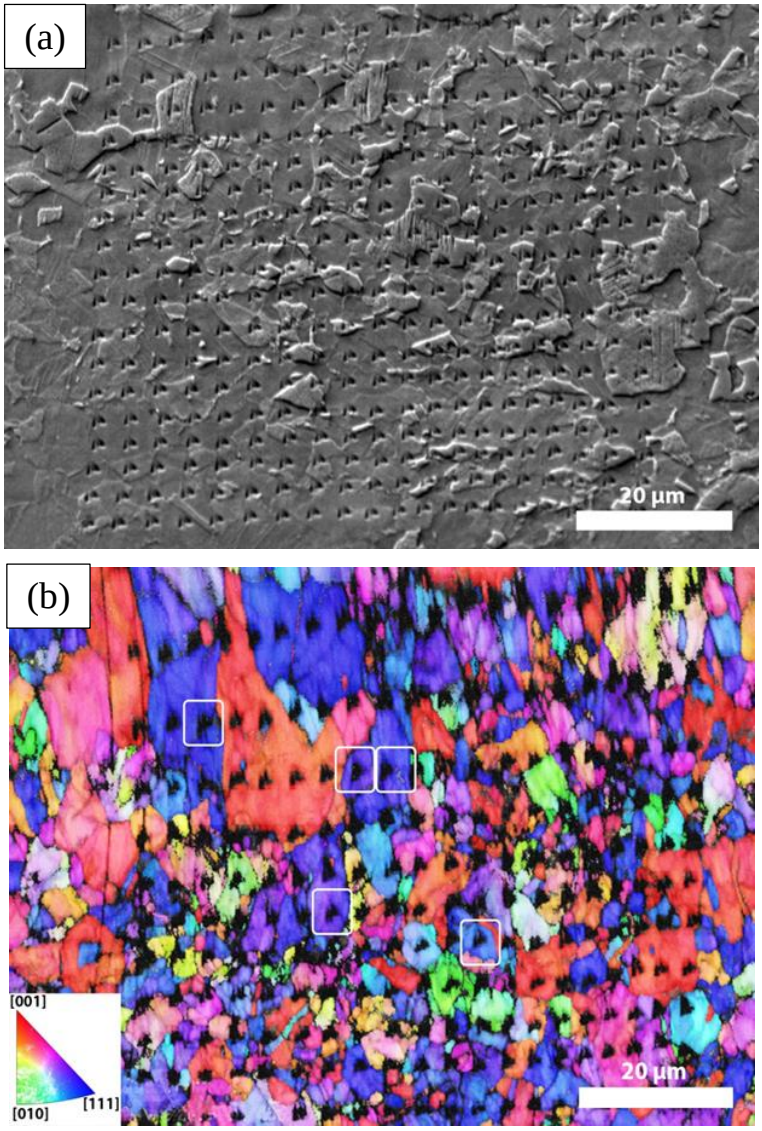

Figure 6.3 *- a) SEM of the surface on which an array of 20 X 20 nano-indentations was performed. The material was pre-deformed up to 20% strain at a strain rate of $10^{-4}s^{-1}$; b) IPF-X and Pattern quality EBSD map corresponding to the image in (a). The white squares indicate indents in grains with <111> orientation for which force-displacement curves are shown in figure 6.4 below.*

The average force-indentation depth curves obtained from the 400 indents, for samples pre-deformed at 10^{-4} s^{-1} and 0.47 s^{-1}, are shown in figure 6.3.

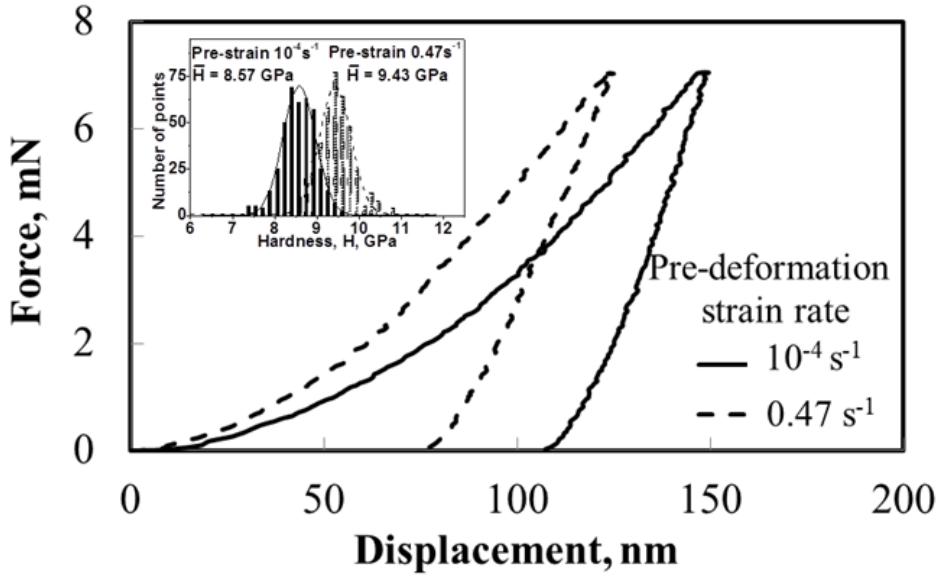

Figure 6.4*- a) Average indentation force–indentation displacement curves for samples pre-deformed at the two strain rates indicated in the figure and up to 20% strain. The average is performed over all 400 indents in the array showed in figure 6.3. The inset shows the histograms of the hardness corresponding to the two cases.*

A clear difference is seen between the two curves: that corresponding to the sample pre-deformed at the smaller rate exhibits much larger indentation depths at the same applied force. This sample appears to be significantly plastically softer. At the same time, the unloading branches of the curves are essentially parallel, which indicates similar average elastic constants. This agrees with the observation that the elastic unloading branches of the stress-strain curves for samples deformed at the two strain rates have the same slope (not shown in figure 6.1). The inset of figure 6.4 shows the histogram of hardness values measured in the 400 indents. The distribution is not a delta function since the values correspond to grains with different orientation. The most important observation is the shift to smaller values of the entire distribution corresponding to the sample pre-deformed at smaller strain rate. This quantifies the effect seen in the average sense in the main figure.

The intriguing observation here is that the trend seen in figure 6.4 is opposite to that observed macroscopically (figure 6.1). The macroscopic flow stress of the sample deformed

at 10^{-4} s^{-1} is larger than that of the sample deformed at 0.47 s^{-1}, while its nanoscale hardness is smaller. The strain rate sensitivity parameter computed from the monotonic curves in figure 6.2 is negative, while the effective strain rate sensitivity computed based on nanoscale hardness values is positive.

To make this observation more specific, we select from the array of indents only curves corresponding to a specific crystallographic orientation. The orientation is identified based on the EBSD map which is also used to determine whether twins pre-exist in each indented grain or not. We are only able to identify twins of thickness above the resolution of the EBSD instrument i.e. thicker than 60nm. The effect of crystal orientation in TWIP Steels has been investigated by several authors mainly by means of tension and compression tests [Saleh2013, Li2013$_b$]. Nevertheless, few information are available in the literature about the orientation-dependencies of the material through nanoindentation.

Figure 6.5 shows several such force-indentation depth curves obtained from the sample pre-deformed at 10^{-4} s^{-1} and from grains with <111> orientation.

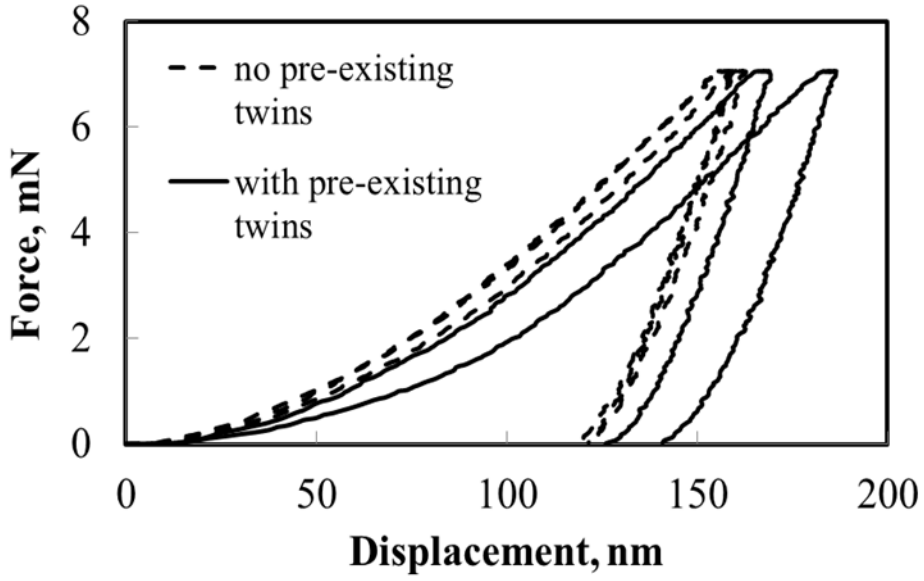

Figure 6.5 *-Indentation force- displacement curves corresponding to grains <111> oriented marked with the five white squares in 6.3b). The curves marked with continuous and dashed lines correspond to indents in grains with and without pre-existing twins.*

The continuous curves correspond to indents in grains in which twins are observed before indentation. The dashed curves correspond to indents in grains with no visible twins

before indentation. The curves clearly separate in the horizontal direction, with those corresponding to twinned grains showing higher plastic compliance, which agrees with the average results shown in figure 6.5.

Similar conclusions are obtained when selecting other crystal orientations. For example, the <100> oriented grains without visible twins lead to a maximum indentation displacement (at 7 mN) of about 140 nm, while those with pre-existing twins have indentation displacements as high as 200 nm at the same maximum force. It should be also noted that indentation with these small forces does not produce twins. This is concluded based on the AFM maps obtained before and after the indentation test.

To investigate this further, we increased the maximum applied force gradually up to 200 mN and observed that twins form with higher probability during indentation only when forces larger than 50 mN are applied. One evidence is shown in figure 6.6 by means of AFM image taken before (a) and after (b) the nano-indentation using a force of 150mN. Nucleated twins are highlighted by red arrows.

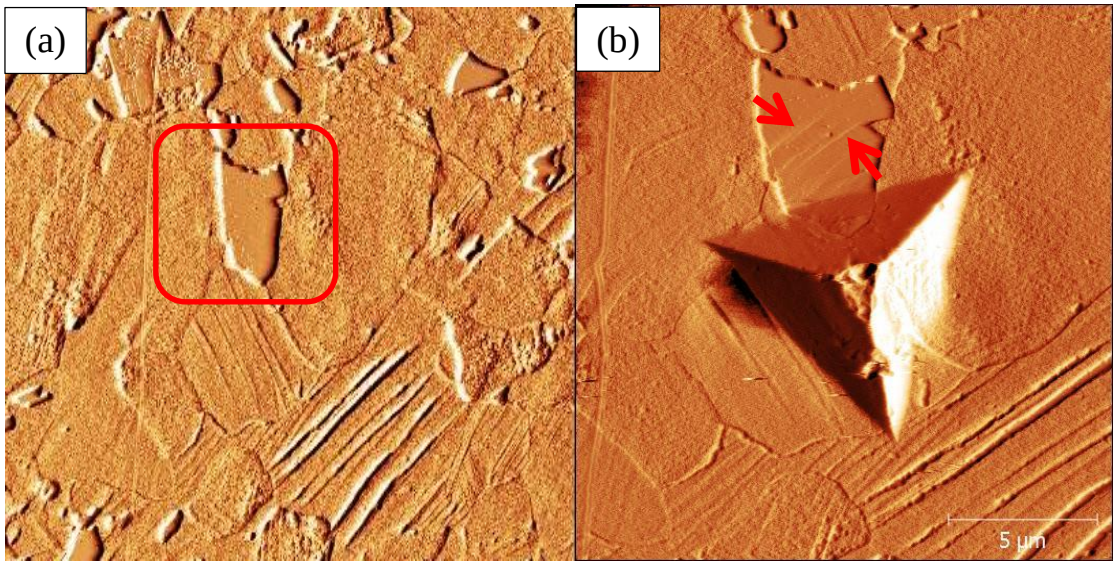

Figure 6.6 *– a) AFM micrograph taken before the nano-indentation of TWIP steel sample pre-deformed up to 20% strain at $10^{-4}s^{-1}$, b) AFM imagine taken after the nano-indentation of TWIP steel sample pre-deformed up to 20% strain at $10^{-4}s^{-1}$ and tested with F=150mN. See the creation of new twins highlighted by red arrows*

We have also studied the effect of the indentation rate by increasing the rate from the reference of 20 mN/min to 200 mN/min (identical for the loading and unloading branches of

the curve) in figure 6.8. The maximum force applied was 100 mN in these tests. As in the macroscopic test, we conclude that twins form with higher probability during indentation performed at the lower indentation rate of 20 mN/min. Comparing AFM maps taken before (figure 6.7 a)) and AFM+EBSD maps after proceed these indents (figure 6.7 b),c)) confirm that twinning takes place during indentation in a large number of cases in these experiments.

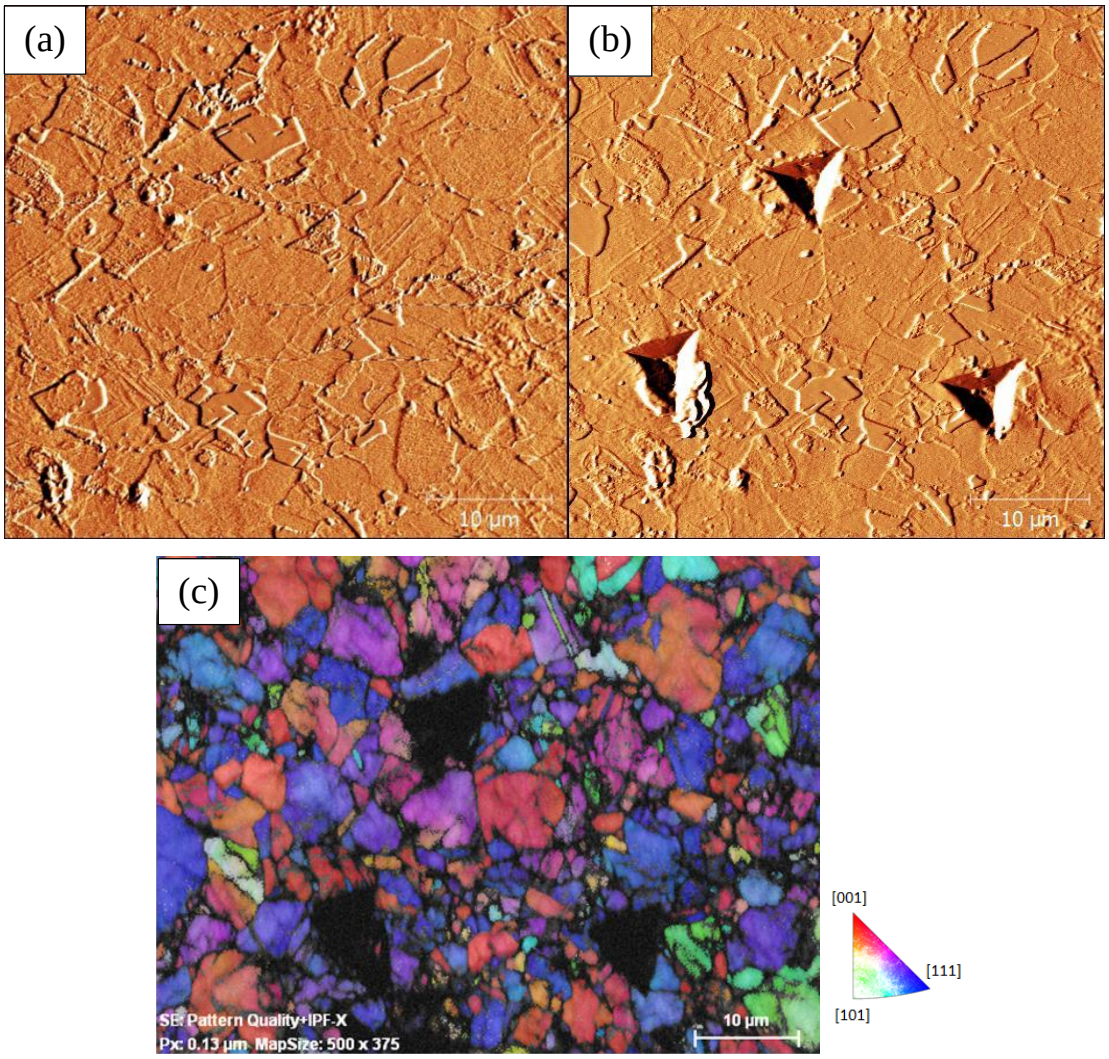

Figure 6.7 *- a) AFM image taken before the indentation of TWIP steel sample pre-deformed up to 20% strain at $10^{-4}s^{-1}$, b) AFM imagine taken after the 3 indentation of TWIP steel sample pre-deformed up to 20% strain at $10^{-4}s^{-1}$ and tested with changing speed of indentation from 2 to 200mN/min, c) EBSD map corresponding to b).*

We present in figure 6.8 the curves obtained from indentations performed with the two rates of 20 and 200 mN/min in a sample pre-deformed up to 20% at 10^{-4} s^{-1}. It is observed that although more twinning activity is observed at the lower indentation rate, the response is plastically more compliant, which agrees with the result shown in figure 6.4

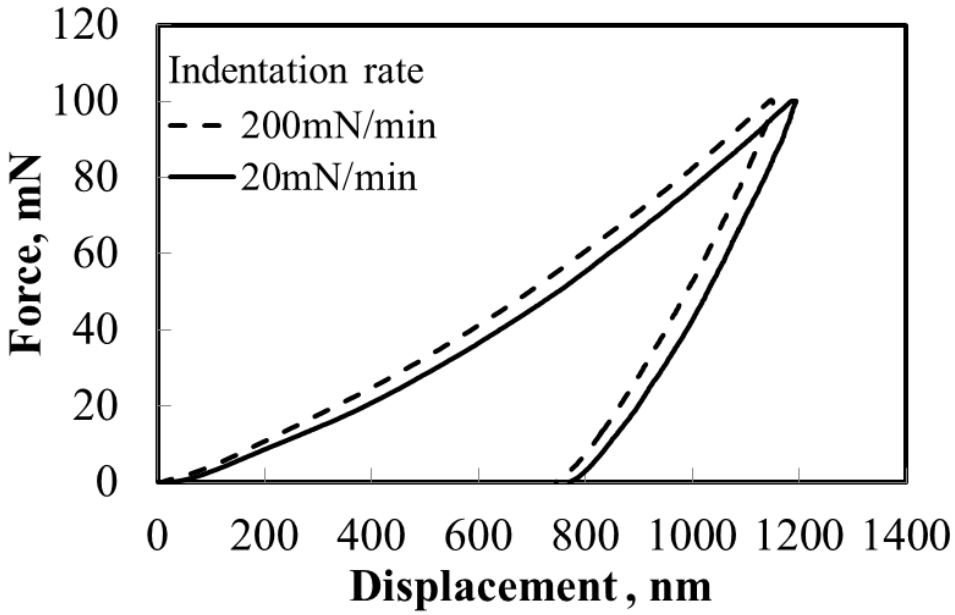

Figure 6.8 *- Load–displacement curves of the TWIP steel sample pre-deformed up to 20% strain at $10^{-4}s^{-1}$ and tested with two indentation rates of 200mN/min and 20mN/min.*

As seen above in the figure 6.8, the effective hardness decreases when twinning occurs during indentation. Sanchez-Martin et al [Sanchez-Martin2015] also observed that high twinning activity leads to smaller apparent hardness in pure Mg. Their samples were not pre-deformed and twins formed dynamically during indentation. The comparison should be made with care though given the different nature of the TWIP and Mg lattices.

This data set indicates that plastic deformation is favored in presence of twins. Considering a simple uniaxial compression loading of a crystal, it is possible to compute the resolved shear stress in the twin composition plane and the twinning direction for all potential twin systems in the FCC structure. Due to the high symmetry, at least one twin system is loaded with a shear stress equal to at least 38% of the applied normal stress (76% of the absolute maximum shear stress) for all directions of the compression axis relative to the principal crystallographic axes. Hence, indentation leads to large resolved shear stresses on

one or multiple potential twin systems in all indented grains. We conclude that the more intense plastic activity observed in the presence of twins is due to the motion of dislocations along twin interfaces, motion which is not hindered by the presence of other twins or forest dislocations in the material. This type of dislocation activity should lead to the increase of the visible twin thickness. However, the resolution of the current EBSD measurements is insufficient to allow the direct observation of this effect.

Let us also observe the more pronounced recovery strain during unloading in the presence of twins (compare continuous lines with dashed lines in figure 6.5). This can be associated with the fact that dislocation motion along the composition planes is more ordered and hence plastic strain recovery is facilitated.

6.2.2 Material behaviour probed by micro-indentation tests

The observation that *m* measured from the monotonic macroscopic tests shown in figure 1 is negative, while *m* measured using the hardness values obtained from nanoscale test is positive requires further investigation at different scales.

This micro-indentation hardness determines the strength of materials measuring the depth or area of an indentation left by an indenter of a specific shape, with a specific force applied for a specific time [Arbtin1953]. To this end, Vickers and Rockwell micro-indentation tests were performed. It was estimate that in the Vickers test the volume of material plastically probed is equivalent to about 1200 grains, while in the Rockwell test approximately 36400 grains are probed since the indenter and imprints are larger in this case. Therefore, the two tests provide information relevant for different probing scales. In both cases we tested samples pre-deformed up to 20% strain at $10^{-4}s^{-1}$ and $0.47s^{-1}$. The mean HV values are 399±3 and 400±4 for the samples pre-deformed at $10^{-4}s^{-1}$ and $0.47s^{-1}$, respectively. The mean HRC values are 42±0.8 and 40.1±1 for the samples pre-deformed at $10^{-4}s^{-1}$ and $0.47s^{-1}$, respectively.

At the macroscopic scale, the difference between the flow stress values of the two types of samples (at 20% plastic strain) is -5.8% (the reference is the flow stress of the sample deformed with the lower strain rate). The difference between the HRC results is -4.5%, while the difference between the HV mean values is essentially zero. At the same time, the nano-indentation test leads to a difference of +9.1% (inset to figure 6.3).

The effective sensitivity of the HV values is $m_{HV-micro} = \log(HV_1/HV_2)/\log(\dot{\varepsilon}_1/\dot{\varepsilon}_2) \approx 0$. The effective sensitivity of the HRC values is $m_{HRC-micro} = \log(HRC_1/HRC_2)/\log(\dot{\varepsilon}_1/\dot{\varepsilon}_2) \approx -0.005$. The mean nano-hardness of the sample pre-deformed at 10^{-4} s^{-1} is $\overline{H}_1$ = 8.57 GPa, while that of the sample pre-deformed at 0.47 s^{-1} is $\overline{H}_2$ = 9.43 GPa. Using these values to compute an effective sensitivity of the nano-hardness to the pre-deformation rate, one obtains $m_{H-nano} = \log(\overline{H}_1/\overline{H}_2)/\log(\dot{\varepsilon}_1/\dot{\varepsilon}_2) = 0.011$. This should be compared with the value shown at 20% strain in Fig. 6.1 for the monotonic tests, which his m = -0.0075. The representation of SRS values obtained from macro, micro and nano scales is shown in the figure 6.9 below.

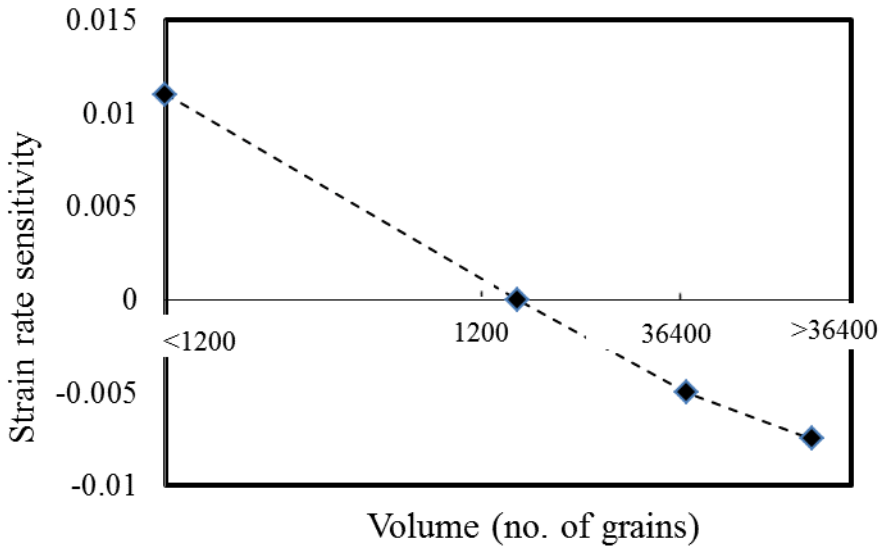

Figure 6.9 *- Strain rate sensitivity parameter, versus numbers of grains, estimated from nano-indentation, micro-hardness and macroscopic tests.*

Clearly, as the probed volume increases, the effective strain rate sensitivity becomes negative. The scale above which the macroscopic result is recovered corresponds to approximately 36400 grains, or ~240 µm.

6.3Partial conclusions

In this chapter it was investigated the local and global response of TWIP steel using nano-indentation, micro-indentation and uniaxial tensile testing. The apparent strain rate sensitivity of the material depends strongly on the scale of observation. Samples pre-deformed at large strain rates contain a smaller density of twins. These samples have smaller flow stress than samples deformed at higher rates, however they have larger nano-hardness. As the volume of material probed increases, the relative hardness of the two types of samples gradually shifts from the trend observed at the nanoscale to that observed macroscopically. This is attributed to the difference between the ways the dislocation-twin interaction mechanism is activated in the nanoscale and macroscale tests and sheds light on the effect of averaging over larger and larger volumes of material on the effective mechanical behavior.

It can be concluded that samples with linear dimensions larger than about 240 μm (equal to the diameter of about 36400 grains in our material) exhibit the trends observed at the macroscopic scale.

CHAPTER 7

Final conclusions and future perspectives

CHAPTER 7 - Final conclusions and future perspectives

7. 1 Final conclusions

The scientific merit of this research derives from the investigation of fundamental deformation mechanisms in two important engineering materials, AA5182 and TWIP steel. The development of different experiments to verify, control and explain the origin and evolution of strain rate sensitivity parameter and the macroscopic materials behavior based on small scale physics, provide a qualitative picture of the deformation of these alloys.

The main conclusions of the present study are presented as follows, for each studied alloy in part.

7.1.1 AA5182

Although a qualitative picture of the deformation mechanism of AA5182 already exist for over fifty years, quantitative theories that predict the microscopic observed behavior in terms of SRS with heat treatment in ufg state are rare in the literature. A clear understanding of the response under different deformation routes is crucial for this material future applications as a high-strength lightweight alloy.

The main objective related with the deformation behavior of AA5182 was to improve its strain rate sensitivity via severe plastic deformation. To accomplish this, the processing paths that lead to the best results were selected. It was shown that a judicious selection of type of rolling and follow-up heat treatment may lead to both increased flow stress and improved (close to zero) strain rate sensitivity.

Three different cold rolling techniques (SR, ASRR and ASRC) used to develop ultrafine grain size were chosen and compared. Another important aspect of the process are the four post-rolling heat treatments. The evolution of microstructure in terms of grain size and texture, the evolution of yield stress and hardening rate or the effect of the critical strain

for onset of PLC, are some of the by-products that will help to understand the deformation of AA5182 by severe plastic deformation.

Taking this into consideration, the following conclusions can be drawn:

a) The results of strain rate sensitivity (*m*) obtained after performing different asymmetric and symmetric rolling reduction (25%, 50%, 66% and 90%) followed by uniaxial tensile tests with continuous strain rate of $10^{-3}s^{-1}$ and $10^{-1}s^{-1}$, shows that *m* increase with increasing the degree of rolling; the effect is visible only after about 50% reduction. At 90% reduction, *m* remains negative, but is close to zero.
b) Considering the uniaxial tensile tests, the results indicate that the yield stress is increasing with increasing rolling reductions while the ductility decreases. The three techniques (ASRR, ASRC, SR) are not identical in terms of the equivalent plastic strain they provide. Thus, one can observes that SR is less efficient in increasing the flow stress than ASRR while the stain hardening rate remains unchanged. ASR is more effective in producing these effects, and ASRR is superior to ASRC from this point of view. Also ASRR technique appear to be the most efficient in increasing the strain rate sensitivity parameter
c) The schedule of the heat treatment makes a difference only for samples rolled to 90% reduction. In these cases the yield stress of symmetrically rolled samples decreases with increasing annealing time (from HT1 (30min) to HT4 (120 min)), while that of asymmetrically rolled samples increases. The strain hardening rate is independent of the type of heat treatment applied and is also largely independent of the rolling reduction for reductions larger than 20%.
d) Microstructural observations indicate that the grain size decreases continuously with increasing rolling reduction, being more pronounced for reductions larger than 50%. Rolling introduces low angle grain boundaries at reductions below 50%, which transform in high angle boundaries at higher reductions. Nanoscale grains are obtained with all rolling methods at 90% reduction.

Several mechanisms which may lead to the observed increase of m upon rolling:

1. Severe plastic deformation introduces (low angle grain boundaries) LAGB at small equivalent plastic deformation and HABG (high angle grain boundaries) at higher plastic strains. The increase of strain rate sensitivity with increasing rolling reduction may be based on the interaction of dislocations with HAGB leading to nanoscale grains.
2. Another mechanism is related to the concentration of Mg in solid solution. Plastic deformation reduces the concentration of Mg atoms free to diffuse and hence *m* increases. This can be explained based on the observation that for larger reductions the density of dislocations and interfaces that may getter Mg increases and thus the effective concentration of Mg in solid solution decreases. Solute may form clusters and plastic deformation leads to the partial dissolution of such clusters leading to an increase of *m*. Moreover, with increasing the annealing time, at larger reductions, these cluster may reform resulting in an increase of the yield stress.

7.1.2 TWIP steels

The main purpose of this part of research was to investigate the relationship between twinning rate and the applied deformation strain rate in an 18% Mn TWIP steel and to observe the effect of this dependence on the macroscopic rate sensitivity of the material. This work was extended to investigate the local deformation response of the material to nano-indentation. The correlation between SRS and probing scale was revealed. Uniaxial tensile tests, hardness tests and microstructural characterization by means of TEM, SEM and EBSD were performed to picture the global and local deformation behavior of the TWIP steel used in this thesis.

The experimental study presented here leads to the following conclusions:

a) It was determined that increasing the strain rate from $10^{-3}s^{-1}$ to$10^{-1}s^{-1}$ leads to lower twinning rate which leads to lower flow stress measured in a macroscopic uniaxial test. This translates in less strain hardening and hence a negative strain hardening rate sensitivity (SHRS).
b) The strain rate sensitivity of the material is measured and placed in relation with SHRS. The conclusions are obtained based on microscopic structural observations and

macroscopic mechanical characterization of the material. The instantaneous component of m is positive and almost strain-independent, while *m* decreases continuously with strain and become negative at a true strain of about 0.1

c) Three potential mechanisms contribute to define the SHRS parameter: i) a negative strain rate dependence of the twin nucleation stress, ii) the twin growth rate and iii) DSA which is responsible of rendering *m* negative. Hence, come the conclusion that twinning contributes to the SHRS, while DSA affects the SRS.
d) Direct observations of the strain rate dependence of the twinning rate are made using electron microscopy and electron backscatter diffraction, which substantiate the proposed mechanism for the observed negative SHRS.
e) The mechanical behaviour of TWIP steel deformed at different strain rates depends on the scale of observation. When probed at the nanoscale by nano-indentation, samples pre-deformed in tension at smaller strain rates ($10^{-4}s^{-1}$) exhibit systematically smaller hardness than samples pre-deformed at higher rates ($0.47s^{-1}$).
f) Therefore, the strain rate sensitivity evaluated based on the nanoscale hardness values is positive. The strain rate sensitivity measured by micro-hardness gradually shifts to negative values as the indenter size and hence the probed volume increase. The effect is linked to the ways the dislocation-twin interaction mechanism is activated in the nanoscale and macroscale tests.
g) It was shown that the scale above which the macroscopic result is recovered corresponds to approximately 36400 grains, or ~240 μm. It can be concluded that samples with linear dimensions larger than about 240 μm (equal to the diameter of about 34 grains in present material) exhibit the trends observed at the macroscopic scale.

7.2 Future perspectives

Based on the high quality sheet metal manufacturing demands, mostly in the automotive industry, the experimental results that this thesis presents can open new directions of research based on the evaluation of strain rate sensitivity over the formability of AA5182 and TWIP steel.

7.2.1 AA5182

As a future research, finite element simulation may be a useful tool to develop multi-scale models to link macro- and micro- deformation behavior of AA5182. In order to fully understand the links between material behavior at different scales this future process design will help to further improve SRS and the parameters utilized to increase the shear strain through asymmetric rolling process.

The microstructure evaluation may continue with investigation of the subgrain microstructure utilizing advanced characterization techniques. Recent advances in electron microscopy provide a number of new analytical techniques that expand its application in material science studies. High-angle annular dark field scanning transmission electron microscopy (HAADF-STEM) can be effectively used to identify and characterize grain refined aluminum-magnesium alloy through asymmetric rolling and annealing at different conditions. It shows atomic number contrast for high scattering angles of the electrons, owing to predominant electron scattering at the potential of the nucleus similar to Rutherford scattering [Nukala2008, Pennycook2011]. In other words, the image contrast in HAADF-STEM is strongly correlated to the atomic mass: heavier elements contribute to brighter contrast.

Elemental probing in the HRTEM will be used to determine the spatial distribution of the solute and potential clustering. Solute clustering is expected at dislocations and grain boundaries, but may also occur in absence of lattice defects. The quantification of the degree of solute (Mg) clustering is essential when trying to understand the mechanisms of DSA and the corresponded negative strain rate sensitivity.

7.2.2 TWIP Steels

The extended research regarding TWIP steels may include, mechanical testing at elevated temperatures, under uniaxial, shear and biaxial conditions for the purpose of accumulating a large database of material behavior which can be used for constitutive model calibration and verification.

In Chapter 5 it was shown that the hardening rate is strongly dependent on the strain rate and is entirely controlled by the twin density. In the presence of twinning, one may attempt to write an evolution law for the twin density and incorporate the dynamic Hall-Petch effect [Kim2010]. The twin density evolution may be calibrated via microstructural observations including TEM and HRTEM. Preliminary versions of such constitutive formulations have been recently developed [Xu2008]. These formulations can be improved by inclusion of the new evidence related to the mechanisms controlling the SRS and SHRS presented in Chapter 5 and 6 of this thesis. Of course after that, the ability of the model must be tested and compared with experimental result concerning formability of the TWIP steel.

Another future approach to improve the strength and formability of TWIP steel it can be dedicated to Hole Expansion test. It is known that a crack appears in this kind of test at a much lower hole expansion ratio than in the case of Ti Interstitial-Free (IF) steel [Chen2010]. Therefore, it is important to accurately analyze the deformation behavior and fracture of TWIP steel sheet in this kind of test. At the current time, progress in the simulation technique is necessary to capture the strain distribution properly. More importantly, the cracking cannot be explained satisfactorily without a plausible mechanism. This is where the negative strain rate sensitivity is expected to play a big role in the plastic deformation of sheet metals.

Bibliography

Abbadi M., Hähner P., Zeghloul A., 2002, "On the characteristics of Portevin–Le Chatelier bands in aluminum alloy 5182 under stress-controlled and strain-controlled tensile testing", Mater. Sci. and Eng. A, vol. 337, p. 194-201;

Ahzi S., M'Guil S., 2008, "A new intermediate model for polycrystalline viscoplastic deformation and texture evolution", Acta Mater., vol. 56, p. 5359-5369;

Alhers M., 1970, "Stacking fault Energy and mechanical properties", Met. Trans., vol. 11, p. 2415-2428;

Allain S., Chateau J.P. Bouaziz O., 2004, "A physical model of the twinning-induced plasticity effect in a high manganese austenitic steel", Mater. Sci. Eng. A, vol. 387–389, p. 143-147;

Allain S., Cugy P., Scott C., Chatea, J.P. Rusinek, A. Deschamps A., 2008, "The influence of plastic instabilities on the mechanical properties of a high-manganese austenitic FeMnC steel", Int. J. Mater. Res., vol. 99, p. 734-738;

An X. H., Han W. Z., Huang C. X,. Zhang P., Yang G., Wu S. D., Zhang Z. F., 2008, "High strength and utilizable ductility of bulk ultrafine-grained Cu–Al alloys", Appl. Phys. Lett., vol. 92, p. 201915;

Aoyama S., Urao R., 2010, "Effects of Grain Size and Sn Concentration on Bending Fatigue Life of Cu-Sn Alloy", J. Japan Inst. Metals, vol. 74, p. 49-54;

Ananthakrishna G., 2007, "Negative strain rate sensitivity and the critical nature of type A bands in the Portevin-Le Chatelier effect", Computer-Aided Materials Design, vol. 14, p. 5-14;

Arbtin E., Murphy G., 1953, "Correlation of Vickers hardness number, modulus of elasticity and the yield strength for ductile metals", Atomic Energy commission, p. 356;

Askeland D.,1987, "The Science and Materials Engineering", G.E. Iberoamerica, p. 235249;

Asaro R.J., Suresh S., 2005, "Mechanistic models for the activation volume and rate sensitivity in metals with nanocrystalline grains and nano-scale twins", Acta Mater., vol. 53, p. 3369–3382;

Bayractar E. L., 1993, "Strain rate and temperature effect on the deformation behavior of the original hadfield steel", Journal de Physique, vol. 4, p. 61-66;

Banabic D., 2010, "Sheet Metal Forming Processes: Constitutive Modelling and Numerical Simulation", Springer Science & Business Media, p. 35-37;

Barbier D., Gey N., Bozzolo N., Allain S., Humbert M., 2009, "EBSD for analyzing the twinning microstructure in fine-grained TWIP steels and its influence on work hardening", J. Microscopy, vol. 235, p. 67-78;

Bazarnik P., Lewandowska M., Andrzejczuk M., Kurzydlowski K.J., 2012, "The strength and thermal stability of Al–5Mg alloys nano-engineered using methods of metal forming", Mat. Sci. and Eng. A, vol. 556, p. 134–139;

Berveiller M., Zaoui A., 1979, "An extension of the self-consistent scheme to plastically-flowing polycrystals", Journal of the Mech. and Physics of Solids, vol. 26, p. 325-344;

Bintu A., Vincze G., Picu C., Lopes A., Grácio J., Barlat F., 2015, "Strain hardening rate sensitivity and strain rate sensitivity in TWIP steels", Mater. Sci. and Eng. A, vol. 629, p. 54–59;

Bintu A., Vincze G., Picu R.C., Lopes A.B., 2016 "Effect of symmetric and asymmetric rolling on the mechanical properties of AA5182", Mat and Design, vol. 100. P. 151-156; Show more

Bishop J., **Hill R**., 1951, "A theory of the plastic distortion of a polycrystalline aggregate under combined stresses", Phil. Mag., vol. 42, p. 414-427;

Bouaziz O., Guelton N., 2001, "Modelling of TWIP effect on work hardening", Mater. Sci. Eng. A vol. 319–321, p. 246–249;

Bracke L., Kestens L., Penning J., 2009, "Micro structure and texture evolution during cold rolling and annealing of a high Mn TWIP steel," Acta Mater., vol. 57, p. 1512;

Buerger M., 1945, "The Genesis of Twin Crystals", Am. Mineral, vol. 30, p. 469-482;

Bunge H.J., 1982, "Texture Analysis in Materials Science: Mathematical Methods", Butterworth Publishers, London;

Callister W. D., 1994, "Materials science and engineering: An introduction", 5th ed. Wiley: Technology & Eng., p. 632–633;

Cahn R., 1954, "Twinned Crystals", Adv. Phys., vol 3, p. 363-445;

Cahn J. W., Nabarro F.R.N, 2001, "Thermal activation under shear", Philosophical Magazine A, vol. 81, p. 1409-1426;

Cao W.Q., Godfrey A., 2003, " Annealing behavior of aluminium deformed by equal channel angular pressing", Materials Letters, vol. 57, p. 3767-3774;

Calcagnotto M., Ponge D., Adachi Y., Raabe D., 2009, "Effect of Grain Refinement on Strength and Ductility in Dual-Phase Steels". Proceedings of the 2nd International Symposium on Steel Science. Kyoto: The Iron and Steel Institute of Japan

Carpenter J., Bai C., Escobedo-Diaz J. P., Hwang J., Ikhmayies S., Li B., Li J., Neves S., 2015, "Characterization of Minerals, Metals and Materials", John Wiley & Sons, p. 16;

Charttejee A., Murty K.L., Gayathri N., Mukherjee P., Barat P., 2010, "Temperature Dependence of the Dynamics of Portevin-Le Chatelier Effect in Al-2.5%Mg alloy", Met. Mater. Trans. A, vol. 42, p. 1184-1190;

Chen Y.C., Huang Y.Y., Chang C.P., Kao P.W., 2003, "The effect of extrusion temperature on the development of deformation microstructures in 5052 aluminium alloy processed by equal channel angular extrusion", Acta Mater., vol. 51, p. 2005-201

Chen L., Kim H.S., Kim S.K., De Cooman B.C., 2007, "Localized Deformation due to Portevin-LeChatelier Effect in 18Mn-0.6C TWIP Steel" , ISIJ International, vol. 47, p.1804;

Chen L., Zhao Y., Qin X., 2013, Some Aspects of High Manganese Twinning-Induced Plasticity (TWIP) Steel, A Review", Acta Metall., vol. 26, p. 1-15;

Chen L., Kim J.K., Kim S.K., Kim G.S., Chin K.G., De Cooman, B.C., 2010, "Stretch-Flangeability of High Mn TWIP steel", Steel Research Int., vol. 81, p. 552–568;

Cheng X.M., Morris J.G., 2000, "The anisotropy of the Portevin– Le Chatelier effect in aluminum alloys", Scripta Mater., vol. 43, p. 651-658;

Choi C.H., Kim K.H., Lee D.N., 1998, "The effect of shear texture development on the formability in rolled aluminum alloy sheets", Mater. Sci. Forum, vol. 273-275, p. 391–396.

Christian J.W., Swann P.R., Massalski T.B., 1965, "Alloying Behavior and Effects in Concentrated Solid Solutions", Gordon and Breach, p. 105-269;

Christian J.W., Mahajan S., 1995, "Deformation twinning", Review Article Progress in Materials Science, vol. 39, p. 1-157;

Christian J.W, 2002, "The Theory of Transformations in Metals and Alloys", Newnes Editors, Oxford, UK;

Chun Y.B., Davies C.H.J., 2011, "Twinning-induced negative strain rate sensitivity in wrought alloy AZ31", Mater. Sci. and Eng. A, vol. 528, p. 5713-5722;

Clausen, B., 1997, "Characterization of polycrystal deformation by numerical modelling and neutron diffraction measurement", Risø National Laboratory report, p. 87;

Clausen B., Lorentzen T., 1998, "Self-consistent modeling of the plastic deformation of FCC. polycrystals and its implications for diffraction measurements of internal stresses", Acta Mater., vol. 46, p. 3087-3098;

Cotter K.H., 1967, "Stacking Fault Probability in Aluminum Alloys", M. S. Thesis, University of Arizona, Tucson, Arizona;

Cottrell A.H., Bilby B.A., 1949, "Dislocation theory of yielding and strain ageing of iron", Proc Phys. Soc., A, vol. 62, p. 49-62;

Cui Q., Ohori K., 2000, "Grain refinement of high purity Al by asymmetric rolling", Mater. Sci. Technol., vol. 16, p. 1095-1101;

Curtin W.A, Olmsted D.L., Hector L.G., 2006, "A predictive mechanism for dynamic strain ageing in aluminium–magnesium alloys**"** Nat. Mater., vol. 5, p. 875–880;

Curtze S., Kuokkala V.T. 2010, "Dependence of tensile deformationbehavior of TWIPon stacking fault energy, temperature and strain rate", Acta Mater., vol. 58, p. 5129-5241;

De Cooman B.C., Chin K.G., Kim J.Y., 2011, "High Mn TWIP Steels for Automotive Applications", Graduate Institute of Ferrous Technology Pohang Univ. of Science and Tech., Pohang POSCO Technical Research Lab., Gwangyang South Korea, p. 101-128;

De Sandeep A., Kibey M., 2007, "Mesoscale Models for Stacking Faults, Deformation Twins and Martensitic transformations: Linking atomistics to continuum", PhD Dissertation, University of Illinois, USA;

Derlet P.M., Van Swygenhoven H., Hasnaoui A., 2003,"Atomistic simulation of dislocation emission in nanosized grain boundaries", Phil. Mag., vol. 83, p. 3569;

Dieffenbach J.R. 1997, "Challenging Today's Stamped Steel Unibody: Assessing Prospects for Steel, Aluminum and Polymer Composites", IBEC 1997 Proceedings, Stuttgart;

Diehl. J., 1956, "Tensile test of Cu single crystal", Z. Metall., vol. 47, p. 331;

Dieter G., 1984, "Mechanical Metallurgy", Mc. Graw Hill., vol. 208-209, p. 331-356;

Dierke H., Krawehl F., Graff S., Forest S., Sachl J., Neuha H., 2006, " Portevin–LeChatelier effect in Al–Mg alloys: Influence of obstacles – experiments and modelling", Comp. Mat. Science, article in press;

Ding Y., Jiang J., Shan A., 2009, "Plastic instability and strain rate sensitivity of ultrafine-grained iron", Journal of Alloys and Compounds, vol. 487, p. 517–521;

Dirras G., Donnadeu P., Doutin J., 2005, "Dislocation precipitate interaction mechanism in 6xxx Aluminium", Report at Institut Galilee, Univerite Paris XIII;

Dos Santos J.F., 2006, "Improving Performance and Productivity of Integral Structures through Fundamental Understanding of Metallurgical Reactions in Metallic Joints", GKSS Research Centre Institute for Materials Research Max-Planck, Document Number: W/FT/012.06, p. 1-24;

Easton M, Song W.Q., Abbott T., 2006, "A comparison of the deformation of magnesium alloys with aluminium and steel in tension, bending and buckling", Mat & Design, vol. 27, p. 935-946;

Ezaz T., 2011, "An advanced perspective in twin growth in Nickel-Titanium", PdD Dissertation, University of Illinois, Urbana, Illinois USA;

Feng X., Fischer G., Zielke R., Svendsen B., Tillmann W., 2012, "Investigation of PLC band nucleation in AA5754", Mater. Sci. and Eng. A, vol. 539, p. 205-210;

Humphreys F. J., "Continuous and discontinuous grain particle containing Al-Sc alloy", Acta Mater., vol 53, p. 1097-1109;

François, D. P., 1998, "Mechanical Behaviour of Materials: Volume I: Elasticity and Plasticity", London: Kluer Academic Publishers;

Frank F.C, 1951, "The equilibrium of linear arrays of dislocations", Phil. Mag., vol. 42, p. 89;

Frommeyer G., Brux U., Neumann P., 2003, "Supra-ductile and high-strength manganese-TRIP/TWIP steels for high energy absorption", ISIJ International, vol. 43, p. 438;

Gallot E., 2011, "Effect of heat treatment and hot working on the microstructural characteristics of TWIP steels", Master Thesis, Universitat Politècnica de Catalunya, p. 12;

Golovin I.S., Mikhaylovskaya A.V., Sinning H.R., 2013, "Role of the β-phase in grain boundary and dislocation anelasticity in binary Al–Mg alloys", Journal of Alloys and Compounds**,** vol. 577, p. 622–63;

Graff S., 2006, "Viscoplastic behavior of zirconium alloys in the temperatures range 20C–400C: characterization and modeling of strain ageing phenomena", Paris: PhD Thesis: Ecole de Mines, France;

Grassel O., Kruger L., Frommeyer G., Meyer L., 2000, "High strength Fe-Mn-(Al, Si)TRIP/TWIP steels development properties application", Int. J. Plast., vol. 16, p. 1391;

Gubicza J., Chinh N.Q., Horita Z., Langdon T.G., 2004, "Effect of Mg addition on microstructure and mechanical properties of aluminum", Mater. Sci. and Eng. A, vol. 387-389, p. 55-59;

Guan Q. F., Zhang Q. Y., Dong C., and Zou G. T., 2005, "Deformation twining in single-crystal aluminum induced by high-current pulsed electron beam", Journal of Mater. Sci., vol. 40, p. 5049;

Gussev M.N., Busby J.T., Byun T.S., Parish C.M., 2013, "Twinning and martensitic transformations in nickel-enriched 304 austenitic steel during tensile and indentation deformations", Mat. Sci. Eng. A, vol. 588, p. 299-307;

Haasen P., 1965, "Physical Metallurgy", (R. W. Cahn, ed.), North-Holland, Amsterdam;

Haasen P., Mordike B. L., 1996, "Physical Metallurgy ", Cambridge University Press, Third Edition;

Hadda Y.M., 2001, "Mechanical Behavior of Engineering Materials", vol. 2, p.15;

Hai Jun L., Dingyi Z., Xian P., Zhenming H., Mingjie,W., 2013, "Dynamic Strain Aging in the Fe-Mn-Cu-C TWIP Steel", Adv. Mat. Res., vol. 668, p. 861-864;

Hayes R.W., Witkin D., Zhou F., Lavernia E.J., 2004, "Deformation and activation volumes of cryomilled ultrafine-grained aluminum", Acta Mater., vol. 52, p. 4259-4271;

Hallberg H., 2010, "Influence of Process Parameters on Grain Refinement in AA1050 Aluminum During Cold Rolling", Int.l Journal of Mechanical Sciences, vol. 66, p. 260-272;

Hall E.O., 1951, "The Deformation and Ageing of Mild Steel: III Discussion of Results", Proc.Phys. Soc B., vol. 64, p.747;

Hallberg H., Wallin M., Ristinmaa M., 2010, "Modeling of discontinuous dynamic recrystallization in pure Cu using a probabilistic cellular automaton", Comp. Mater. Sci., vol. 49, p. 25–34;

Haijun L., Dingyi Z., Xian P., Zhenming H., Mingjie W., 2013, Adv.Mat.Res., vol. 668, p. 861-864;

Han Q., Huang J., Zhu T., Lavernia E.J., 2006, "Negative Strain-Rate Sensitivity in a nanostructured Aluminum alloy", Advanced Engineering Mat., vol. 8, p. 945-947;

Harris J. E., Masters B. C., 1965, "The Stacking Fault Energy of Zinc and Magnesium", Physica status solidi B, vol. 9, p. 181–184;

Havner K. S., 1992, "Finite Plastic Deformation of Crystalline Solids", Cambridge University Press;

Hirsch J., 2011, "Aluminum in Innovative Light-Weight Car Design", Mater. Trans., vol. 52, p. 818-824;

Hirth J. P., Lothe J., 1982, "Theory of dislocations", second ed. John Wiley, New York,

Honnef H., Mecking H., 1978, "A method for the determination of the active slip systems and orientation changes during single crystal deformation. Textures of Materials", Proceedings of ICOTOM, vol. 5, p. 265-275;

Höppel H.W., May J., Eisenlohr P., Göken M., 2005, "Strain-rate sensitivity of ultrafine-grained materials", In: Zeit fur Metallkdunde, vol. 96, p. *566*-571;

Hosford W. F., 1993, "The Mechanics of Crystals and textured Polycrystals", Oxford Univ. Press, Technology & Eng., vol. 632–633, p. 56–85;

Hosford W. F., 2006, "The anisotropy of aluminum and aluminum alloys", Journal of The Min., Met & Mater. Society, vol. 58, p. 70;

Huang C., Gao Y., Yang G., Wu G., Li S., 2006, "Bulk nanocrystalline stainless steel fabricated by equal channel angular pressing", Mater. Res., vol. 21, p. 1687;

Humphreis F.J., Hatherly M., 2004," Recrystallization and related annealing phenomena", Second ed. Oxford, UK: Elsevier;

Hutchinson C.R., Loo P.T., Bastow T.J., Hill A.J., Da Costa Teixeira J., 2009, "Quantifying the strain-induced dissolution of precipitates in Al alloy microstructures using nuclear magnetic resonance", Acta Mater., vol. 57, p. 5645-5653;

Idrissi H., Renard K., Ryelandt L., Schryvers D., Jacques P.J., 2010, "On the mechanism of twin formation in Fe–Mn–C TWIP steels", Acta Mater., vol. 58, p. 2464–2476, (a);

Idrissi H., Renard K., Schryvers D., Jacques P.J., 2010, "On the relationship between the twin internal structure and the work-hardening rate of TWIP steels", Scripta Mater., vol. 63, p. 961, (b);

Idrissi H., Renard K., Schryvers D., Jacques P.J., 2013, "TEM investigation of the formation mechanism of deformation twins in Fe–Mn–Si–Al TWIP steels", Phil Mag., vol. 93-35, p. 4378-4391;

Ji Y.H., Park J., 2009, " Development of SPD by various asymetric rolling processes", Mater. Sci. and Eng. A, vol. 499, p.14-17;

Jiang H., Zhang Q., Chen X., Chen Z., Chen Z., Jiang Z., Wu X., Fan J., 2007, "Three types of Portevin Le-Chatelier effects: Experiment and modeling", Acta Mater., vol. 55, p. 2219-2228;

Jin H., Lloyd D.J., 2004, "The tensile response of a fine-Grained AA5754 alloy produced by asymmetric rolling and annealing", Metal and Mater. Trans. A, vol. 35, p. 997-1006 (a);

Jin H. and Lloyd, D., 2005, "The reduction of planar anisotropy by texture modification through asymmetric rolling and annealing in AA5754", Mater. Sci. and Eng. A, vol. 399, p. 358–367;

Jin H., Lloyd, D., 2009, "Effect of a duplex grain size on the tensile ductility of an ultra-fine grained Al-Mg alloy, AA5754, produced by asymmetric rolling and annealing", Scripta Mater., vol. 50, p. 1319–1323 (b);

Jin Y., Bernacki M., Rohrer G., Rollett A., Lin B., 2013, "Formation of annealing twins during recrystallization and grain growth in 304L austenitic stainless steel", 5th International Conference on Recrystallization and Grain Growth, ReX and GG, Sydney;

Kabirian F., Khan A.S., Pandey A., 2014, "Negative to positive strain rate sensitivity in 5xxx series aluminum alloys: Experiment and constitutive modeling", Int. Jou. of Plast., vol. 55, p. 232-246;

Kalkman A.J., A.H. Verbruggen, G., Radelaar S., 2002, "High-temperature tensile tests and activation volume measurement of free-standing submicron Al films", Journal of Applied Physics., vol. 92, p. 6612-6615;

Kammers A.D., Ngam J.W., Langdon T.G., Daly S., 2015, "The microstructure length scale of strain rate sensitivity in ultrafine-grained aluminum", Jou. of Mater. Research, vol. 30, p. 981-992;

Kang S.B., Min B.K., Kim H.W., Wilkinson D.S., Kang J., 2005, "Effect of asymmetric rolling on the texture and mechanical properties of AA6111-Aluminum sheet", Metal.and Mater.Trans., vol. 36A, p. 3141-3149

Karaman I., Sehitoglu H., Beaudoin A.J., Chimlyakov Y.I., Maier H.I., Tome C.N., 2000, "Modeling the deformation behavior of Hardfield Steel in single and polycrystals due to twinning and slip", Acta Mater., vol. 48, p. 2031-2047;

Kibey S., Liu J.B., Johnson D.D., Sehitoglu H., 2007, "Predicting twinning stress in fcc metals: Linking twin-energy pathways to twin nucleation", Acta Mater., vol. 55, p. 6843–6851;

Kim J.K., Chen L., Kim H.S., Kim S.K., Estrin Y., De Cooman B.C., 2009, "On the Tensile behavior of High-Manganese Twinning-Induced Plasticity Steel" Metall. Mat. Trans., vol. 40A, p. 3147-3158 (a);

Kim S.J., Jang S.K., 2009, "Effects of solution heat treatment on corrosion resistance of 5083F Al alloy", Trans. Nonferrous Met. Soc. China, vol. 19, p. 887−891 (b);

Kim J.K., Estrin Y., Beladi H., Kim S.K., Chin K.G., De Cooman B.C., 2010, "Constitutive Modeling of TWIP Steel in Uni-Axial Tension", Materials Science Forum, vol. 654-656, p. 270-273;

Kim S.J., Jang S., Han M., Kim S.C., Kim J.S., 2011, "Effects of precipitation strengthening heat treatment for AlMg alloy", Trans. Nonferrous Met. Soc. China., vol. 21, p. 1218-1224;

Kim J.G., Hong S., Anjabin N., Park B.H., Kim S.K., Chin K.G., Lee S., Kim H.S., 2015, "Dynamic strain aging of twinning-induced plasticity (TWIP) steel in tensile testing and deep drawing", Mater. Sci. Eng. A, vol. 633, p.136-143;

Kim K.H., Lee D.N., Choi, C.H., 1999, "The deformation textures and lankford values of asymmetrically rolled aluminum alloy sheets", Proceedings of the 12th ICOTOM, J. Szpunar, ed., NRC-CNRC, Ottawa, Canada, p. 267–272;

Kim K.H., Lee D.N., 2001, "Analysis of deformation textures of asymmetrically rolled aluminum sheets", Acta Mater., vol. 49, p. 2583–2595;

Klassen-Neklyudova M.V., 2012, "Mechanical Twinning of Crystals", Springer Science & Business Media, USA, p. 9;

Kocks U.F., 1970, "The relation between polycrystal deformation and single crystal deformation", Metall. Trans., vol. 1, p. 1121;

Kocks U. F., 2000, " Texture and Anisotropy: Preferred Orientations in Polycrystals and their Effect on Materials Properties", Cambridge University Press;

Kocks U.F., **Mecking H**., 2003, "Physics and phenomenology of strain hardening: the FCC case" Progress in Materials Science, vol. 48, p. 171–273;

Korbel A. Z., 1976, "A new approach to the Portevin–LeChatelier effect", Acta Metall., vol 24, p. 919-923;

Krishna K.S.V.B.R., Sekhar C., Tejas R., Krishna N., Sivaprasad K., Narayanasam R.K., 2015, "Effect of cryorolling on the mechanical properties of AA5083 alloy and the Portevin–Le Chatelier phenomenon", Materials&Design, vol. 67, p. 107-117;

Kröner E., 1961, "Zur plastischen verformung des vielkristalls: On the plastic deformation of polycrystals", Acta. Metall., vol. 9, p. 155;

Kubin L. E., 1985, "The Portevin-Le Chatelier effect in deformation with constant stress rate", Acta Metall., vol. 33, p. 397-407;

Kubin L. E., 1990, "Evolution of dislocation densities and the critical conditions for the Portevin-Le Châtelier effect", Acta Met.Mater., vol. 38, p. 697;

Kumar R., 2002, "Formability analysis of extra-deep drawing steel", Materials Processing Tech., vol. 130-131, p. 31-41;

Lebedkina T.A., Lebyodkin M.A., Chateau J.P., Jacques A., Allain S., 2009, "On the mechanism of unstable plastic flow in an austenitic FeMnC TWIP steel", Mat. Sci. and Eng. A, vol. 519, p. 147;

Lebensohn, R.A., Tomé, C.N., 1993, "A selfconsistent approach for the simulation of plastic deformation and texture development of polycrystals: application to Zirconium alloys". Acta Metall. et Mater., vol. 41, p. 2611–2624;

Lee J.K, Lee D.N., 2007, "Texture evolution and grain refinement in AA1050 aluminum alloy sheets asymmetrically rolled with varied shear directions", Key Eng. Mat., vol. 340–341, p. 619–26;

Lee J. K., Lee D. N., 2008, "Texture control and grain refinement of AA1050 Al alloy sheets by asymmetric rolling", Int. Jou. of Mech. Sci., 50, p. 869–887;

Li S., Li X., Yang L., 2013, "Role of strain path change in grain refinement by severe plastic deformation: A case study of equal channel angular extrusion", Acta Mater., vol. 61, p. 4398–4413 (a);

Li Y., Zhua L., Liu Y., Wei Y., Wu Y., Tang D., Mi Z., "On the strain hardening and texture evolution in high manganese steels: Experiments and numerical investigation", Journal of the Mechanics and Physics of Solids, vol. 61, p. 2588–2604 (b);

Li S., Beyerlein I.J., Neckera C.T., 2006, "On the development of microstructure and texture heterogeneity in ECAE via route C", Acta Mater., vol. 54, p. 1397–1408;

Liang S., 2012, "Deformation and Its Effect on Recrystallization in Magnesium Alloy AZ31", PhD Thesis, Mater. Sci. & Eng. Univ., Hamilton, USA;

Liu R., Zhang Z. J., Li L. L., An X. H., Zhang Z. F., 2015, "Microscopic mechanisms contributing to the synchronous improvement of strength and plasticity (SISP) for TWIP copper alloys", Sci Rep., vol. 5, p. 5-9550;

Lloyd D.J., 1980, "Microstructural Control in Aluminum Alloys", Metal Trans., vol. 11, p. 1287;

Lopes A. B., 2010, "Experimental methods of X-Ray diffraction", lecture notes;

Lopes A. B., 2001, "Analise microstructural das instabilidades plasticas em materias metalicos", Aveiro, PhD thesis, 227, Portugal;

Lu Song, 2012, "Firts-principles investigations of planar defects", School of Industrial Engineering and Management, Licentiate Thesis Department of Materials Science and Engineering, KTH, Sweden;

.

Ma C.Q., Hou L.G., Zhang J.S., Zhuang L.Z., 2014, "Experimental and Numerical Investigations of the Plastic Deformation during Multi-Pass Asymmetric and Symmetric Rolling of High-Strength Aluminum Alloys", Materials Science Forum, 794-796, p. 1157-1162;

Ma C.Q., Hou L.G., Zhang J.S., Zhang L.Z., 2015, "Strain analysis during symmetric and asymmetric rolling of 7075 Al alloy sheet", Light Met., vol. 1, p. 445-449;

May J, Hoppel H.W, Goken M., 2005, "Strain rate sensitivity of ultrafine-grained aluminium processed by severe plastic deformation", Scripa Mater., vol. 53, p. 189-194;

Mánik T., Holmedal B., 2014, "Review of the Taylor ambiguity and the relationship between rate-independent and rate-dependent full-constraints Taylor models", Int. Journal of Plasticity, vol. 55, p. 152-181;

McCormick P.G., 1972, "A model for the Portevin-Le Chatelier effect in substitutional alloys", Acta Metall., vol. 20, p. 351-354;

McCormick P. E., 1989, "Transient flow behavior associated with dynamic strain ageing", Scripta Met., vol. 23, p. 1231;

Miyamoto H, Ota K Mimaki T., 2006, "Viscous nature of deformation of ultra-fine grain aluminum processed by equal-channel angular pressing", Scripta Mater., vol. 54, p. 1721-1725;

Miranda F., 2008, "Mechanical behavior of an aluminum alloy and a structural steel under multiaxial low cycle fatigue", Department of Mech. Eng., Instituto Superior Técnico Av. Rovisco 1 – 1049-001 Lisboa, Portugal;

Mohamed F. A., 2003, "A dislocation model for the minimum grain size obtainable by milling," Acta Mater., vol. 51, p. 4107;

Molinari A., Canova G.R, Ahzi S., 1987, "A self-consistent approach of the large deformation polycrystal viscoplasticity", Acta Metall., vol. 35, p. 2983–94;

Morishige T., Hirota T., Vesuge T., TakigawaY., Higasgi K., 2011, "Effect of Mg content on the minimum grain size of Al–Mg alloys obtained by friction stir processing", Scripta Mater, vol. 64, p. 355-358;

Morita M., Umezawa O., 2011, "Slip Deformation Analysis Based on Full Constraints Model for ά-Titanium Alloy at Low Temperature", Mater. Trans., vol. 52, p. 1595-1602;

Mulford R.A., Kocks U.F., 1979, "New observations on the mechanisms of dynamic strain aging and of jerky flow", Acta Metall., vol. 27, p. 1125-1134;

Muzyk M., Pakiela Z., Kurzydlowski K.J., 2011, "Ab initio calculations of the generalized stacking fault energy in aluminum alloys", Scripta Mater., vol. 64, p. 916–918;

Najafi-Zadeh A., Jonas J. J., Yue S., 1992, "Grain refinement by dynamic recrystallization during the simulated warm-rolling of interstitial free steels", Metall. Trans. A, vol. 23, p. 2607;

Nikura M., Hasegawa K., Fujita T., 1997, "Effect of strain rate on elongation and serration behavior in Al-Mg alloy sheets", Journal of Japan Institute of Light Metals, vol.47, p.469;

Niendorf T., Rüsing C.J., Frehn A., Maier H.J., 2013, "The Deformation Behavior of Functionally Graded TWIP Steel under Monotonic Loading at Ambient Temperature", Mat. Res. Let., vol 1, p. 96-101;

Nikolaevich S.A., Valerievich A.A., Igorevich G.A., Alexandrovich S.A., Alexandrovich S.M., 2014, "Advanced materials of automobile bodies in volume production", European Transport \ Trasporti Europei, p. 1-27;

Nolze G., 2015, "Euler angles and crystal symmetry", Crystal Research and Technology, vol.50, p. 188-201;

Nukala H., 2008, "Quantitative thickness mapping in high angle annular dark field (HAADF) Scanning Transmission Electron Microscopy (STEM)", Master thesis, B.E, Andhra University, Visakhapatnam, Florida;

Osakada K., 2008, "History of Plasticity and Metal Forming Analysis", The 9th International Conference on Technology of Plasticity", p. 22, ICTP;

Petch N.J., 1953, "The cleavage strength of polycrystals", J. Iron Steel Inst., vol. 174, p.25;

Penning P. 1972, "On the theory of the portevin-le chatelier effect", Acta metall., vol. 20, p. 1169;

Pennycook S. J., Nellist P. D., 2011, "Scanning Transmission Electron Microscopy: Imaging and Analysis", Springer Science & Business Media, London, p. 540;

Picu R. C., 2003, "Atomistic study of pipe diffusion in Al-Mg alloys", Acta Mater., vol. 52, p. 161;

Picu R.C., 2004, "A mechanism for the negative strain rate sensitivity of dilute solid solutions", Acta Mater., vol. 52, p. 3447-3458;

Picu R.C., Zhang D., 2004, "Atomistic study of pipe diffusion in Al–Mg alloys", Acta Mater., vol. 52, p. 161-171;

Picu R.C., Vincze G., Ozturk F., Gracio J.J., Barlat F., Maniatty A.M., 2005, "Strain rate sensitivity of the commercial aluminum alloy AA5182-O", Mater. Science and Eng. A, vol. 390, p. 334-343;

Picu R.C., Vincze G., Gracio J.J., Barlat F., 2006, "Effect of Solute Distribution on the Strain Rate Sensitivity of Solid Solutions", Scripta Mater., vol. 54, p. 71;

Popovic M., Romhanji E., 2008, "Characterization of microstructural changes in an Al-6.8 wt.% Mg alloy by electrical resistivity measurements", Mat. Sci. and Eng. A, vol. 492, p. 460-467;

Portevin A., Le Chatelier H., 1923, "Sur un phénomène observé lors de l'essai de traction d'alliages en cours de transformation", Comptes Rendus de l'Académie des Sciences, Paris, vol.176, p. 507-510;

Qian T. Marx M., Schuler K., Hockauf M., Vehoff H., 2010, "Plastic deformation mechanism of ultra-fine-grained AA6063 processed by equal-channel angular pressing", Acta Mater., vol. 58, p. 2112-2123;

Raabe D., Springer H., Gutieres-Urrutia I., Roters F., Bausch M., Seol J.B., Koyama M., P.P. Choi, 2014, **"**Alloy Design, Combinatorial Synthesis, and Microstructure– Property Relations for Low-Density Fe-Mn-Al-C Austenitic Steels", JOM, vol.66, p. 1845-1855;

Radović L., Nikačević M., 2008, "Microstructure and Properties of Cold Rolled and Annealed Al-Mg Alloys", Scientific Technical Review, vol. 58, p. 14-19;

Reed, R.P., Schram R.E., 1974, "Relationship between Stacking- Fault Energy and X-Ray Measurements of Stacking Fault Probability and Microstrain", J. Appl. Phys. vol. 45, p.4705 – 4711;

Reisman L., 2011, "Car Wars: Aluminum v. Steel, Episode Two", Sourcing & Trading Intelligence for Global Markets;

Renard, K., Ryelandt, S., Jacques, P.J., 2010, "Characterization of the Portevin-Le Châtelier effect affecting an austenitic TWIP steel based on digital image correlation", Mat. Sci. and Eng. A, vol. 527, p. 2969;

Rizzi E., Hahner P., 2004, "On the Portevin Le-Chatelier effect: theoretical modeling and numerical results", Int. Jou. of Plasticity, vol. 20, p.121-165;

Romhanji E., Popovic M., GliŠiĆ D., Stefanovich M., Milovanovic M., 2002, "The Al-Mg alloy sheets for automotive application: Problems and solutions", Association of Metall. Eng. Serbia and Montenegro, Invited paper, p. 205-216;

Romhanji E., Popovic M., Glisic D., Dodok R., Jovanovi D., 2006, "Effect of annealing temperature on the formability of Al–Mg4.5–Cu0.5 alloy sheets", Journal of Mat. Proc. Tech., vol. 177, p. 386-389;

Rosengaard N. M., Skriver, H. L., 1993, "Calculated stacking-fault energies of elemental metals", Phys. Rev. B, vol. 47, p. 12865;

Roy B., Kumar N.K., Nambissan P.M.G., Das J., 2014, "Evolution and interaction of twins, dislocations and stacking faults in rolled α-brass during nanostructuring at sub-zero temperature", AIP Advances, vol. 4, no. 6;

Roylance D., 2001, "Stress-Strain Curves", Department of Materials Science and Engineering Massachusetts Institute of Technology Cambridge, MA 02139;

Roylance D., 2008, " Mechanical properties of materials", Massachusetts Institute of Technology, Available at: http://stuff.mit.edu/afs/athena/course/3/3.225/book.pdf. ISBN-10: 0471593990;

Sachs G.Z., 1928, Verein. Deut. Ing., vol. 72, p. 734;

Sakai T., Hamada S., Saito Y., 2001, "Improvement of the r-value in 5052 aluminum alloy sheets having through-thickness shear texture by 2-pass single-roll drive unidirectional shear rolling", Scripta mater., vol. 44, p. 2569–2573.

Saleh A.A., Pereloma E.V., Gazder A.A., 2013, "Microstructure and texture evolution in a twinning-induced-plasticity steel during uniaxial tension", Acta Mater., vol. 61, p. 2671-2691;

Sanchez-Martin R., Zambaldi C., Perez-Prado M.T., Molina-Aldareguia J.M., 2015, "High temperature nanoindentation of pure magnesium", Scripta Mater., Article in press.

Sanders P. E., 1997, "Elastic and tensile behavior of nanocrystalline copper and palladium", Acta Mater., vol. 45, p. 4019;

Santos D., Gonzales B., Pereloma E., 2012, "Recrystallization and mechanical behavior of high Mn and low C cold rolled and annealed steel with TWIP effect", Materials Science Forum, vol. 715-716, p. 579-584;

Sarkar A. B., 2005, "Scaling Behavior of Portevin LeChatelier Effect", International Conference on Statistical Mechanics, Kolkata, India;

Schmid E., 1924, "Yield Point" of crystals. Critical shear stress law", Proc. Int. Cong. Appl. Mech., vol. 342;

Schwarz, D., Bachem, H., and Opbroek, E., 2004, "Comparison of Steel and Aluminium Hood with Same Design in View of Pedestrian Head Impact", SAE Technical Paper, 01-1605;

Schuman H., 1971, "Martensitische Umwandlung in austenitischen Mangan-Kohlenstoff-Stählen", Neue Hutte, vol. 17, p. 605-609;

Segurado J., Lebensohn R.A., Llorca J., Tomé C.N., 2012, "Multiscale modeling of plasticity based on embedding the viscoplastic self-consistent formulation in implicit finite elements", Int. Journal of Plast., vol. 28, p. 124–140;

Schuh C. A., 2006, "Nanoindentation studies of materials", Materials Today, vol. 9, p. 32-40;

Simões F. P., Alves de Sousa R. J., Gracio J. J., Barlat F., Yoon J. W., 2008, "Mechanical behavior of an asymmetrically rolled and annealed 1050-O sheet", Int. Journal of Mech. Sci., vol. 50, p. 1372–1380.

Singh D., Nageswara P., Jayaganthan R., 2013, "Effect of deformation temperature on mechanical properties of ultrafine grained Al–Mg alloys processed by rolling", Materials & Design, vol. 50, , p. 646–65;

Shen Y.F., Lu L., Dao M., Suresh S., 2006, "Strain rate sensitivity of Cu with nanoscale twins", Scripta Mater., vol. 55, p. 319-322;

Soare M.A., Curtin W.A., 2008, "Solute strengthening of both mobile and forest dislocations: the origin of dynamic strain aging in FCC metals", Acta Mater., vol. 56, p. 4046–4061;

Superlightcar Project, 2009, Internet: *www.superlightcar.com* and *www.arup.com;*

Swygenhoven H., Derlet P. M., Frøseth A.G., 2004, "Stacking fault energies and slip in nanocrystalline metals", Nature Mater., vol. 3, p. 399 – 403;

Tadmor E.B., Bernstein N., 2004, "A first-principles measure for the twinnability of FCC metals", Mech. and Physics of Solids, vol. 52, p. 250 –2519;

Tamimi S., Correia J. P., Lopes A. B., Ahzia S., Barlat F., Gracio J. J., 2014, "Asymmetric rolling of thin AA-5182 sheets: Modelling and experiments", Mater. Sci. and Eng. A, vol. 603, p. 150–159;

Taye F., Das P., Kumar R.D., Sankar B.R., 2014, "Characterization of Mechanical Properties and Formability of Cryorolled Aluminium Alloy Sheets" 45 th International & 26th All India Manuf. Tech., Design and Research Conf. IIT Guwahati, Assam, India 511-1;

Taylor G.I., 1938, “Plastic strain in metals”, Journal Inst. Metals, vol. 62, p. 307;

Titov V., 2004, "Rolled steel sheet for the abroad automotive industry”, National Metall., vol. 5, p. 84-89;

Tome C.N., Lebensohn R.A., Necker C.T., 2002, “Orientation correlations and anisotropy of recrystallized aluminum", Metall. Mater. Trans. A, vol. 33, p. 2635-2648;

Tomé C.N., Maudlin P.J., Lebensohn R.A., Kaschner G.C., 2001, “ Mechanical response of zirconium: I. Derivation of a polycrystal constitutive law and finite element analysis”, Acta Mater., vol. 49, p. 3085–3096;

Tuan Q., Puga H., Barbosa J., Pinto A.M.P., 2015, “Grain Refinement of Al-Mg-Sc Alloy by Ultrasonic Treatment”, Met. Mater. Int., vol. 21, p. 72-78;

Uota T., Suzu T., Fukumoto S., Yamamoto A., 2009, “EBSD Observation for Reversible Behavior of Deformation Twins in AZ31B Magnesium Alloy”, Mater. Trans., vol. 50, p. 2118-2120;

Ungureanu, C. A., 2007, “Design for sustanability: Product life-cycle analysis in Aluminium auto Body applications”, University of Kentucky Master's Thesis, Paper 449;

Valiev R. Z., Langdon T.G., 2006, “Principles of equal-channel angular pressing as a processing tool for grain refinement”, Progress in Mater. Science, vol. 51, p. 881-981;

Valiev R., 2004, “Nanostructuring of metals by severe plastic deformation for advanced properties”, Nature Mater., vol. 3, p. 511 – 516;

Van Houtte P., 1981, “Adaptation of the Taylor theory to the typical substructure of cold rolled FCC metals”, in Sixth Int. Conf. On Texture of Materials, Tokyo: The Iron and Steel Institute of Japan, p. 428;

Van Houtte, **P**., 1986, “The effect of strain path on texture: theoretical and experimental considerations”, Strength of Metals and Alloys, H.J.McQueen & al., eds. Oxford: Pergamon, p. 1701-1986;

Van Swygenhoven H, Caro A., 1998, “Plastic behavior of nanophase metals studied by molecular dynamics”, Physical Review B, vol. 58:11246, p. 51;

Van Swygenhoven H, Spaczer M, Caro A, Farkas D., 1999, “Competing Plastic Deformation Mechanisms in Nanophase Metals”, Physical Review B, p. 60-22;

Van Swygenhoven H., 2002,”Polycrystalline materials - Grain boundaries and dislocations”, Mater. Science and Eng., vol. 296, p. 66;

Van Swygenhoven H., Derlet P.M., Frøseth A.G., 2004,”Stacking fault energies and slip in nanocrystalline metals”, Nature Mater., vol. 3, p. 399;

Vincze G., 2007, "Investigation methodologies for metals used in forming processes", PhD Thesis, Universidade de Aveiro, Aveiro, Portugal;

Wei Q., 2007, "Strain rate effects in the ultrafine grain and nanocrystalline regimes—influence on constitutive response", Jou. of Mater. Sci., vol. 42, p. 1709-1727;

Wen W., Zhao Y., Morris G.J., 2005, "The effect of Mg precipitation of the mechanical properties of 5XXX aluminium alloys", Mat. Sci. and Eng. A, vol. 392, p. 136-144;

Whelan M.J., 1959, "Dislocation Interactions in Face-Centred Cubic Metals, with Particular Reference to Stainless Steel", Proc. Roy Soc, vol. 249, p. 114;

William D., Callister Jr., 2007, "1/th Edition: Materials science and engineering, an introduction", Danvers : John Willey & Sons, Inc;

Wilkinson D.S., 2013, " Advanced structural materials", Technology & Engineering Proceedings of the International Symposium On: Advanced Structural Materials, vol 9. p. 34 ;

Wohlecker R., and Henn R., 2009, "Mass Reduction Potential of Steel and Aluminum in Automotive Applications", SAE Int. J. Mater. Manf., vol. 1, p. 480-484;

[www$_1$] http://www.key-to-metals.com/Article137.htm (accessed on 26.07.2015);

[www$_2$]- http://aluminium.matter.org.uk/accesed (accessed on 14.03.2014);

[www$_3$] http://www.archertower.com/aluminum-magnesium-phase-diagram (accessed on 2.08.2015)

Xu Z., Picu R.C., 2007, "Effect of residual and pre-existing solute clusters on dynamic strain ageing in dilute solid solutions", Model. Simul. Mater. Sci. Eng., vol. 15, p. 385–396;

Xu C., Horita Z., Langdon T. G., 2008, "The evolution of homogeneity in an aluminum alloy processed using high-pressure torsion", Acta Mater., vol. 56, p. 5168–5176;

Xu L., Chen L., De Cooman B.C., Steglich D., Barlat F., 2010, "Hole expansion of advanced high strength steel sheet sample", Int. J. Mat. Forming, vol. 3, vol. 247;

Xu X., Picu R.C., 2006, "Dislocation–solute cluster interaction in Al–Mg binary alloys", Modelling Simul. Mater. Sci. Eng., vol. 14, p. 195;

Yakubtsov I.A., Airapour A., Perovic D.D., 1999, "Some aspects of high manganese twinning-induced plasticity (TWIP) steel, a review", Acta Mater., vol. 47, p. 1271-1279;

Yamakov V., Wolf D., Phillpot S.R., Gleiter H., 2002, ”Dislocation processes in the deformation of nanocrystalline aluminium by molecular-dynamics simulation”, Nature Mater., vol. 1, p. 45;

Youssef K., Sakaliyska M., Bahmanpour H., Scattergood R., Koch C., 2011, “ Effect of stacking fault energy on mechanical behavior of bulk nanocrystalline Cu and Cu alloy”, Acta Mater., vol. 59, p. 5758-5764;

Youssef K.M., Scattergood R.O., Murty K.L., Koch C.C., 2006, "Nanocrystalline Al-Mg Alloy With Ultrahigh Strength and Good Ductility", Scripta Mater., vol. 54, p. 251-256;

Yu H., Tieu A., Lu K., Liu X., Liu M., Godbole A., Kong C., Qin Q., 2015, **“**A new insight into ductile fracture of ultrafine-grained Al-Mg alloys”, Sci. Rep., vol. 5, p. 9568;

Zavattieri P.D., Savic V., Hector L.G., Fekete,J.R., Tong W., Xuan Y., 2009, “Spatiotemporal characteristics of the Portevin-LeChatelier effect in austenitic steel with twinning induced plasticity”, Int. J. Plast., vol. 25, p. 2298;

Zhilyaev A.P., Langdon T.G., 2008, “Using high-pressure torsion for metal processing: Fundamentals and applications”, Progress in Mater. Science, vol. 53, p. 893-979;

Zhang Z.J., Duan Q.Q., An X.H., Wu S.D., Yang G., Zhang Z.F., 2011, “Microstructure and mechanical properties of Cu and Cu–Zn alloys produced by equal channel angular pressing”, Mater. Sci. and Eng. A, vol. 528, p. 4259-4267.